

# **Vertical Graphene Nanosheets: Growth, Structure and Electrochemical Performance**

By

**SUBRATA GHOSH**

**Enrolment no: PHYS02 2011 04 005**

**Indira Gandhi Centre for Atomic Research,  
Kalpakkam, Tamil Nadu, India, 603102**

*A thesis submitted to the  
Board of studies in Physical Sciences*

*In partial fulfilment of requirements  
for the degree of*

**DOCTOR OF PHILOSOPHY**

of

**HOMI BHABHA NATIONAL INSTITUTE**

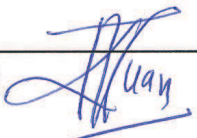


**May 2016**

## Homi Bhabha National Institute

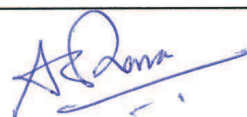
### Recommendations of the Viva Voce Board

As members of the Viva Voce Committee, we certify that we have read the dissertation prepared by **Subrata Ghosh** entitled "**Vertical Graphene Nanosheets: Growth, Structure and Electrochemical Performance**" and recommend that it may be accepted as fulfilling the thesis requirement for the award of Degree of Doctor of Philosophy.

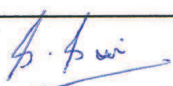
Chairman: Dr. A. K. Tyagi  Date: 24/10/2016

Guide: Dr. M. Kamruddin  Date: 24/10/16

Examiner: Dr. Harish Barshilia  Date: 24.10.2016

Member: Dr. S. K. Dhara  Date: 24/10/2016

Member: Dr. G. Amarendra  Date: Oct 24, 2016

Member: Dr. Saroja Saibaba  Date: 24/10/2016

Final approval and acceptance of this dissertation is contingent upon the candidates' submission of the final copies of the thesis to HBNI.

I hereby certify that I have read this dissertation prepared under my direction and recommend that it may be accepted as fulfilling the thesis requirement.

Date: 24/10/16

Place: Kalpakkam

  
Dr. M. Kamruddin  
(Guide)

## STATEMENT OF AUTHOR

This dissertation has been submitted in the partial fulfilment of requirements for an advanced degree at Homi Bhabha National Institute (HBNI) and is deposited in the Library to be made available for borrowers under rules of the HBNI.

Brief quotations from this dissertation are allowable without special permission, provided that accurate acknowledgement of source is made. Requests for permission for extended quotation from or reproduction of this manuscript in whole or in part may be granted by the Competent Authority of HBNI when in his or her judgement the proposed use of the material is in the interests of the scholarship. In all other instances, however, permission must be obtained from the author.

  
SUBRATA GHOSH

## DECLARATION

I, hereby declare that the investigation presented in the thesis has been carried out by me. The work is original and has not been submitted earlier as a whole or in part for a degree/diploma at this or any other Institution/University.

  
SUBRATA GHOSH

## LIST OF PUBLICATIONS/PREPRINTS

### *Publications in Journals/Preprints arising from thesis*

1. Supercapacitative vertical graphene nanosheets in aqueous electrolytes, **Subrata Ghosh**, Tom Mathews, Bhavana Gupta, A. Das, Nanda Gopala Krishna and M. Kamruddin. *ACS Energy Lett.* **2016**, (Manuscript ID : nz-2016-00463v) [arXiv:1603.08320](https://arxiv.org/abs/1603.08320)
2. A route towards controlling the morphology of vertical graphene nanosheets, **Subrata Ghosh**, K. Ganesan, S. R. Polaki and M. Kamruddin. **2016**, [arXiv:1603.08322](https://arxiv.org/abs/1603.08322)
3. MnO<sub>2</sub>/Vertical graphene nanosheets as active materials for energy storage, **Subrata Ghosh**, Bhavana Gupta, K. Ganesan, A. Das, M. kamruddin, Sitaram Dash and A. K. Tyagi, *Mat. Today Proc.*, **2016** 3, 1686-1692
4. Effect of Annealing on the Structural Properties of Vertical Graphene Nanosheets, **Subrata Ghosh**, K. Ganesan, S. R. Polaki, A. K. Sivadasan, M. Kamruddin and A. K. Tyagi, *Adv. Sc. Eng. Med.* **2016**; 8,146-149
5. Flipping growth orientation of nanographitic structures by plasma enhanced chemical vapor deposition, **Subrata Ghosh**, K. Ganesan, S. R. Polaki, S. Ilango, S. Amrithapandian, S. Dhara, M. Kamruddin and A. K. Tyagi, *RSC Adv.* **2015**, 5, 91922-91931
6. Influence of substrate on nucleation and growth of vertical graphene nanosheets, **Subrata Ghosh**, K. Ganesan, S. R. Polaki, Tom Mathews, Sandip Dhara, M. Kamruddin and A. K. Tyagi, *Appl. Surf. Sc.* **2015**, 349, 576-581
7. Evolution and defect analysis of vertical graphene nanosheets, **Subrata Ghosh**, K. Ganesan, Shyamal. R. Polaki, T. R. Ravindran, Nanda Gopala Krishna, M. Kamruddin and A. K. Tyagi *J. Raman Spectrosc.* **2014**, 45, 642-649 [arXiv:1402.2074v3](https://arxiv.org/abs/1402.2074v3)

### *Conferences*

1. Vertical graphene nanosheets as supercapacitor electrodes: effect of morphology and electrolyte, **Subrata Ghosh**, B. Gupta, M. Kamruddin and A.K. Tyagi. NANOS-2015, GITAM University, Visakhapatnam, India (*Oral presentation*)
2. Synthesis and structure-property analysis of vertical graphene nanosheets and their applications towards energy storage devices, M. Kamruddin, **Subrata Ghosh**, K. Ganesan, and A.K. Tyagi, NANO-2015, K.S.R. College of Engineering, Tamil Nadu India (*Oral presentation*)

3. X-ray photoelectron spectroscopy analysis of defect structures in carbon nanomaterials, K. Ganesan, **Subrata Ghosh**, N. G. Krishna, M. Kamruddin and A.K. Tyagi, FAM-2015, IISc-Bangalore, India. (*Poster presentation*)
4. MnO<sub>2</sub>-Vertical graphene nanosheets as active materials for energy storage, **Subrata Ghosh**, B. Gupta, A. Das, K. Ganesan, M. Kamruddin, S. Dash and A.K. Tyagi, RAINSAT-2015, Sathyabhama University, India. (*Oral presentation*)
5. Effect of annealing on the structural properties of vertical graphene nanosheets, **Subrata Ghosh**, K. Ganesan, S. R. Polaki, A. K. Sivadasan, M. Kamruddin, A. K. Tyagi: NANOCON 014, Bharati Vidyapeeth University, Pune, India. (*Oral presentation*)
6. Role of feedstock gases on the growth of planar and vertical morphology carbon nanostructures, K Ganesan, **Subrata Ghosh**, S R Polaki, M Kamruddin, A K Tyagi, EMCA-2014, National Institute of Technology-Durgapur, India. (*Poster presentation*)
7. Influence of feedstock gas composition on growth of vertical graphene nanosheets by ECR CVD, **Subrata Ghosh**, K. Ganesan, S. R. Polaki, S. Dhara, M. Kamruddin, A. K. Tyagi, ICONSAT-2014, INST-Mohali, India (*Poster presentation*)
8. Evolution and defect analysis of graphene nanosheets grown by ECR-CVD, **Subrata Ghosh**, K. Ganesan, S. R. Polaki, T. R. Ravindran, N. G. Krishna, M. Kamruddin, A. K. Tyagi, IUMRS-ICA 2013, IISc Bangalore, India (*Poster presentation*)

## **Others (not included in thesis)**

### ***Publications in journal/Preprints***

1. A Comparative Study on Defect Estimation using XPS and Raman Spectroscopy in Few Layer Nanographitic Structures. K. Ganesan, **Subrata Ghosh**, Nanda Gopala Krishna, S. Ilango, M Kamruddin, and A K Tyagi, *Phys. Chem. Chem. Phys.* **2016**, 18, 22160-22167. [arXiv: 1607.04482v1](https://arxiv.org/abs/1607.04482v1)
2. Temperature and Pressure Dependent Raman Spectroscopic Studies and Thermal Conductivity of Vertical Graphene Nanosheets. K. K. Mishra, **Subrata Ghosh**, T. R. Ravindran, S. Amrithapandian, and M. Kamruddin, *J. Phys. Chem. C* (Manuscript ID: jp-2016-08754s)

3. Vertical Graphene Nanosheets for Supercapacitor Application in Organic Electrolyte, **Subrata Ghosh**, Madhusmita Sahoo, T. Mathews and M. Kamruddin, (Submitted to *AIP Conf. Proc.* For DAE-SSPS-2016)
4. Heterogeneous Electron Transfer Properties of Vertical Graphene Nanosheets, Dale Brownson, **Subrata Ghosh**, C. E. Banks and M. Kamruddin, (Manuscript under preparation)

### *Conferences*

1. Temperature Dependent Raman Studies and Thermal Conductivity of Vertical Graphene Nanosheet, K. K. Mishra, **Subrata Ghosh**, T. R. Ravindran. ICMST-2016, St. Thomas College, Pala, Kerala, India (*Poster presentation*)

  
SUBRATA GHOSH

**Dedicated to**



*Ask the right questions, and nature will open the door to her secrets*

## ACKNOWLEDGEMENTS

From the first moment of journey towards this dissertation, time moves on her way. In this page, I want to recall all, without them this dissertation would not have been possible.

First and foremost, I sincerely thank and express my deepest gratitude to my supervisor, Dr. M. Kamruddin for his guidance, encouragement and patience throughout the course of present dissertation.

I would like to express my gratitude to Dr. S.A.V. Satya Murty, Dr. Basudev Rao, and Dr. S. C. Chetal, present and past Director, IGCAR for permitting me to pursue Ph. D at IGCAR. I am highly thankful to Dr. G. Amarendra, Dr. C. S. Sundar, and Dr. M. P. Janawadkar, present and past Group Director, MSG for providing the conducive atmosphere for my smooth research. I thank Dr. Saibaba for the wonderful hospitality during my stay at JRF Enclave.

I am also very grateful to all the professors of my doctoral committee; Dr. A. K. Tyagi, Dr. S. K. Dhara, Dr. G. Amarendra, and Dr. Saroja Saibaba for sharing their valuable time and for providing me with helpful feedback and evaluating my work at each stage.

I would like to thank Dr. K. Ganesan, Mr. S. R. Polaki, Dr. P. K. Aji Kumar, Mr. Nanda Gopala Krishna, Dr. Bhavana Gupta, Dr. Tom Mathews, Mrs. Madhusmita Sahoo, Dr. Prasana Sahoo, Dr. Avinash Patsha, Dr. Bonu Venkatramana, Mr. Kishore Madupu, Mr. A. K. Sivadasan, Mr. Santanu Parida, Dr. Arindam Das, Dr. Minisha Mehta, Mr. Shailesh Joshi, Mr. Anees P., Dr. Niranjana Kumar, Mr. Ashok Bahuguna, Mr. Sushil Dubey, Dr. Herojit Loushambam, Dr. T. R. Devidas, Mr. Shashwat Swain

and Mrs. Raktima Basu who had immensely helped in learning various stages of Ph.D. career.

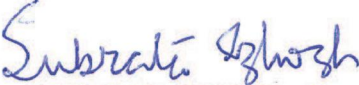
It is my great pleasure to thank Dr. Lukas Albert from Germany, Prof. Zheng Bo from Zhejiang University, China, Prof. Zhipeng Wang from Shishnu University, Japan, Prof. Marta Sevilla from Instituto Nacional del Carbon, Spain, Prof. Luiz Gustavo Cancado from Universidade Federal de Minas Gerais, Brazil, Prof. Victor Krivchenko from Moscow State University, Russia, Dr. Dong Han Seo from University of Sydney, Australia, and Dr. David Aradilla from CEA Grenoble/INAC/SPrAM/PCI, France for fruitful discussion on the subject.

I would not have been able to complete my work without to financial assistance of Dept. of Atomic Energy, Govt. of India. I would like to thank Homi Bhabha National Institute for accepting this dissertation towards Ph.D. degree. I am also thankful to all reviewers and examiner for their time and careful evaluation.

I wish to extend my sincere gratitude to all my teachers, who had taught me at educational career. I am also thanks to my friends, batch mates, and all research scholars.

Above all, I will never have the words of appreciation for my wife, Banashree, my beloved parents, and my whole family, who has shown me that who I am and who I'd like to become.

Thank you all for your love, patience and support to make it possible.

  
SUBRATA GHOSH

## ABSTRACTS

Due to the unique geometry, high surface area, good electrical conductivity and open three-dimensional network, vertical graphene nanosheets (VGN) received strong momentum towards its wide range of applications. To utilize them in potential applications, a clear understanding of the growth mechanism and optimization of growth parameters to achieve desired morphology is highly essential. With this motivation, the present work is addressed towards synthesis and studies of VGN on various substrates and their application towards supercapacitor (SC) electrode.

A systematic study on synthesis of VGN using electron cyclotron resonance - plasma enhanced chemical vapor deposition is carried out. The effect of growth time, feedstock gas composition, growth temperature, microwave power, distance from plasma source to substrate and role of substrates on the growth and structural properties of VGN are addressed. The experimental observations reveal that the morphology can be tuned from vertical to planar structure by changing the growth parameters. Further, direct correlation between XPS and Raman analysis in terms of vacancy-like defects is obtained. Based on the results from influence of feedstock gas compositions, a ternary field diagram clearly demarcating the region of VGN growth is established. A phenomenological four stage growth model is proposed and discussed, to substantiate the defect-induced nucleation and growth mechanism of VGN by invoking substrate-plasma interaction during growth. Formation of defects at early stage nucleation is found to dictate the morphology and structural quality of VGN.

Finally, the electrochemical performance of VGN of optimized morphology and suitable aqueous electrolyte for its effective utilization as a SC electrode is investigated. To explore the capacitive behaviour under various aqueous electrolytes ( $\text{Na}_2\text{SO}_4$ ,  $\text{KOH}$ , and  $\text{H}_2\text{SO}_4$ ), the electrochemical investigation of VGN are carried out using

three electrode system. An electrical equivalent circuit modelling is performed based on electrochemical impedance spectroscopy to elucidate the electrolyte-electrode interaction.  $\text{H}_2\text{SO}_4$  is found to be a choice of electrolyte in terms of specific capacitance, cycle life, efficiency and time constant. Integration of VGN with transition metal oxides (TMO) is a promising approach to further enhance the capacitance of VGN. Due to the fast redox kinetics, less toxicity and less expensive,  $\text{MnO}_2$  is chosen out of TMO and decorated on the surface of VGN. Apart from the enhancement in capacitance of the composite by five times, VGN is found to serve as an excellent mechanical backbone for the effective utilization of  $\text{MnO}_2$  without any structural degradation. The observed results demonstrate that the VGN and its composites can be a potential candidate for SC applications.

# CONTENTS

Synopsis	i
List of Figures	ix
List of Tables	xv
List of Abbreviation	xvii

## **Chapter 1: Introduction**

1.1 Historical overview of graphene	1
1.2 Classification of graphene family	3
1.3 Vertical graphene nanosheets	5
1.3.1 Morphology and structure	5
1.3.2 Properties and applications	5
1.4 Motivation and Research objectives	12
1.5 References	19

## **Chapter 2. Experimental Techniques**

2.1 Introduction	25
2.2 Growth techniques	
2.2.1 Muffle furnace	25
2.2.2 DC sputtering unit	27
2.2.3 Electron Cyclotron Resonance Chemical Vapour Deposition	28
2.3 Morphological characterization	
2.3.1 Field Emission Scanning Electron Microscope (FESEM)	32
2.3.2 Atomic Force Microscopy (AFM)	33
2.4 Structural characterization	

2.4.1 Transmission Electron Microscopy (TEM)	34
2.4.2 Electron Energy Loss Spectroscopy (EELS)	36
2.4.3 Raman Spectroscopy	36
2.4.4 X-ray Photoelectron Spectroscopy (XPS)	38
2.5 Contact Angle Measurement Technique	39
2.6 Fourier Transform Infra-red (FTIR) Spectroscopy	41
2.7 Four Probe Resistive Method	42
2.8 Three Electrode Electrochemical Set up	43
2.9 Summary	45
2.10 Reference	46

### **Chapter 3. Growth Mechanism of Vertical Graphene Nanosheets**

3.1 Introduction	47
3.2 Time dependent growth	
3.2.1 FESEM analysis	48
3.2.2 Disorder induced two-stage growth	49
3.2.3 XPS analysis	54
3.2.4 Electrical properties	57
3.3 Role of feedstock gas composition	
3.3.1 FESEM analysis	58
3.3.2 HRTEM and EELS analysis	63
3.3.3 Raman spectroscopic analysis	65
3.4 Temperature dependent growth	
3.4.1 FESEM analysis	69
3.4.2 Raman spectroscopic analysis	71

3.5 Discussion	72
3.6 Summary	75
3.7 References	76

## **Chapter 4. Tuning Morphology of Vertical Graphene Nanosheets and Study of its**

### **Thermal Stability**

4.1 Introduction	79
4.2 Effect of radical plasma density	
4.2.1 Influence of microwave power	80
4.2.2 Influence of distance from plasma source to substrate	82
4.2.3 Discussion	83
4.3 Homogeneity and uniformity of vertical graphene nanosheets	84
4.4 Effect of substrates	
4.4.1 FESEM analysis	85
4.4.2 Contact angle measurement	86
4.4.3 Raman spectroscopic analysis	88
4.4.4 Discussion	90
4.5 Thermal stability of vertical graphene nanosheets	
4.5.1 FESEM analysis	92
4.5.2 Raman spectroscopic analysis	93
4.5.3 Electrical properties	96
4.5.4 Discussion	96
4.6 Summary	97
4.7 References	98

## **Chapter 5. Electrochemical Performance of Vertical Graphene Nanosheets as Supercapacitor Electrode**

5.1. Introduction	99
5.2. Role of morphology	
5.2.1 FESEM analysis	100
5.2.2 Raman spectroscopic analysis	100
5.2.3 XPS Analysis	101
5.2.4 Electrical properties	101
5.2.5 Cyclic Voltammetry study	102
5.3. Role of different aqueous electrolytes	
5.3.1 Wetting properties	105
5.3.2 Cyclic Voltammetry study	105
5.3.3 Charge-discharge study	107
5.3.4 Electrochemical impedance study	109
5.4. Influence of MnO <sub>2</sub> decoration	
5.4.1 MnO <sub>2</sub> decoration	116
5.4.2 Raman spectroscopic analysis	116
5.4.3 Cyclic Voltammetry study	117
5.4.4 Charge-Discharge study	119
5.4.5 Electrochemical Impedance study	120
5.5. Summary	121
5.6. References	122

## **Chapter 6. Conclusion and Future Prospect**

6.1. Conclusion	123
6.2. Future prospect	123

## Synopsis

The discovery of graphene in 2004, by Prof. A. K. Geim and Prof. K. V. Novoselov, and its remarkable properties has evolved strong research interest in both the academic and industry for their unique. Graphene, the mother of other two dimensional materials, is one atomic thick  $sp^2$  bonded hexagonal honeycomb structure of carbon atoms. This unique structure imparts fascinating properties like high mechanical strength, higher electronic and thermal conductivity, which make it a potential candidate for next generation electronic and optoelectronic devices. Compared to the conventional planar graphene parallel to the substrate, the vertical graphene nanosheet (VGN), also known as carbon nanowalls, is emerging as an important member in the graphene family. The VGN is an interconnected three dimensional open network of graphene sheets of few layers thick, standing perpendicular to the nanographitic (NG) base layer of approximately 10 nm thick. The NG base layer is formed between the substrate and vertical network. While the height of vertical sheets can vary upto several micrometers, the thickness of each sheet is in the range of 2-8 nm. Due to its outstanding properties like high surface to volume ratio, more open space (consists of large distribution in pores), high exposed sharp edge density, excellent conductivity, thermal and chemical stability, the VGN have opened up exciting possibility of wide range of applications such as field emission, energy storage device, gas sensor and bio sensor and biological applications. In addition, this novel nanostructure can be easily functionalized and utilized as templates for growing other class of materials. However, its successful implementation in various fields relies on the suitable synthesis technique to grow the VGN in controllable and scalable fashion.

The large scale production of VGN has become a rapidly developing field towards its commercialization since the first growth reported by Ando *et al.* and followed by Wu *et al.* using plasma enhanced chemical vapor deposition (PECVD). From then onwards, PECVD has emerged as the most promising and easily accessible route for controllable growth of VGN. The major advantages of this technique are high control over the growth, possibility of uniform and homogeneous coating and faster growth rate at low temperature in addition to its environmental friendly nature and compatibility with industrial processes. Various plasma sources including microwave (MW), radio-frequency (RF), direct current (dc) and different strategies have been developed towards high quality VGN growth and understanding its growth mechanism. Although several attempts are devoted to understand its growth mechanism under complex plasma chemistry by controlling the process parameters, still it is an open challenge to the community to come up with an unique and appropriate growth model. Apart from that, several groups have grown planar graphene and VGN using PECVD by controlling feedstock gas composition, independently. Further, a good control over the growth and structure–property relationship are not explored in detail. Hence, this work aims at investigation on the effect of various plasma process parameters likes deposition time, substrate temperature, microwave power, feedstock gas compositions ( $\text{CH}_4$ , Ar, and/or  $\text{H}_2$ ) and distance from plasma source to substrate to shed some light on nucleation and growth mechanism of VGN. This form the first part of the thesis.

The second objective of this thesis is to explore its electrochemical performance. The electrochemical performance, in particular the charge storage capacity, of VGN is mainly based on the electric double layer formation at the interface of VGN and

electrolytes. The morphology with controlled conducting network and nature of electrolytes play the key role on its performance. Hence, this part of the thesis is dericted towards the effect of the morphology and aqueous electrolytes on the electrochemical charge storage capacity of VGN. Although carbon materials are promising candidate for supercapacitors (SC) for their higher power density and long cycle life, their lower energy density limits its commercialization. The capability of easy functionalization allows decoration of the VGN with transition metal. Study on MnO<sub>2</sub> decorated VGN with an aim to enhance its energy density is also included in this part of the thesis.

This thesis is organized into six chapters and the contents of each chapter are summarized below.

### **Chapter 1 – Introduction**

Chapter 1 presents a brief introduction to graphene family. Special attention is paid to the classification of graphene related materials, their structural morphology, properties and potential applications. The state-of-art of VGN growth through literature survey, brief motivation and objective towards optimization of synthesis conditions for controlled growth and their electrochemical performance as SC electrode is addressed in this Chapter.

### **Chapter 2 – Experimental Techniques**

Chapter 2 describes in detail the experimental techniques employed to synthesize and characterize the VGN. The salient features of electron cyclotron resonance (ECR) MWPECVD system, used to grow VGN, are described. The basics

and working principle of scanning electron microscope, atomic force microscope and contact angle measurement used for morphological studies are briefed. The Raman spectroscopy and high resolution transmission electron microscopy (HRTEM) utilized for structural characterization are discussed in detail. This chapter also deals with four probe resistive method used for studying the electrical properties of the VGN and the electrochemical studies of VGN to utilize VGN as a SC electrode.

### **Chapter 3 – Growth Mechanism of Vertical Graphene Nanosheets**

Chapter 3 focuses on understanding the growth of VGN under complex plasma chemistry. The first part of the Chapter presents time dependent growth of VGN on SiO<sub>2</sub>/Si using MW ECR-PECVD. Raman analysis with respect to growth time reveals that two different disorder-induced competing mechanisms contributing to the defect band intensity. The transformation of defects with growth time is in conceptual agreement with a well established amorphization trajectory for graphitic materials. X-ray photoemission spectroscopy studies corroborate well with Raman analysis in terms of defect density and vacancy-like defects for the VGN grown on SiO<sub>2</sub>/Si substrates. Moreover, depending on growth time, the grown VGN exhibit the sheet resistance varying from 30 to 2.17 kΩ/sq. In the second part, by the study on effect dilution of CH<sub>4</sub> with Ar and/or H<sub>2</sub>, it is shown that the morphology of VGN can be tuned to planar nanographitic structure and their intermediates. The findings show that an Ar-rich composition favors VGN while an addition of H<sub>2</sub> to it aids the growth of planar films. Raman analysis reveals the dilution of CH<sub>4</sub> with either Ar or H<sub>2</sub> or Ar + H<sub>2</sub> help to improve the structural quality of the films. Based on the relationship between feedstock gas composition and observed results, a ternary field diagram is established. Line shape

analysis of the Raman 2D bands shows a nearly symmetrical Lorentzian profile which confirms the turbostratic nature of the grown NGS. This aspect is further elucidated by HRTEM studies where an elliptical diffraction pattern is observed. The third part deals the temperature dependent growth of VGN. It is also shown that an increase in substrate temperature, during growth, leads to grow VGN from the continuous nanographitic structure. The activation energy of the VGN grown by PECVD is found to be 0.57 eV. At the end of this Chapter, a phenomenological four-stage model is discussed, to substantiate the nucleation and growth mechanism of VGN on different substrates, by invoking substrate–plasma interaction.

#### **Chapter 4 –Tuning Morphology of Vertical Graphene Nanosheets and Study of its Thermal Stability**

The present Chapter describes the ability of tuning the morphology of VGN by varying MW power, distance from plasma source to substrates and substrates. This comprises the plasma chemistry, nucleation, growth and parallel etching process. The first part of this chapter deals with how the plasma parameters like MW power and distance from plasma sources to substrate influence the density and energy of the plasma species and plasma size, which determine the surface reaction kinetics that governed the final structure and morphology of VGN. The second part addresses the role of substrate on the change in morphology and structure of VGN. To this effect, the VGN are grown on various substrates like Pt, Ni, Au, Cu, Si(100), Si(111), SiO<sub>2</sub> and quartz simultaneously. The significant morphological variation is found in VGN grown on different substrates. VGN on Pt have the highest aerial density of vertical sheets while quartz have the lowest. The structural defects in VGN vary with substrate as

evidenced from Raman spectroscopy. The observation of defect related Raman bands such as D' and D\* at 1150 and 1500  $\text{cm}^{-1}$ , respectively confirm the existence of pentagon–heptagon rings or carbon onions in VGN. Formation of such defects at early stage of nucleation dictates the growth mechanism and hence the morphology. It has shown that the substrate properties like surface energy thermal conductivity and atomic density play major role in deciding the different form of VGN. Such understanding on growth of VGN is not only useful for growth mechanism under plasma chemistry but also beneficial to get controlled and desired structure suitable for various applications. In addition, the thermal stability of VGN, which is one of the desired characteristics of material to use them for device application, is addressed in the last part of this Chapter.

## **Chapter 5 – Electrochemical Performance of Vertical Graphene Nanosheets as Supercapacitor Electrode**

The present Chapter demonstrates that both the electrochemical charge storage capacity and transport mechanism of VGN can be improved by controlling growth morphology and using different electrolytes. The electrochemical properties and capacitance measurement of the VGN electrodes are carried out using three-electrode system. The VGN with more open network and high conductivity show better electrochemical performance in 1M  $\text{H}_2\text{SO}_4$  electrolyte. The second part of this Chapter describes the electrochemical performance of VGN electrode in various aqueous electrolyte mediums, like 1M  $\text{Na}_2\text{SO}_4$ , 1M  $\text{H}_2\text{SO}_4$  and 1M KOH. The  $\text{H}_2\text{SO}_4$  medium shows better electrochemical performance of capacitance ( $188 \mu\text{F}/\text{cm}^2$  at 100 mV/s) with 96.8% retention and almost no deterioration in impedance spectra even after 200 cycles. The charge storage capacity is investigated by the help of electrochemical

impedance spectroscopy and equivalent circuit modeling. The last part discusses the possibility of enhancing the electrochemical performance of the device by decorating MnO<sub>2</sub> on VGN. This hybrid structure exhibited a higher specific capacitance than that of VGN. The enhanced capacitance is attributed to effective utilization of MnO<sub>2</sub> coating on conductive 3D network of VGN. These results provide important scientific findings necessary for fabricating energy storage devices based on VGN with superior electrochemical performances.

## **Chapter 6 – Conclusion and Outlook**

This Chapter summarizes the major findings of the current thesis and some possible directions for future work on VGN are proposed.



## List of Figures

Figure 1.1	Timeline of selected events leading to the discovery of graphene (Ref 1)	1
Figure 1.2	(a) Unit cell, (b) schematic of in-plane $\sigma$ -bond and out-of-plane $\pi$ -bond, (c) band-energy diagram of the graphene and (d) graphene as building block of fullerene(0D), carbon nanotube(1D), and graphite(3D)	2
Figure 1.3	Schematic of (a) graphene oxide, (b) graphene nanoribbons with arm-chair and zig-zag edges and (c) graphane	4
Figure 1.4	(a)schematic of vertical graphene nanosheets (VGN) and (b) number of publication <i>vs</i> year of publication on VGN, upto April 2016	5
Figure 1.5	Possible ways of decoration on VGN: (a) conformal deposition, (b) gap filling, (c) deposition on the top edges, and (d) dispersed nanoparticle deposition (Ref. 19)	7
Figure 1.6	Schematic of various applications of VGN (images are taken from the corresponding references given in text)	11
Figure 2.1	(a) Schematic of muffle furnace, and (b) typical temperature profile maintained for the growth of SiO <sub>2</sub> on Si substrate	26
Figure 2.2	(a) Schematic of sputtering process, (b) DC-sputtering for thin film deposition, and (c) plot of sputtering yield <i>vs</i> normalized ion energy	28
Figure 2.3	A chronology of carbon nanostructure prepared by PECVD technique	29
Figure 2.4	(a) A schematic of ECR-CVD set up, (b) Schematic of ECR-principle and (c) typical growth profile of VGN	30
Figure 2.5	(a) schematic diagram of FESEM, (b) interaction force <i>vs</i> distance between tip and sample, and (c) schematic diagram of AFM	33
Figure 2.6	A schematic of transmission electron microscopy (TEM)	35

Figure 2.7	Schematic view of (a) scattering process in material with incident light, and (b) Raman spectrometer set up	37
Figure 2.8	(a) Schematic view of X-ray induced photoelectron emission process, and (b) block diagram of X-ray photoelectron spectroscopy	38
Figure 2.9	(a) Schematic of contact angle (CA) formed by sessile liquid drop on smooth homogeneous solid surface, (b) table of CA with wetting property, and (c) Contact angle measurement set up in our lab	40
Figure 2.10	A block diagram of Fourier transform infra-red spectroscopy	42
Figure 2.11	(a) Four point probe contact on the arbitrary shape of the material, and (b) the van der Pauw correction factor, $F$ vs $R_T$ (Ref. 10)	43
Figure 2.12	(a) Schematic of three-electrode system, and (b) block diagram of potentiostat/galvanostat	44
Figure 3.1	FESEM micrographs of the VGN grown at different duration of (a) 10 sec, (b) 1 min (c) 5 min, (d) 10 min, (e) 20 min, and (f) 45 min. Inset of Figure (c-f) represent corresponding cross-sectional FESEM micrograph of the film.	49
Figure 3.2	(a) First order and (b) second order typical Raman spectrum of VGN and its deconvolution with Lorentzian line shape, (c) vertically stacked up of Raman spectra of VGN at different growth duration of 10 sec, 1, 5, 10, 20, and 45 min, (d) FWHM of D, G, and G' bands, (e) variation of G-band position, (f) $I_{G'}/I_G$ with respect to growth time and (g) plot of $I_D/I_G$ vs $I_{D'}/I_G$ for VGN. Connecting solid lines in Fig. 4(d-f) are guide to eye.	51
Figure 3.3	(a) Variation of $I_D/I_G$ with respect to growth time, (b) plot of $L_D$ vs $I_D/I_G$ and inset represents the schematic definition of “activated” A-region and “structurally-disordered” S-region according to Lucheese’s model (Ref. 7), (c) calculated defect density with growth time for the VGN. The solid line in the Fig. 3.3(b) is fit to the experimental data along with simulated curve with the same fitting parameters ( $0 < L_D < 50$ nm). The fitting is performed using Eqn. (5). Solid line in the Fig. 3.3(a and c) is guide to eye	53

- 
- Figure 3.4 (a) The high resolution C1s spectra for the films grown for 10 sec, 10 min, and 45 min, The inset in Fig. (a) is an extended region of C1s at higher BE, (b) deconvulated C1s spectrum for the film grown for 10 min, and (c) the Si2p XPS spectrum for 10 s grown film 55
- Figure 3.5 (a) FTIR spectra and (b) variation of sheet resistance vs growth time of VGN. Solid line in Fig. (b) is a guide to eye. Inset represents the Ohmic behavior of VGN grown at 10 sec and 45 min 57
- Figure 3.6 FESEM micrographs of VGN grown at different CH<sub>4</sub>:Ar:H<sub>2</sub> ratios: (a) 1:0:0, (b) 1:1:0, (c) 1:3:0, (d) 1:5:0, (e) 1:7:0 and (f) cross-sectional FESEM images of (b–e) with a 100 nm scale bar 59
- Figure 3.7 FESEM micrographs of a few layer planar nanographite films grown at different CH<sub>4</sub>:Ar:H<sub>2</sub> ratios (a) 1:0:1 (b) 1:0:3 (c) 1:0:5 and (d) 1:0:7 59
- Figure 3.8 (a-i) FESEM micrographs of NGS grown under mixed Ar+H<sub>2</sub> dilution. The actual gas flow ratios are labeled on each image as CH<sub>4</sub>:Ar:H<sub>2</sub>, Insets represent cross-sectional FESEM image of respective film 61
- Figure 3.9 A tentative ternary field diagram indicating the growth of various NGS morphologies under different feedstock ratios 61
- Figure 3.10 (a) and (b) HRTEM micrographs, (c) FFT of (b) and (d) EELS of the sample grown with the composition of 1:7:0. (e) and (f) HRTEM image, (g) FFT of (b) and (d) EELS of the sample grown with the composition of 1:0:5. 64
- Figure 3.11 Raman spectra of NGS grown at different conditions by diluting (a) CH<sub>4</sub> with increasing Ar [case I], (b) CH<sub>4</sub> with increasing H<sub>2</sub> [case II], (c) CH<sub>4</sub>+5 sccm of H<sub>2</sub> with increasing Ar [case IIIa], (d) CH<sub>4</sub>+5 sccm of Ar with increasing H<sub>2</sub> [case IIIb], and (e) increasing CH<sub>4</sub> concentration with fixed Ar and H<sub>2</sub> ratio [case IIIc]. Raman spectra are normalized with G band intensity of the respective curve and linearly shifted in the y-axis for clarity. The actual flow rates in sccm are given in the plots. (f) A Lorentzian fit (solid line) of G'-band of NGS grown with different feedstock gas compositions along with highly oriented pyrolytic graphene 67

---

Figure 3.12	FESEM micrograph of the sample grown at (a) 600 °C, (b) 625 °C, (c) 625 °C (cross section image), (d) 650 °C, (e) 725 °C and (f) 800 °C. (g) Arrhenius plot of the growth rate <i>vs</i> inverse substrate temperature and (h) Water contact angle <i>vs</i> growth temperature of VGN	71
Figure 3.13	(a) Raman spectra of temperature dependent growth of VGN, (b) FWHM of D, G, G'), and $I_D/I_G$ <i>vs</i> growth temperature, and (c) position of G band and $I_D/I_G$ <i>vs</i> growth temperature.	72
Figure 3.14	A phenomenological four stage growth model of VGN	74
Figure 4.1	FESEM micrographs of VGN grown at MW power of (a) 200 W, (b) 250 W, (c) 320 W, (d) 375 W, (e) 425 W and (f) 475 W; (g) variation of growth rate, (h) stack of Raman spectra, and (i) $I_D/I_G$ of VGN with respect to MW power.	81
Figure 4.2	FESEM micrographs of VGN grown at a distance from plasma source of (a) 40 cm, (b) 30 cm, (c) 20 cm and (d) 10 cm; (e) variation of growth rate, (f) stack of Raman spectra, (g) variation in FWHM of D, G and G' band, and (h) variation in $I_D/I_G$ of VGN with respect to distance	82
Figure 4.3	(a) Optical image of VGN grown on Cu substrate, (b) FESEM micrographs of VGN, (c) variation in FWHM and position of D, G and G' band with respect to the axis (a, b and c)	84
Figure 4.4	FESEM micrographs of VGN grown on (a) Pt, (b) Ni, (c) Si(111), (d) Si(100), (e) Au/Si, (f) Cu, (g) SiO <sub>2</sub> , and (h) quartz substrates	86
Figure 4.5	Water contact angle of Si(100) (a) before growth, and (b) after growth of VGN	87
Figure 4.6	(a) Raman spectra, and (b) closer view of first order Raman spectra of VGN grown on various substrates	89
Figure 4.7	FESEM micrographs of (a) as-grown, and (b) 16 hrs annealed VGN. Inset represents corresponding cross sectional FESEM micrographs	92

---

Figure 4.8	(a) Raman spectra of as-grown and annealed VGN, (b) FWHM and (c) position of D, G, G' bands of VGN as a function of annealing time	93
Figure 4.9	(a) Variation of $I_D/I_G$ with annealing time, (b) FWHM of G band vs $I_D/I_G$ , (c) variation of $I_D/I_G$ and (d) $I_{G'}/I_G$ as a function of annealing time. Solid lines are guide to eye	94
Figure 4.10	Schematic of edge fragmentation of graphene upon annealing (Ref 19)	95
Figure 5.1	FESEM micrographs of VGN electrode grown under different process parameters. Insets represent corresponding cross sectional FESEM micrographs of VGN.	100
Figure 5.2	(a) Raman spectra, and (b) Photoemission signal of VGN1 and inset represents the C1s of VGN1	101
Figure 5.3	Cyclic voltammogram (CV) of (a) VGN1, (b) VGN2, and (c) VGN3 at different scan rates in the range of 50-500 mV/s in 1M H <sub>2</sub> SO <sub>4</sub> electrolyte, (d) comparison of CV of Si and VGN/Si at 20 mV/s scan rate, and (e) plot of specific capacitance vs scan rate for VGN	103
Figure 5.4	Time dependent wettability of VGN3 in 1M Na <sub>2</sub> SO <sub>4</sub> , 1M KOH, and 1M H <sub>2</sub> SO <sub>4</sub> electrolyte medium	105
Figure 5.5	Cyclic voltammogram of VGN3 in (a) 1M Na <sub>2</sub> SO <sub>4</sub> , (b) 1M KOH, and (c) 1M H <sub>2</sub> SO <sub>4</sub> medium at scan rate ranges 100, 200, 300, 400, 500 mV/s. (d) Specific capacitance vs scan rate of VGN3 in different aqueous electrolytes	106
Figure 5.6	Charge-discharge profile of VGN at different current density in (a) 1M Na <sub>2</sub> SO <sub>4</sub> , (b) 1M KOH, and (c) 1M H <sub>2</sub> SO <sub>4</sub> , and (d) capacitance retention vs cycle number of VGN3 in different aqueous electrolytes	108
Figure 5.7	(a) Phase angle versus frequency (Bode plot), and (b) evolution of the imaginary part of the complex capacitance vs frequency of VGN3 in various electrolyte systems	110

---

Figure 5.8	Nyquist plot of VGN3 in (a) 1M Na <sub>2</sub> SO <sub>4</sub> , (b) 1M KOH, and (c) 1M H <sub>2</sub> SO <sub>4</sub> spectra before and after 200 charge-discharge cycles. Inset of panels in (a), (b), (c) represents the expanded high frequency Nyquist plot and solid line indicates fitted data using equivalent circuit [Fig. 5.9(b)]	112
Figure 5.9	(a) Simple Randles circuit, and (b) electrical equivalent circuit for VGN3 electrode in aqueous medium	113
Figure 5.10	(a) Raman spectra, and (b) FWHM of D/G/G' of pristine VGN3 and after electrochemical experiment in 1M Na <sub>2</sub> SO <sub>4</sub> , 1M KOH and 1M H <sub>2</sub> SO <sub>4</sub>	115
Figure 5.11	Raman spectra of VGN3 and MnO <sub>2</sub> /VGN3	117
Figure 5.12	Cyclic voltammogram (CV) of MnO <sub>2</sub> /VGN3 in (a) 1M Na <sub>2</sub> SO <sub>4</sub> and (b) 1M H <sub>2</sub> SO <sub>4</sub> at scan rates of 100-500 mV/s, respectively; (c) comparative CV of VGN3 in 1M H <sub>2</sub> SO <sub>4</sub> , MnO <sub>2</sub> /VGN3 in 1M Na <sub>2</sub> SO <sub>4</sub> and MnO <sub>2</sub> /VGN3 in 1M H <sub>2</sub> SO <sub>4</sub> at scan rate of 100 mV/s; (d) Specific capacitance vs scan rate of VGN3 in 1M H <sub>2</sub> SO <sub>4</sub> , MnO <sub>2</sub> /VGN3 in 1M Na <sub>2</sub> SO <sub>4</sub> and MnO <sub>2</sub> /VGN3 in 1M H <sub>2</sub> SO <sub>4</sub>	118
Figure 5.13	Charge-discharge profile of MnO <sub>2</sub> /VGN3 in (a) 1M Na <sub>2</sub> SO <sub>4</sub> and (b) 1M H <sub>2</sub> SO <sub>4</sub> at current density in the range of 5-25 μA/cm <sup>2</sup> , respectively; (c) comparative charge-discharge profile of VGN3 in 1M H <sub>2</sub> SO <sub>4</sub> , MnO <sub>2</sub> /VGN3 in 1M Na <sub>2</sub> SO <sub>4</sub> and MnO <sub>2</sub> /VGN3 in 1M H <sub>2</sub> SO <sub>4</sub> at current density of 5 μA/cm <sup>2</sup> ; and (d) capacitance retention vs cycle number of VGN3 in 1M H <sub>2</sub> SO <sub>4</sub> , MnO <sub>2</sub> /VGN3 in 1M Na <sub>2</sub> SO <sub>4</sub> and MnO <sub>2</sub> /VGN3 in 1M H <sub>2</sub> SO <sub>4</sub>	120
Figure 5.14	Nyquist plot of VGN3 in (a) 1M Na <sub>2</sub> SO <sub>4</sub> , (b) 1M KOH, and (c) 1M H <sub>2</sub> SO <sub>4</sub>	121

## List of Tables

Table 1.1	Comparison of physicochemical properties of various SC materials (Ref. 107)	16
Table 1.2	Comparison of different carbon materials and their properties in EDLC electrodes (Ref. 110)	16
Table 1.3	Comparison of capacitance values of VGN under different aqueous electrolytes reported in the literature	18
Table 2.1	Typical parameters of arc-discharge, Radio-Frequency and Microwave plasmas used for the nanofabrication (Ref. 4)	29
Table 3.1	Experimental parameters for time dependent growth of VGN	48
Table 3.2	Types of defects in graphitic structure based on $I_D/I_G$ ratio (Ref. 9,10)	51
Table 3.3	Extracted parameters from XPS analysis for the VGN	56
Table 3.4	Deposition parameters for VGN growth by ECRCVD under different feedstock gas composition	58
Table 3.5	Extracted parameters from Raman analysis for different NGS. The topography of the nanostructures are classified as isolated nanoclusters (IN), vertical (V) and planar (P) structures as given in morphology column. The symbol '*' in column ' <i>h</i> ' represents thickness measured by AFM and others values are measured by FESEM and ' <i>d</i> ' represents a discontinuous film	68
Table 3.6	Experimental parameters for temperature dependent growth of VGN	69
Table 4.1	Experimental parameters to tune radical plasma density for VGN growth	80
Table 4.2	Experimental parameters for VGN on Cu substrate	84
Table 4.3	Experimental parameters for VGN on different substrates	85

---

Table 4.4	The extracted parameter of contact angle measurement of different surfaces before and after growth of VGN, <i>rms</i> roughness of pre-cleaned substrates and their respective thermal conductivity from literature	87
Table 4.5	Extracted parameters of Raman spectra of VGN grown on different substrates	89
Table 5.1	Growth conditions for VGN electrode of different morphology	99
Table 5.2	Extracted physical parameters of VGN	102
Table 5.3	Characteristic parameters of ions of the distinct aqueous electrolyte (Ref. 12,13)	107
Table 5.4	Extracted parameters of equivalent circuit of VGN under different aqueous electrolytes obtained through EIS spectrum analyser	114
Table 5.5	Comparison of electrochemical performance of VGN in various aqueous electrolytes	114
Table 5.6	Extracted parameters of Raman analysis of VGN3 and MnO <sub>2</sub> /VGN3	117

## List of Abbreviations

0D	Zero Dimensional
1D	One Dimensional
2D	Two Dimensional
3D	Three Dimensional
AFM	Atomic Force Microscopy
BE	Binding Energy
CA	Contact Angle
CNF	Carbon Nanofiber
CNT	Carbon Nanotube
CV	Cyclic Voltammogram
ECR	Electron Cyclotron Resonance
EDLC	Electric Double Layer Capacitance
EELS	Electron Energy Loss Spectroscopy
EIS	Electrochemical Impedance Spectroscopy
FESEM	Field Emission Scanning Electron Microscope
FFT	Fast Fourier Transform
FWHM	Full Width at Half Maximum
FPNG	Few Layer Planar Nanographite
GO	Graphene Oxide
GNR	Graphene Nanoribbons
GQD	Graphene Quantum Dots
HD	High Defect
HOPG	Highly Oriented Pyrolytic Graphite
HRTEM	High Resolution Transmission Electron Microscopy
LD	Low Defect
MFC	Mass Flow Controller
MW	Microwave
ND	Nanocrystalline Diamond
NG	Nanocrystalline Graphitic film
NGSs	Nanographitic Structures
PECVD	Plasma Enhanced Chemical Vapor Deposition

PL	Photoluminescence
<i>rms</i>	Root Mean Square
SAED	Selected Area Electron Diffraction
SC	Supercapacitor
ta-C	tetrahedral amorphous carbon
UNCD	Ultracrystalline Diamond
VGN	Vertical Graphene Nanosheets
XPS	X-Ray Photoelectron Spectroscopy

# 1

## Introduction

*Without carbon, life cannot exist*

The remarkable properties of graphene and graphene related structures have drawn significant attention of academic and industrial community. This Chapter will provide, in brief, the historical background, classification of graphene family and highlights of current research on vertical graphene nanosheets, one of interesting structures of graphene family. Moreover, motivation and roadmap of the thesis work is framed.

## 1.1 Historical overview of graphene

Graphite, a layered structure of  $sp^2$  bonded carbon network, has drawn significant attention during the past decades in various fields of research and industrial application. The theoretical and experimental research was continued towards how to peel off single layer from the layered structure of graphite, their stability as a structure and its properties. “Carbon, the basis of all known life on earth, has surprised us once again” through “groundbreaking experiments regarding the two-dimensional material graphene”. That fetched Nobel Prize in the year of 2010. Figure 1.1 shows the timeline of selected events to the discovery of graphene.<sup>1</sup>

1840-1958: Graphite oxide by Schafhaeutl, Brodie, Staudenmaier, Hummers and others
1930: Landau and Peierls: 2D crystals were thermodynamically unstable
1940: Theoretical analyses suggested that graphite layers—if isolated—might exhibit extraordinary electronic characteristics
1947: Wallace - The band theory of graphite → graphene
1955: Lomer - Group theory
1956: McCure - Electrons can be described as Dirac-fermions with zero mass
1962: Bohem et al. prepare reduced graphite oxide by chemical and thermal reduction of graphite oxide.
1970: Blakley <i>et al.</i> - monolayer graphite by segregating C on surface of Ni(100)
1975: van Bommel <i>et al.</i> - prepare monolayer graphite by subliming Si from SiC.
1986: Bohem <i>et al.</i> recommend the name ‘GRAPHENE’
1997:IUPAC–The term graphene should be used only when the structural relations or other properties of individual layers are discussed”
1999:Ruoff <i>et al</i> - micromechanically exfoliate graphite into thin lamellae comprised of multiple layers of Graphene
2004: Geims and Novoselov - first experimental observation of 2D graphite layer
2006: Somani <i>et al.</i> - Planer nano-graphenes from camphor by CVD

Figure 1.1: Timeline of selected events leading to the discovery of graphene (Ref. <sup>1</sup>)

Graphene is a two-dimensional (2D) honeycomb structure with one atomic layer of  $sp^2$  carbon. The thickness of graphene is 0.335 nm. The unit cell of graphene contains two

carbon atoms (A and B) with C-C bond length of 0.142 nm [Fig. 1.2(a)]. Each carbon atom has four bonds, three in-plane  $\sigma$ -bonds with the neighboring carbon atoms and one out-of-plane  $\pi$ -bond [Fig. 1.2(b)]. The  $\sigma$ -bond is responsible for the mechanical backbone, whereas the  $\pi$ -bond provides the good electrical conductivity in the plane. In addition, it is a zero-band gap semiconductor due to the linear relationship of energy-momentum, where conduction and valence bands meet at Dirac Point [Fig. 1.2(c)]. Thus the graphene has intriguing properties such as

- Zero band gap semiconductor with mobility of  $10,000\text{--}2,00,000\text{ cm}^2\text{V}^{-1}\text{s}^{-1}$
- Highest current density at room temperature (  $10^6$  times than that of Cu)
- Stiffest material, high Young's Modulus of 1TPa and intrinsic strength of 130 GPa
- Most stretchable, pliable and thinnest material with surface area of  $2,630\text{ m}^2/\text{g}$
- Longest mean free path at room temperature (  $\sim$  microns)
- Superior thermal conductivity ( $5000\text{ W/mK}$ ) and negative thermal expansion coefficient
- Exceptional optical properties with 97% transparency
- Chemically inert, bio-compatible and impermeable (even for He)

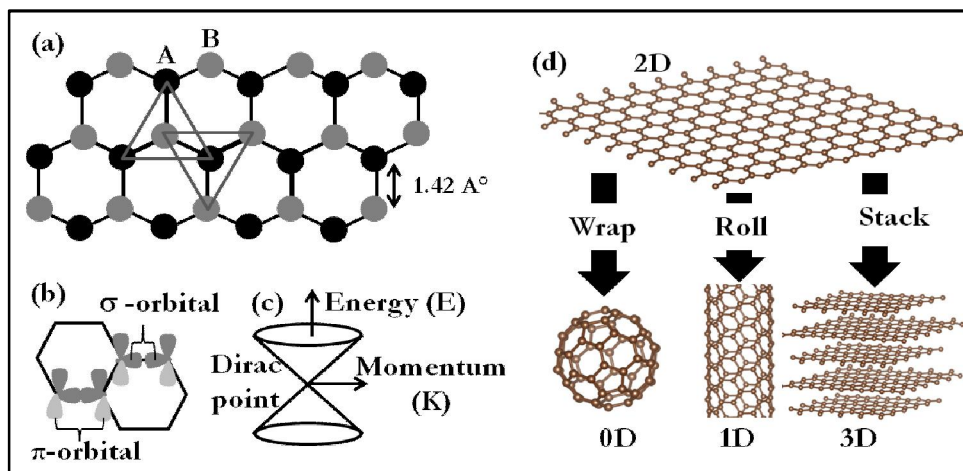


Figure 1.2: (a) Unit cell, (b) schematic of in-plane  $\sigma$ -bond and out-of-plane  $\pi$ -bond, (c) band-energy diagram of graphene and (d) Graphene (2D) as building block of fullerene (0D), carbon nanotube(1D) and graphite(3D)

Tunability into various shapes makes graphene the mother of all  $sp^2$  hybridized structures. By stacking, rolling or wrapping, graphene (2D) can be transformed into graphite (3D), carbon nanotubes (1D) and fullerene (0D), respectively [Fig. 1.2(d)].

## 1.2 Classification of graphene family

Based on the existing structure and morphology, the graphene family is divided into several classes as follows:<sup>2,3</sup>

### *a. Graphene*

A single layer of  $sp^2$  bonded hexagonal carbon network, is known as single layer graphene or simply graphene [Fig. 1.2(d)]. The lateral dimension can vary upto any length scale. It can be freely suspended or laid parallel to the substrates. Depending on number of layers ( $n$ ), planar graphene can be classified into bi-layer graphene ( $n=2$ ), tri-layer graphene ( $n=3$ ), few layer graphene ( $2 < n < 5$ ) or multilayer graphene ( $n \leq 10$ ).

### *b. Graphene Oxide (GO)*

Graphene oxide is the chemically modified graphene, where carbon to oxygen atomic ratio is less than 3 [Fig. 1.3(a)]. The oxygen content can be reduced further and called as reduced graphene oxide (rGO).

### *c. Vertical Graphene Nanosheets (VGN)*

Compared to lying down or being parallel to the substrate, vertically standing graphene on the substrate is called as vertical graphene. Vertical graphene nanosheets (VGN) is composed of three-dimensional network structure of vertical sheets and each

sheets contains few layer graphene. It is also known as carbon/graphene nanowalls/nanosheets, carbon nanospikes, few layer graphene, graphite petals, free standing graphene or vertically oriented graphene.

#### **d. Graphene Nanoribbons (GNR)**

The graphene nanoribbons (GNR) is a single layer graphene with width less than or equal to 50 nm. Depending on the edges of GNR, again it can be classified into zig-zag or armchair, as shown in Fig. 1.3(b).

#### **e. Graphene Quantum Dots (GQD)**

It consists of few layer graphene with size less than 10 nm. GQD has intrinsic properties like low toxicity, chemical stability, and it shows stable photoluminescence and quantum confinement effect.

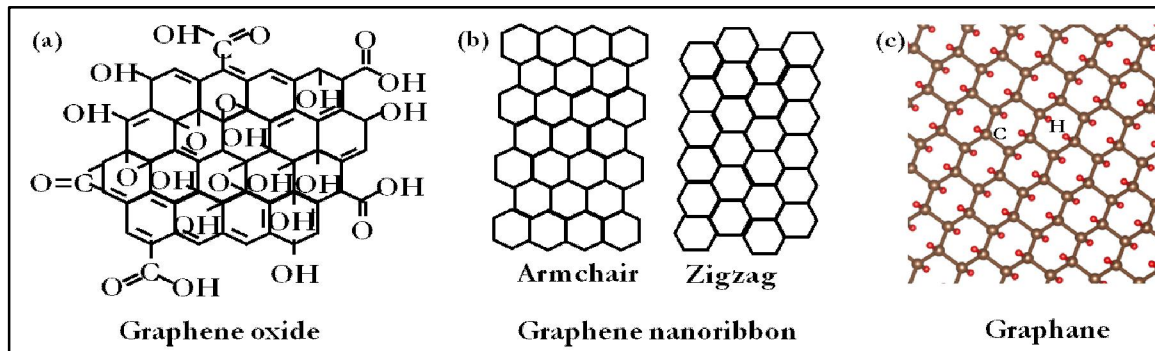


Figure 1.3: Schematic of (a) graphene oxide, (b) graphene nanoribbons with arm-chair and zig-zag edges, and (c) graphane

#### **f. Hydrogenated Graphene**

A fully hydrogenated form of graphene is known as graphane, which is non-magnetic in nature with band gap of 4.5 eV [Fig. 1.3(c)]. The semi-hydrogenated graphene is called graphone, which is ferromagnetic in nature with band-gap of 0.46 eV.<sup>4</sup>

## 1.3 Vertical graphene nanosheets

### 1.3.1 Morphology and structure

The schematic of VGN is shown in Fig. 1.4(a). Generally, vertical sheets are interconnected, making a maze-like open 3D network. The thickness is in nanometer scale whereas the length and height of these sheets can vary up to several micrometers. The increasing trend of number of publications on VGN emphasizes the impact of this structure, which is depicted in Fig. 1.4(b).

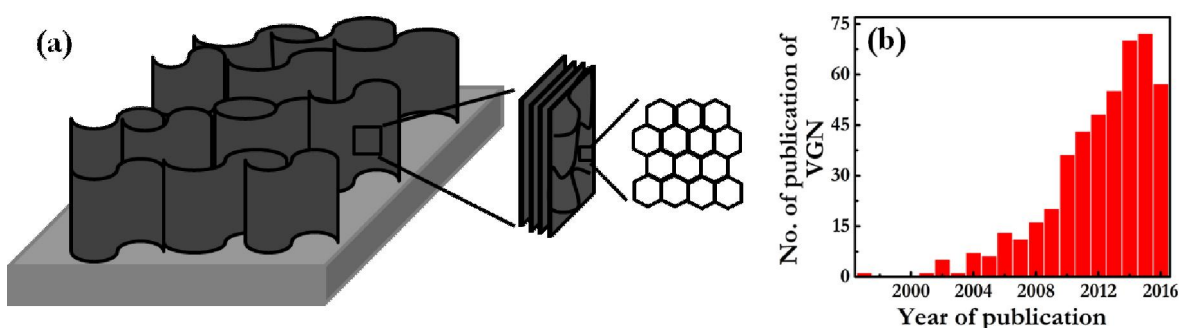


Figure 1.4 (a) schematic of VGN, and (b) number of publication vs year of publication on VGN, upto October 2016

### 1.3.2 Properties and applications

The fascinating properties of VGN open up a new window for wide range of applications. The basic properties of this novel architecture are as follows:

#### *Wetting properties*

The water contact angle (CA) of VGN is found to be in the range of 130-140° which ensures it's near superhydrophobic nature. The average surface energy obtained was 33 mJ/m<sup>2</sup>, which is one of the lowest reported value for graphene related structure.<sup>5</sup> The wetting property can be tuned from superhydrophobic to superhydrophilic by modifying surface defect, varying the growth parameters or using post synthesis plasma treatment.<sup>6-9</sup>

### *Surface area*

The VGN shows high nitrogen Brunauer-Emmett-Teller specific surface area of  $\sim 1800 \text{ m}^2/\text{g}$ , one of the crucial parameters to use them for electrochemical purpose.<sup>10</sup> The observed value is closest to the theoretical value of surface area of graphene ( $2630 \text{ m}^2/\text{g}$ ).

### *Thermal properties*

The thermal conductivity of VGN is found to be  $480 \text{ W/mK}$ , which is significantly lower than that of suspended single layer graphene ( $5300 \text{ W/mK}$ ). This is due to leakages of phonons through the VGN-Cu interface and scattering of phonon by edge defects.<sup>11</sup>

### *Stability*

The VGN demonstrate excellent thermal stability with less than 3% weight loss upto  $800 \text{ }^\circ\text{C}$  under  $\text{N}_2$  environment.<sup>12</sup> Whereas high temperature annealing ( $1200\text{-}3000 \text{ }^\circ\text{C}$ ) modifies the structure slightly.<sup>13</sup>

Wu *et al.*<sup>14</sup> showed the structural and morphological stability of VGN under harsh X-ray environment, to test their potential application as a cold cathode, even in the space. Wang *et al.*<sup>15</sup> demonstrated the reproducibility and stability of VGN over 200 hrs of cycle operation at  $1.3 \text{ mA}$  current emission. The excellent stability of structure was also confirmed by Jiao *et al.*<sup>16</sup> through the PMMA/Graphene/VGN/Si solar cell experiment.

It is also possible to preserve its internal structure and architecture in acid solution, water and alcohol environment.<sup>17,18</sup>

### *Capability of functionalization*

Owing to hydrogen terminated edges, the capability of decorating nanoparticles and

functionalization of VGN open up another pathway for their application with improved performance. The decoration can be performed via conformal deposition, gap filling, deposition on the top edges of VGN and dispersed nanoparticle deposition, as shown in Fig. 1.5(a-d).<sup>19</sup> The following examples show the enhancement of properties of VGN by decoration or functionalization by hetero-atoms.

- Si, SnO<sub>2</sub>, TiO<sub>2</sub>, and GeO<sub>x</sub> decoration for Li-ion battery,<sup>20-23</sup>
- Adsorption-induced functionalization or functionalization by metal oxide (MnO<sub>2</sub>, V<sub>2</sub>O<sub>5</sub>, NiO, Co<sub>3</sub>O<sub>4</sub>), Ni(OH)<sub>2</sub> for supercapacitor (SC) electrode,<sup>10,24-26</sup>
- Pt nanoparticles decoration for methanol electro-oxidation,<sup>27</sup>
- Functionalization by single-strand DNA for bio-sensor application,<sup>28</sup>
- Decoration with Ag for enhancement of gas sensing properties,<sup>29</sup>
- Decoration of TiO<sub>2</sub> for photocatalytic ability,<sup>30</sup>
- Ag and Au nanoparticles decoration for surface enhanced Raman spectroscopy (SERS) substrates,<sup>31,32</sup>
- It is also used as template for oxide, magnetic and metallic nanostructure,<sup>33</sup>
- Composites with carbon nanotube (CNT), MoSe<sub>2</sub> for specific applications,<sup>34,35</sup>

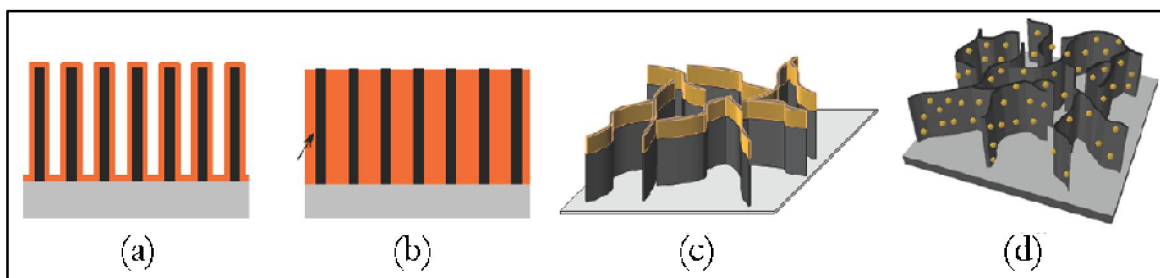


Figure 1.5: Possible ways of decoration on VGN: (a) conformal deposition, (b) gap filling, (c) deposition on the top edges, and (d) dispersed nanoparticle deposition (Ref. <sup>19</sup>)

### *Optical properties*

The VGN shows low reflectance (up to 0.13%) and high specific absorption

( $6600 \text{ g}^{-1} \text{ cm}^2$ , higher than CNT forest) in the visible range of 400–1000 nm.<sup>36</sup> Even the absorption properties of VGN are found to be independent of polarization of incident radiation and only 2% of light is reflected.<sup>17</sup> The transmittance of VGN on glass substrate decreases with the vertical height and it is found to be 42.44% for a film of 1.2  $\mu\text{m}$  height.<sup>37</sup> The refractive index, extinction co-efficient and optical band gap of VGN are reported to be 1.2-1.5, 0.1-0.5, and 0.2 eV, respectively.<sup>38</sup>

In addition, VGN shows three strong photoluminescence (PL) bands centered about 408, 526 and 699 nm. These bands are due to the chemical radicals terminated on the VGN and the transitions between the  $\sigma^*$ - $\pi$  bands,  $\pi^*$ - $\pi$  bands, and  $\pi^*$  band - oxygen-defect states, respectively.<sup>39</sup> Also tunable PL can be achieved by incorporation of  $\text{N}_2$  or  $\text{O}_2$  into the structure making it useful for optoelectronic devices.<sup>40</sup>

#### *Field emission properties*

Uniform morphology and sharp edges of VGN ensured their capability as a potential candidate for field electron emitters.<sup>41</sup> The emission properties can be further improved by sharpening the edges, introducing more defect sites and increasing the emission sites, which leads to reduction in screening effect and thus decreasing the field strength. This can be performed by controlled growth, X-ray irradiation<sup>14</sup> and Ar<sup>42</sup> or  $\text{N}_2$ <sup>43</sup> plasma treatment. The enhancement of turn-on field and threshold field by X-ray irradiation in VGN is due to the increased work function induced by oxygen functional group on the surface.<sup>14</sup>

#### *Electrical properties*

The electrical properties of VGN are semimetal in nature.<sup>44</sup> From Hall measurement, the VGN are found to be *p*-type semiconductor.<sup>45</sup> The semiconducting

nature of VGN is due to the presence of structural disorder (edges, ripples, bends and branches) in the film.<sup>46</sup> The type of carrier can be changed to *n*-type by N-incorporation into the structure. The N-incorporation into the structure can be performed either during growth or post treatment. Takeuchi *et al.*<sup>47</sup> have shown that the carrier density increases and mobility decreases with the N-content during the growth, where C<sub>2</sub>F<sub>6</sub> was used as carbon source. The role of F in the electrical properties is not reported in their study. On the other hand, N<sub>2</sub> plasma post treatment reveals opposite result in mobility and carrier density with increasing post treatment time, but *p*-type conduction remain unchanged.<sup>48</sup> It is also observed that the electrical properties of VGN can switch over from semiconducting to metallic by thinning down the thickness of vertical sheets.<sup>49</sup> Moreover, the measured current of 10 pA at 100 mV at the top of nanosheets, measured by torsion resonance atomic force microscopy in dynamic non-contact mode, reveals high conducting nature of the film.<sup>50</sup> In addition, Wang *et al.*<sup>51</sup> has shown the presence of small energy bandgap in VGN of the order of meV.

Depending on the contact geometry, Wu *et al.*<sup>52</sup> have shown that the electron transport across metal/2D carbon interface is anisotropic in nature. They observed a very high mechanical magneto-resistance exceeding 10000% at room temperature and linear response within finite range of applied field due to magneto-mechanical effect, which make them a promising candidate for switch and magnetic sensor.<sup>53</sup>

### *Magnetic properties*

The magnetism of carbon nanostructure has become an interesting as well as a controversial research area. This is also true for VGN. The ferromagnetic property with large saturation magnetization of upto 2 emu/g at 5K and 1.2 emu/g at room temperature

demonstrates the capability of VGN as a promising candidate for graphene-based magnetic devices.<sup>54</sup> Ray *et al.*<sup>4</sup> have also shown room temperature ferromagnetism in partially hydrogenated VGN. Moreover, the observed magnetic phase transition at 50K is attributed to the co-existence of antiferromagnetism with ferromagnetic behavior.<sup>13</sup> In addition to that, Ney *et al.*<sup>55</sup> claim paramagnetic property instead of ferromagnetism in VGN and N<sub>2</sub> irradiated VGN even at 5K. On the other-hand, an anisotropic magnetic property of VGN on SiC substrate is also investigated by Chen *et al.*<sup>56</sup> They observed the diamagnetic property of VGN with susceptibility of  $-21.5 \times 10^{-6}$  emu/g at room temperature, while the magnetic field is perpendicular to the graphene basal plane and anisotropic susceptibility of  $-0.002/T$  emu/g at high temperature. The magnetic properties of VGN can be tuned by functionalization with Si and varying O<sub>2</sub>-content or by controlling the morphology.<sup>57,58</sup>

#### *Mechanical properties*

The mechanical strength and durability of CNT is further improved by growing VGN on CNT.<sup>59</sup> VGN based nano-composite exhibited higher Young's modulus and enhanced tensile strength than those of pure polymer.<sup>60</sup>

The VGN shows lubricating potential for the rubbed surfaces in the presence of low sulfur diesel fuels with friction co-efficient close to that of graphite.<sup>61</sup>

#### *Electrochemical and oxygen reduction properties*

The VGN exhibits fast electron transfer kinetics and excellent oxygen reduction reaction activity in alkaline medium. The electrochemical response exhibits reversible Nerstian behavior with a peak to peak separation of about 60 mV, which is close to that for single electron transfer of 59 mV. This can be further improved by N<sub>2</sub> plasma treatment of

VGN surface.<sup>53</sup>

Due to its outstanding properties, VGN hold the promise for a wide range of applications and are depicted as schematic in Fig. 1.6. The possible applications include electric double layer capacitor (EDLC),<sup>62</sup> Li-ion and vanadium redox flow battery,<sup>63,64</sup> ac line filtering,<sup>65</sup> corona discharge electrode,<sup>66</sup> THz modulators and photoelectric devices,<sup>67</sup>

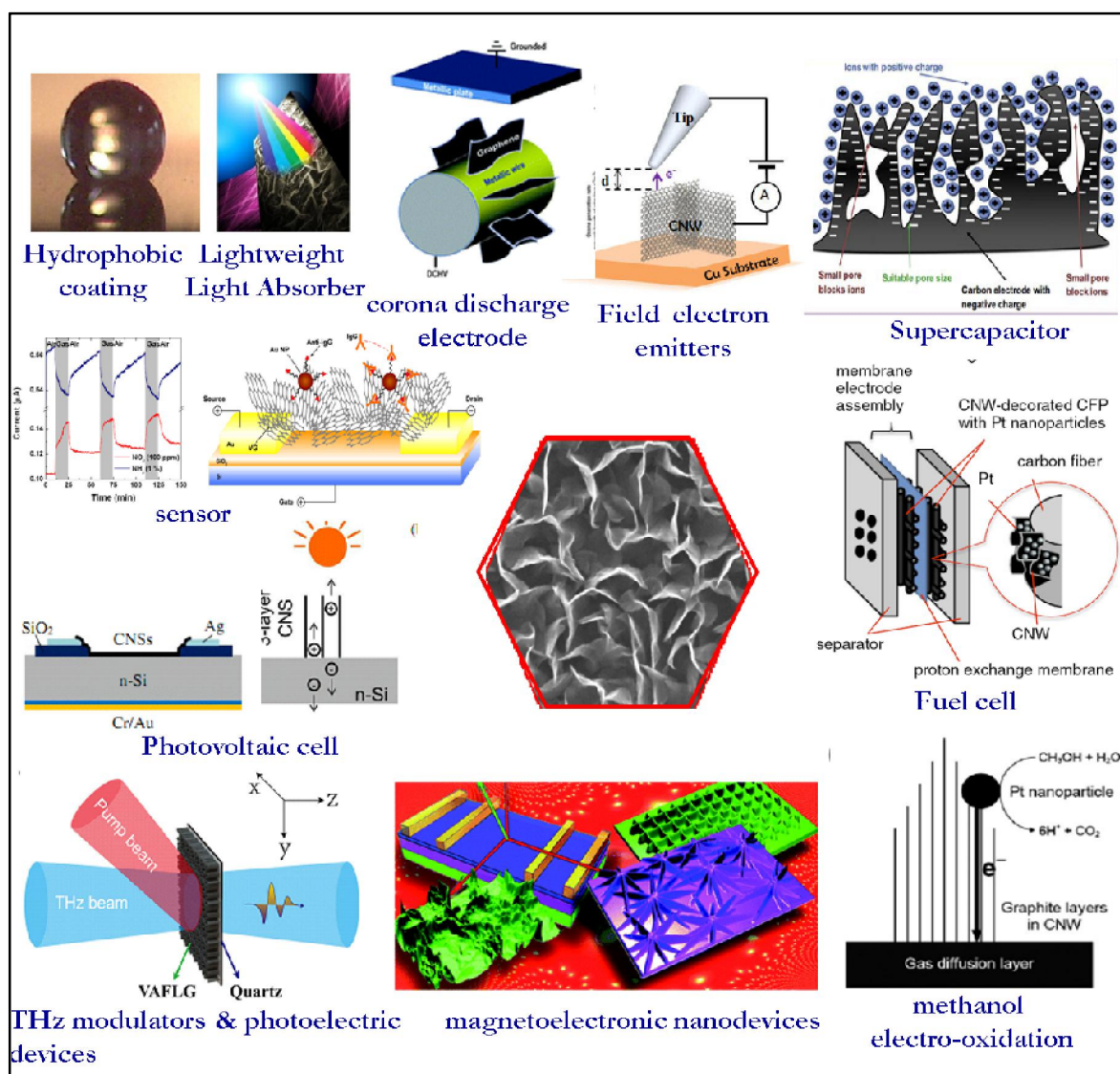


Figure 1.6: Schematic of various applications of vertical graphene nanosheets (images are taken from the corresponding references given in text)

fuel cell,<sup>68-70</sup> hydrogen absorption,<sup>71</sup> dye-sensitized solar cell, field electron emitters,<sup>41</sup> biosensor and gas sensor,<sup>72-75</sup> photovoltaic cell,<sup>16,76</sup> culturing of cervical cancer cells,<sup>77</sup> lightweight light absorber,<sup>78</sup> black body coating,<sup>36</sup> magnetoelectronic nanodevices,<sup>58</sup> hydrophobic, spintronics<sup>4</sup> and bio applications.<sup>79</sup>

### 1.3 Motivation and Research objectives

#### *Growth mechanism of vertical graphene nanosheets*

In view of above extraordinary properties and their potential applications, a better understanding of VGN growth is highly recommended. Among a variety of growth processes of VGN, plasma enhanced chemical vapor deposition (PECVD) has emerged as a key synthesis tool. In an excellent review, Bo *et al.*<sup>80</sup> presented the state-of-art on the growth of VGN and the understanding towards its growth mechanism. Despite several existing reports, herein it should be noted that a clear understanding of growth mechanism of VGN under complex plasma chemistry is still lacking. To provide plausible insights into the growth mechanism, this thesis intends to sort out some of the issues as follows:

- PECVD synthesized materials suffer from large amount of defects due to ion bombardment from the high density plasma. Hence, it is very important to gain knowledge over the defect formation mechanism with respect to the process parameters in order to minimize defects. Although almost all previous reports on defects in plasma based graphene synthesis deals through Raman spectrum analysis, a detailed investigation of defects and disorder, such as nature of defects, quantification of defect concentration and their correlation with growth mechanism, are scarce.
- The observed results in terms of morphology and structural properties of VGN grown by various groups are only in partial agreement and are sometimes even contradictory.

Briefly, while some groups have used Ar for the dilution of hydrocarbons,<sup>81-83</sup> others employed H<sub>2</sub> to grow VGN.<sup>84-87</sup> A few groups have also used a combination of Ar and H<sub>2</sub> for the growth of VGN.<sup>58,88</sup> The growth of monolayer graphene or few layer planar nanographitic films on metal surfaces using CH<sub>4</sub>/H<sub>2</sub> or CH<sub>4</sub>/Ar or CH<sub>4</sub>/Ar/H<sub>2</sub> as feedstock gases by microwave PECVD has also been successfully demonstrated by a few groups.<sup>89-94</sup> The reason for such variation and discrepancy among the published results could be due to the use of different synthesis techniques and conditions, which makes it difficult to give a single interpretation for the growth and its properties. The possible explanation for the vertical growth, irrespective of choice of gas composition, is the inherent local electric field due to plasma. At this point, it would be interesting to explore the possibility of growing graphitic structure (both vertical and planar) by single technique, namely PECVD, in presence of inherent local electric field.

Therefore, brief discussion on the defect-induced growth mechanism of VGN is addressed by growing VGN with varying the growth time, feedstock gas composition (Ar, H<sub>2</sub> and CH<sub>4</sub>) and growth temperature in the Chapter 3. Based on the experimental investigations, a phenomenological four stage growth model is proposed and a ternary field diagram is established to elucidate the growth mechanism through substrate-plasma interaction.

#### *Tuning vertical graphene nanosheets and study of its thermal stability*

Not only the understanding on the growth mechanism, but also a controlled, stable and optimized structure on desired substrate is highly essential towards commercialization of VGN. Although several attempts are directed towards getting controlled structure for

their applications, a clear understanding of the effect of PECVD process parameters and substrate on the final structure is very limited. Hence, a detailed study on the controllable morphology and structural property of VGN by changing the growth parameters, namely microwave power and distance from plasma source to substrate, is carried out and discussed in Chapter 4. In addition to that, the final optimized structures on proper substrates are required for their desired application. For example, sample on Cu substrate are needed for field emission application, samples on insulators are required for gas sensor, whereas samples are required on current collector (Ni, Ti, carbon paper) for their utilization in energy storage devices. The research on growth process of VGN is attempted on different types of substrates viz. Si, SiO<sub>2</sub>, Al<sub>2</sub>O<sub>3</sub>, MgO, quartz, Al, stainless steel, Pt, Ti, Cu, Ni, Mo, Zr, Hf, Nb, W, and Ta till date.<sup>37,86,95-97</sup> However, little attention has been paid to understand the role of substrates on the growth of VGN. Hiramatsu *et al.*<sup>96</sup> found that the growth rate of VGN on Ti to be 1.6 times more than that on Si, under identical growth conditions. Formation of interfacial carbide layer is reported to enhance the adhesion of VGN on quartz and Si substrates.<sup>95</sup> The substrate properties such as thermal conductivity,<sup>37,95</sup> electronic conductivity,<sup>98</sup> surface roughness, lattice parameter, ability to adsorb hydrocarbon species<sup>99</sup> and plasma-surface interaction<sup>100</sup> are found to influence the nucleation and growth. From the results of the studies carried out by various research groups, it can be inferred that substrate indeed plays a crucial role in growth of VGN. On the contrary, a few groups have reported that the nucleation and growth of VGN is substrate independent in PECVD.<sup>84,97</sup> Though the substrate surface effect on the VGN growth is reported, the study on substrate dependent growth mechanism is scarce. Hence, a detailed analysis on the role of substrate is essential to understand the nucleation, growth rate and morphology of VGN in PECVD technique. Apart from understanding the role of

substrate, the material is expected to be uniform throughout the deposition area and thermally stable to utilize them for commercial purpose. Hence, Chapter 4 describes how to achieve controlled structure over the various substrates with better crystallinity, uniformity and thermal stability.

#### *Electrochemical performance of vertical graphene nanosheets*

The emerging demand of next-generation devices, namely portable electronic devices, low emission hybrid vehicles, smart grids, memory backup systems, and military devices, necessitates development of efficient energy storage devices. The electrochemical capacitor or SC, have proven to be a promising candidate for next generation electronic energy storage device.<sup>101-103</sup> The SC can deliver very high power densities (>10 kW/kg) compared to batteries, possess higher energy density than that of the conventional capacitors and impressive cycle life (>10<sup>5</sup> cycles).<sup>104</sup> However, the energy density is significantly lower than that of batteries.<sup>101,102</sup> This drawback triggered considerable amount of research in improving the energy density without sacrificing the power density and cycle life by choosing advanced material with high specific capacitance and suitable electrolyte.<sup>105,106</sup> Carbon nanostructures, polymers and transition metal oxides are extensively used for this purpose.<sup>104-106</sup> The comparison of physicochemical properties of various SC materials is shown in Table 1.1.<sup>107</sup> The porous carbon nanomaterials, such as activated carbon, carbide derived carbons, mesoporous template carbon, CNT, graphene and their derivatives, are being extensively studied as promising materials because of their high surface area, good electrical conductivity, chemical stability, lower cost and biodegradability.<sup>108-110</sup> The comparison of those carbon nanostructures and their properties in EDLC electrode are given in Table 1.2.<sup>111</sup> The charge storage mechanism of porous carbon

based SC is formation of EDL at the electrode/electrolyte interface and not the faradic reactions.

Table 1.1: comparison of physicochemical properties of various SC materials <sup>107</sup>  
 ●●●● : very high, ●●●: high, ●● : medium, ● : low, ○ : very low

Physicochemical properties	Carbon materials	Metal Oxides	Conducting Polymers
Non Faradic capacitance	●●●●	●●	●●
Faradic capacitance	○	●●●●	●●●●
Conductivity	●●●●	●	●●●●
Energy density	●	●●●	●●
Power density	●●●	●	●●
Cost	●●	●●●	●●
Chemical stability	●●●●	●	●●●
Cycle life	●●●●	●●	●●
Easy fabrication process	●●	●	●●●
Flexibility	●●	○	●●●

Table 1.2: Comparison of different carbon materials and their properties in EDLC electrodes <sup>111</sup>

Material	Activ-ated carbon	Templ-ated carbon	Carbide derived carbon	Carbon Aerogel	Carbon Fiber	Graphene	CNT	GO
Price	Low	High	Medium	Medium	Medium	Medium	High	High
Scalability	High	Low	Medium	Medium	High	Medium	Low	Low
S(m <sup>2</sup> /g)	2000	4500	3200	700	200	2630	1315	500
$\sigma$	Low	Low	Medium	Low	Medium	High	High	variable
C <sub>g</sub>	Medium	High	High	Medium	Low	Medium	Low	Low
C <sub>v</sub>	High	Low	High	Low	Low	Medium	Low	Low

$\sigma$  - Conductivity, S- surface area, C<sub>g</sub> -Gravimetric capacitance, C<sub>v</sub>- Volumetric capacitance

The advantages of VGN over the issues of using existing carbon nanomaterials are as follows:

- powder electro-active materials require binders to fabricate the electrodes and on

additional current collector. Such materials strongly deteriorate electrochemical performance.

VGN can be grown on any substrate. VGN itself is conducting in nature obviating the need of an additional current collector.

- agglomeration and restacking of these carbon materials during processing always lower the specific surface area and create obstacle for the electrolyte ions to diffuse toward interior of the surface.<sup>112</sup> In consequence, a reduced efficiency for charge storage capacity is observed.<sup>113</sup>

VGN are vertically standing, non-agglomerated porous network having large fully accessible surface area.

- presence of large amount of edge planes on electrode surface enhances the capacitance value.<sup>65,114</sup> In view of this, Kim *et al*<sup>115</sup> have grown CNT on graphene and studied the electrochemical performance. In this system, graphene serve as the current collector and CNT with high surface area as EDL former. Capping of CNT, by the catalyst used during growth, renders tube inner surface and top edge unavailable for charge storage.

VGN is open network structure with high edge density.

- VGN can be easily functionalized, as it is discussed in previous section.

In view of proven capability and remarkable properties, the VGN can be materials of choice for energy storage device. This unique structure offers the migration of electrolyte ions into the interior surface for the formation of extensive EDL which improves charge storage capacity.<sup>116</sup> Therefore, the last few years have witnessed a strong momentum towards the electrochemical characterization of VGN for application in SC.<sup>8,62,65,114,117-122</sup> The overall SC performance not only depends on the electrode material but also on the electrolyte used.<sup>123-125</sup> The use of aqueous electrolyte for SC application is

more suitable than the organic electrolytes in terms of cost, life time, low internal resistance, non-flammability and toxicity. The different VGN/aqueous electrolyte systems studied are listed in Table 1.3. The different value of capacitance could be due to the different electrolytes and their interaction with the electrode. Since, compatibility of ion-size with pore-size, charge transfer resistance and ionic mobility of electrolytes are major driving parameters for better performance. Hence, a good understanding of electrode/electrolyte interaction is essential for proper selection of electrolyte to utilize VGN with full accessibility.

Table 1.3: comparison on capacitance values of VGNs under different aqueous electrolytes reported in the literatures.

Ref.	height	substrate	Aqueous electrolyte	Sp. capacitance
<sup>65</sup>	0.6 $\mu\text{m}$	Ni	25 wt % KOH	175 $\mu\text{F}/\text{cm}^2$ at 120 Hz
<sup>8</sup>	0.1 $\mu\text{m}$	Pt/Si	6M KOH	704 $\mu\text{F}/\text{cm}^2$ at 2 mV/s
<sup>62</sup>	-	carbon paper	6M $\text{H}_2\text{SO}_4$	76 $\text{mF}/\text{cm}^2$
<sup>119</sup>	0.5 $\mu\text{m}$	Carbon cloth	1M $\text{H}_2\text{SO}_4$	0.7 $\text{F}/\text{cm}^2$ at 2 mV/s
<sup>121</sup>	-	Ni foam	1M $\text{Na}_2\text{SO}_4$	0.46 $\text{F}/\text{cm}^2$ at 5 mV/s
<sup>122</sup>	-	Glassy carbon	1M $\text{Na}_2\text{SO}_4$	0.8-1 $\text{mF}/\text{cm}^2$

Therefore the electrochemical performance of VGN as SC electrode are carried in the three parts, as follows, and details of this study are covered in Chapter 5

- Morphology dependent performance of VGN in 1M  $\text{H}_2\text{SO}_4$  to select VGN with optimized structure
- Influence of aqueous electrolyte on the electrochemical performance of VGN to find out suitable electrolyte
- $\text{MnO}_2$  decoration on VGN to increase the electrochemical performance

---

## 1.5 References

1. Dreyer, D. R., *et al.*, *Angew. Chem. Int. Ed.* (2010) **49** (49), 9336
2. Wick, P., *et al.*, *Angew. Chem. Int. Ed.* (2014) **53** (30), 7714
3. Bianco, A., *et al.*, *Carbon* (2013) **65**, 1
4. Ray, S. C., *et al.*, *Sci. Rep.* (2014) **4**, 3862
5. Jacob, M. V., *et al.*, *Nano Lett.* (2015) **15** (9), 5702
6. Watanabe, H., *et al.*, *Jpn. J. Appl. Phys.* (2012) **51** (1S), 01AJ07
7. Dong, J., *et al.*, *Sci. Rep.* (2013) **3**, 1733
8. Qi, J. L., *et al.*, *Nanoscale* (2015) **7** (8), 3675
9. Vizireanu, S., *et al.*, *Plasma Process. Polym.* (2012) **9** (4), 363
10. Liao, Q., *et al.*, *ACS nano* (2015) **9** ( 5), 5310
11. Dang, C., *et al.*, *Mater. Sci. Semicond. Process.* (2014) **27**, 97
12. Shen, B., *et al.*, *Appl. Surf. Sci.* (2012) **258** (10), 4523
13. Wang, Z., *et al.*, *Carbon* (2014) **68**, 360
14. Wu, J., *et al.*, *Nucl. Instrum. Methods Phys. Res., Sect. B* (2013) **304**, 49
15. Wang, S., *et al.*, *Appl. Phys. Lett.* (2006) **89** (18), 183103
16. Jiao, T., *et al.*, *RSC Adv.* (2016) **6**, 10175
17. Evlashin, S., *et al.*, *Carbon* (2014) **70**, 111
18. Vizireanu, S., *et al.*, *Physica E: Low dimens. Syst. Nanostruct.* (2013) **47**, 59
19. Hiramatsu, M., *et al.*, *InTech Europe, Croatia* (2013), 235
20. Krivchenko, V. A., *et al.*, *Carbon* (2012) **50** (3), 1438
21. Thomas, R., and Rao, G. M., *J. Mater. Chem. A* (2015) **3** (1), 274
22. Moitzheim, S., *et al.*, *Nanotechnology* (2014) **25** (50), 504008
23. Jin, S., *et al.*, *Nano Energy* (2013) **2** (6), 1128

24. Chang, H.-C., *et al.*, *Appl. Surf. Sci.* (2012) **258** (22), 8599
25. Wang, X., *et al.*, *New J. Chem.* (2012) **36** (9), 1902
26. Sviridova, L. N., *et al.*, *Mendeleev Commun.* (2014) **24** (5), 304
27. Zhang, C., *et al.*, *Carbon* (2012) **50** (10), 3731
28. Vansweevelt, R., *et al.*, *Chem. Phys. Lett.* (2010) **485** (1), 196
29. Cui, S., *et al.*, *J. Phys. D: Appl. Phys.* (2015) **48** (31), 314008
30. Wang, H., *et al.*, *Carbon* (2008) **46** (8), 1126
31. Suetin, N., *et al.*, *Phys. Chem. Chem. Phys.* (2016) **18**, 12344
32. Rider, A. E., *et al.*, *Chem. Commun.* (2012) **48** (21), 2659
33. Wu, Y., *et al.*, *Adv. Funct. Mater.* (2002) **12** (8), 489
34. Deng, J.-h., *et al.*, *Carbon* (2012) **50** (12), 4732
35. Mao, S., *et al.*, *Small* (2015) **11** (4), 414
36. Krivchenko, V., *et al.*, *Sci. Rep.* (2013) **3**, 3328
37. Kim, S. Y., *et al.*, *Jpn. J. Appl. Phys.* (2014) **53** (5S1), 05FD09
38. Kawai, S., *et al.*, *Jpn. J. Appl. Phys.* (2010) **49** (6R), 060220
39. Wang, B., *et al.*, *J. Mater. Chem. C* (2014) **2** (16), 2851
40. Chiou, J., *et al.*, *J. Phys. Chem. C* (2012) **116** (30), 16251
41. Wu, Y., *et al.*, *J. Mater. Chem.* (2004) **14** (4), 469
42. Qi, J., *et al.*, *J. Phys. D: Appl. Phys.* (2010) **43** (5), 055302
43. Takeuchi, W., *et al.*, *Appl. Phys. Lett.* (2011) **98** (12), 123107
44. Itoh, T., *et al.*, *J. Non-Cryst. Solids* (2012) **358** (17), 2548
45. Hiramatsu, M., and Hori, M., *Carbon nanowalls: synthesis and emerging applications*. Springer: 2010
46. Cho, H. J., *et al.*, *Carbon* (2014) **68**, 380

47. Takeuchi, W., *et al.*, *Appl. Phys. Lett.* (2008) **92** (21), 213103
48. Cho, H. J., *et al.*, *Jpn. J. Appl. Phys.* (2014) **53** (4), 040307
49. HanáSeo, D., *J. Mater. Chem.* (2011) **21** (41), 16339
50. Vetushka, A., *et al.*, *J. Non-Cryst. Solids* (2012) **358** (17), 2545
51. Wang, H., *et al.*, *Solid State Commun.* (2008) **145** (7), 341
52. Wu, Y., *et al.*, *AIP Adv.* (2012) **2** (1), 012132
53. Zhang, C., *et al.*, *Appl. Phys. Lett.* (2010) **97** (6), 062102
54. Yue, Z., *et al.*, *Appl. Phys. Lett.* (2014) **104** (9), 092417
55. Ney, A., *et al.*, *Appl. Phys. Lett.* (2011) **99** (10), 102504
56. Chen, L., *et al.*, *RSC Adv.* (2013) **3** (33), 13926
57. Ray, S. C., *et al.*, *J. Appl. Phys.* (2015) **118** (11), 115302
58. Yue, Z., *et al.*, *Nanoscale* (2013) **5** (19), 9283
59. Kumar, A., *et al.*, *Carbon* (2015) **84**, 236
60. Davami, K., *et al.*, *J. Mater. Res.* (2015), 1
61. Vizireanu, S., *et al.*, *Dig. J. Nanomater. Biostruct.* (2013) **8** (3), 1145
62. Zhao, X., *et al.*, *J. Power Sources* (2009) **194** (2), 1208
63. Xiao, X., *et al.*, *Electrochem. Commun.* (2011) **13** (2), 209
64. González, Z., *et al.*, *Nano Energy* (2012) **1** (6), 833
65. Miller, J. R., *et al.*, *Science* (2010) **329** (5999), 1637
66. Bo, Z., *et al.*, *Energy Environ. Sci.* (2011) **4** (7), 2525
67. Fu, M., *et al.*, *Appl. Phys. Lett.* (2016) **108** (12), 121904
68. Hiramatsu, M., *et al.*, *Jpn. J. Appl. Phys.* (2013) **52** (1S), 01AK03
69. Shang, N., *et al.*, *J. Phys. Chem. C* (2010) **114** (37), 15837
70. Shin, S. C., *et al.*, *J. Appl. Phys.* (2011) **110** (10), 104308

71. Kita, Y., *et al.*, *J. Appl. Phys.* (2010) **108** (1), 013703
72. Mao, S., *et al.*, *Sci. Rep.* (2013) **3**, 1696
73. Seo, D., *et al.*, *Carbon* (2013) **60**, 221
74. Shang, N. G., *et al.*, *Adv. Funct. Mater.* (2008) **18** (21), 3506
75. Wang, Z., *et al.*, *Talanta* (2012) **99**, 487
76. Wang, Z., *et al.*, *Carbon* (2014) **67**, 326
77. Watanabe, H., *et al.*, *Appl. Phys. Lett.* (2014) **105** (24), 244105
78. Davami, K., *et al.*, *Mater. Res. Bull.* (2016) **74**, 226
79. Stancu, E. C., *et al.*, *J. Phys. D: Appl. Phys.* (2014) **47** (26), 265203
80. Bo, Z., *et al.*, *Nanoscale* (2013) **5** (12), 5180
81. Cheng, C., and Teii, K., *IEEE Trans. Plasma Sci.* (2012) **40** (7), 1783
82. Wang, Z., *et al.*, *Appl. Surf. Sci.* (2011) **257** (21), 9082
83. Jain, H. G., *et al.*, *Carbon* (2011) **49** (15), 4987
84. Hiramatsu, M., *et al.*, *Appl. Phys. Lett.* (2004) **84** (23), 4708
85. Vizireanu, S., *et al.*, *Surf. Coat. Technol.* (2012) **211**, 2
86. Wu, Y., *et al.*, *Adv. Mater.* (2002) **14** (1), 64
87. French, B., *et al.*, *Thin Solid Films* (2006) **494** (1), 105
88. Yoshimura, A., *et al.*, *Carbon* (2012) **50** (8), 2698
89. Schmidt, M. E., *et al.*, *Mater. Res. Express* (2014) **1** (2), 025031
90. Kim, Y., *et al.*, *Appl. Phys. Lett.* (2011) **98** (26), 263106
91. Chan, S.-H., *et al.*, *Nanoscale Res. Lett.* (2013) **8** (1), 1
92. Woehrl, N., *et al.*, *AIP Adv.* (2014) **4** (4), 7128
93. SeungáKim, Y., and DanieláPark, Y., *Nanoscale* (2013) **5** (3), 1221
94. Van Nang, L., and Kim, E.-T., *J. Electrochem. Soc.* (2012) **159** (4), K93

95. Vitchev, R., *et al.*, *Nanotechnology* (2010) **21** (9), 095602
96. Hiramatsu, M., *et al.*, *Jpn. J. Appl. Phys.* (2013) **52** (1S), 01AK05
97. Wang, J., *et al.*, *Carbon* (2004) **42** (14), 2867
98. Wang, Z., *et al.*, *Jpn. J. Appl. Phys.* (2012) **51** (1S), 01AH02
99. Zhang, L., *et al.*, *Nano Research* (2011) **4** (3), 315
100. Ostrikov, K., *et al.*, *Adv. Phys.* (2013) **62** (2), 113
101. Conway, B. E., *Electrochemical supercapacitors : Scientific Fundamentals and Technological Applications*. Kluwer Academic/Plenum Publishers(1999)
102. Winter, M., and Brodd, R. J., *Chem. Rev.* (2004) **104** (10), 4245
103. Dubal, D., *et al.*, *Chem. Soc. Rev.* (2015) **44** (7), 1777
104. Miller, J. R., and Burke, A. F., *Electrochem. Soc. Interface* (2008) **17** (1), 53
105. Simon, P., and Gogotsi, Y., *Nature materials* (2008) **7** (11), 845
106. Yan, J., *et al.*, *Adv. Energy Mater.* (2014) **4** (4)
107. Shown, I., *et al.*, *Energy Science & Engineering* (2015) **3** (1), 2
108. Portet, C., *et al.*, *Carbon* (2007) **45** (13), 2511
109. Ghosh, A., and Lee, Y. H., *ChemSusChem* (2012) **5** (3), 480
110. Béguin, F., *et al.*, *Adv. Mater.* (2014) **26** (14), 2219
111. Borchardt, L., *et al.*, *Materials Horizons* (2014) **1** (2), 157
112. Inagaki, M., *New Carbon Mater.* (2009) **24** (3), 193
113. Si, Y., and Samulski, E. T., *Chem. Mater.* (2008) **20** (21), 6792
114. Aradilla, D., *et al.*, *J. Mater. Chem. A* (2015) **3** (38), 19254
115. Kim, Y.-S., *et al.*, *Nanotechnology* (2012) **23** (1), 015301
116. Kötz, R., and Carlen, M., *Electrochim. Acta* (2000) **45** (15), 2483
117. Dinh, T. M., *et al.*, *Nano Energy* (2014) **10**, 288

118. Sheridan, L. B., *et al.*, *J. Electrochem. Soc.* (2014) **161** (9), H558
119. Xiong, G., *et al.*, *Adv. Energy Mater.* (2014) **4** (3), 1300515
120. Chen, J., *et al.*, *Vertically-Oriented Graphene*. Springer: 2015
121. Seo, D. H., *et al.*, *ACS Sustain. Chem. Eng.* (2015) **3** (3), 544
122. Komarova, N. y. S., *et al.*, *Langmuir* (2015) **31** (25), 7129
123. Lota, G., *et al.*, *Energy Environ. Sci.* (2011) **4** (5), 1592
124. Winchester, A., *et al.*, *ACS Appl. Mater. Interfaces* (2014) **6** (3), 2125
125. Kim, M., *et al.*, *Phys. Chem. Chem. Phys.* (2015) **17**, 16367

# 2

## Experimental Techniques

*At the beginning of all experimental work stands the choice of the appropriate technique of investigation*

*Walter Rudolf Hess*

Synthesis, characterization and utilization of materials for suitable application involve studies and investigations by several complementary experimental techniques. This chapter presents an overview on deposition techniques used for the substrate preparation and growth of vertical graphene nanosheets and the characterization techniques used to understand morphological, elemental, structural, wettability and electrical properties of the grown samples. To utilize the material for energy storage as a supercapacitor electrode, the electrochemical set up is used and discussed in details.

## 2.1 Introduction

The experimental methods including thin film deposition for substrate preparation and synthesis of vertical graphene nanosheets (VGN) are briefly described. The SiO<sub>2</sub> thin film preparation and Au coating on Si substrates for growth of VGNs are carried out in muffle furnace and DC-sputtering unit, respectively. The VGN are grown by Electron-cyclotron resonance chemical vapor deposition technique.

The different type of characterization techniques utilized for understanding the morphological, elemental, structural, optical and electrical properties, are discussed. Scanning and transmission electron microscopy are employed for morphological and structural studies of the VGN.<sup>1</sup> The elemental analysis is performed by X-ray photoelectron spectroscopy and electron energy loss spectroscopy.<sup>1</sup> The structural quality in terms of degree of graphitization of the VGN is studied exclusively by Raman spectroscopy.<sup>1</sup> The roughness, morphology and thickness of the film are measured by atomic force microscopy.<sup>1</sup> Moreover, wettability property of the film is studied by contact angle measurement. The electrical properties of the films are carried out by the four probe resistive method in the van-der Pauw geometry.

The electrochemical investigation of VGN as a supercapacitor electrode is carried out by cyclic voltammetry, charge-discharge and electrochemical impedance spectroscopy.

## 2.2 Growth techniques

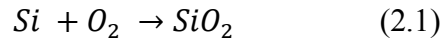
### 2.2.1. Muffle furnace

The potential use of the material for next generation electronic device, the requirement is to grow the film on the insulating substrate. For this purpose, cheap and easily available n-type Si substrate (P-doped) with resistivity of 2-8 Ω-cm are used for the

SiO<sub>2</sub> growth. Figure 2.1(a) shows the schematic of muffle furnace used for the thermal oxidation of Si.

The muffle furnace is made of resistive heating elements and ceramic fiber wool insulation for better temperature uniformity and stability. The temperature is controlled by a thyristor based power control coupled to a PID controller. The K-type thermocouple is used for temperature measurement.

The growth of SiO<sub>2</sub> on Si is based on dry oxidation method, where oxygen supplied from the ambient. In this process, an oxidizing agent diffuses into the wafer at high temperature and reacts with it. The chemical reaction occurs at the Si surface is



It should be noted that whenever Si is exposed to air or water, it automatically forms a native oxide of 2 nm thickness. The growth rate of oxidation decreases with the increasing thickness of oxide layer, because to grow more oxide layer, oxygen has to diffuse through more and more oxide layer.<sup>2</sup>

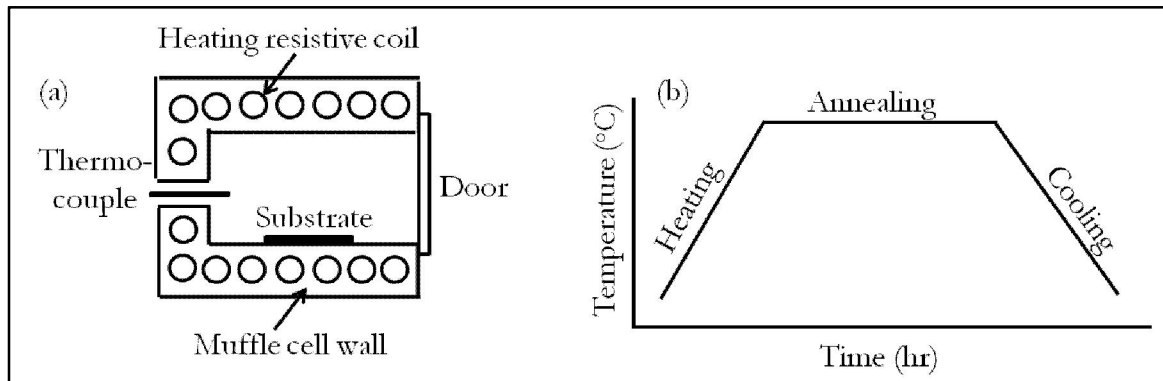


Figure 2.1: (a) Schematic of muffle furnace, and (b) typical temperature profile maintained for the growth of SiO<sub>2</sub> on Si substrate

For typical SiO<sub>2</sub> growth, Si substrate is heated to 1000°C, kept for 6hrs and cooled down naturally to room temperature by switching off the furnace [Fig. 2.1(b)]. The

thickness of SiO<sub>2</sub> is verified by cross sectional SEM images and also from color-vs-thickness chart. The thickness is found to be around 450 nm.

### 2.2.2. DC sputtering unit

A thin film of Au on n-Si(100) substrate is grown by DC sputter deposition to investigate the role of substrate on the growth of VGN (will be discuss in Chapter-4).

The sputter deposition is one of the physical vapor deposition techniques used for thin film growth. A schematic of the sputtering process is given in Fig. 2.2(a). In DC sputtering system, the vacuum chamber is evacuated and argon is let in at a pressure of  $8 \times 10^{-3}$  mBar. A potential is applied between the cathode and the anode to accelerate electrons between the electrodes. The collision between these electrons and Ar atoms results in Ar<sup>+</sup> ions and more electrons which is creating the glow discharge. The electrons are attracted by the anode whereas the Ar<sup>+</sup> ions are accelerated towards cathode. The energetic Ar<sup>+</sup> ions on impinging produces secondary electrons and sputter atoms from the surface of the cathode (target). These secondary electrons maintain the glow. The sputtered atoms finally condense on the substrate. A sketch of the DC sputtering system is shown in Fig. 2.2(b).

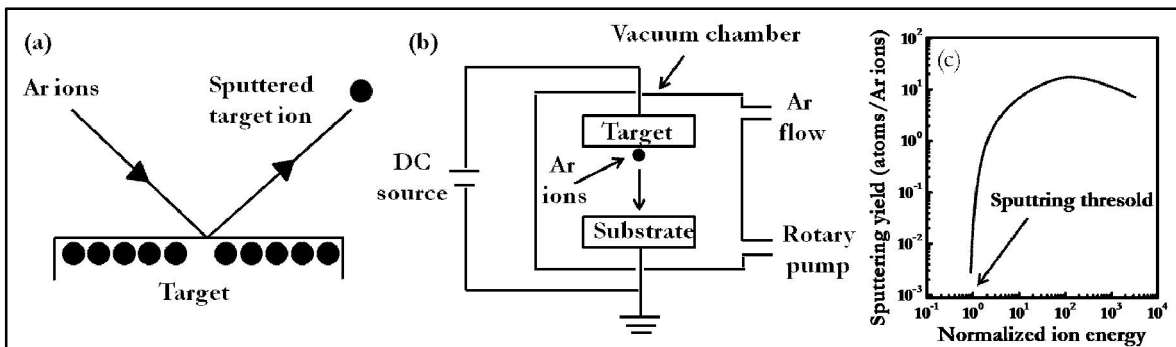


Figure 2.2: (a) Schematic of sputtering process, (b) DC-sputtering for thin film deposition and (c) plot of sputtering yield vs normalized ion energy

The growth rate of the film by the above mentioned technique depends on the distance between cathode and anode, DC voltage, chamber pressure and nature of target. For sputtering, it should exceed the threshold energy. The sputtering yield is the number of liberated atoms from the target by each incident atom and it increases with energy of incident ions. Figure 2.2(c) shows the typical plot of sputtering yield with respect to the normalized ion energy.<sup>2</sup>

### 2.2.3. Electron Cyclotron Resonance - Chemical Vapor Deposition

The VGN, materials for the present work, are synthesized by Electron Cyclotron Resonance Microwave Plasma Enhanced Chemical Vapor Deposition (ECR-MWPECVD).

Chemical vapor deposition (CVD) is a deposition technique where thin films form on the surface of a substrate by decomposition or reaction of gaseous compounds in gas phase. In thermal CVD system (TCVD), gaseous species decomposed by thermal heating, while it decomposed by plasmas in PECVD. The major advantages of PECVD over TCVD are

- PECVD allows deposition at lower substrate temperature with higher growth rate
- capability of high quality, controllable and uniform growth on both catalytic and non-catalytic substrates
- possibility to grow patterned vertical nanostructures
- amenable to doping by heteroatoms

In view of proven capability, PECVD has become the most popular technique for the growth of wide range of carbon nanostructure.<sup>3</sup> The plasma in PECVD can be generated by arc discharge, microwave (MW) or radio-frequency (RF) system. Typical parameters of arc-discharge, MW and RF plasma reactors used for nanofabrication are

listed in Table 2.1. The chronology of carbon structures grown by PECVD is depicted in Fig. 2.3.

Table 2.1: Typical parameters of arc-discharge, Radio-Frequency and Microwave plasmas used for the nanofabrication<sup>4</sup>

Parameters	arc-discharge	RF-plasma	MW-Plasma
Discharge power range (kW)	0.1-10	0.01-10	0.1-10
Plasma density (cm <sup>-3</sup> )	10 <sup>11</sup> -10 <sup>14</sup>	10 <sup>10</sup> -10 <sup>13</sup>	10 <sup>10</sup> -10 <sup>13</sup>
Electron energy in discharge (eV)	0.5-10	1-5	5-10
Operating pressure range (mBar)	-	0.01-10	0.001-100
Typical frequency	-	0.46-13.56 MHz	2.45 GHz
Power density (W × cm <sup>-3</sup> )	-	0.01-0.5	1-2
Substrate temperature range	3000-3500K	100-500 °C	100-800 °C
	(anode surface)		
Discharge electrode	Required	Required	Not required

<b><u>Carbon nanostructures grown by PECVD</u></b>	
1976:	First report on carbonaceous films
1985:	Polycrystalline diamond films
1989:	nanocrystalline diamond film (ND)
1991:	Carbon Nanotube (CNT)
1994:	Diamond films from Ar- C <sub>60</sub> plasmas
1994:	Ultracrystalline diamond (UNCD)
1997:	Petal like graphite sheets or Vertical Graphene Nanosheets (VGN)
2000:	Carbon Nanofiber (CNF)
2001:	Nitrogen doped UNCD
2001:	Carbon nanocone
2004:	Hybrid of CNF and CNT
2005:	Aligned Carbon Nanotips
2005:	Hybrid of UNCD and CNT
2005:	Carbon Nanohorns
2005:	CNF/VGN
2007:	Hybrid of VGN and CNT
2008:	Single and bi-layer graphene
2008:	ND/VGN
2016:	Graphene Oxide

Figure 2.3: A chronology of carbon nanostructure prepared by PECVD technique

### Principle of ECR-plasma

In ECR plasma source, strong magnets are used to produce magnetic field ( $\mathbf{B}$ ). Free electrons always presence in chamber. When an external changing electric field ( $\mathbf{E}$ ) is generated by the microwaves, free electrons experience the force in presence of magnetic field and start to move in helical path due to Lorentz force:  $\mathbf{F} = e[\mathbf{E} + (\mathbf{v} \times \mathbf{B})]$  (Figure 2.4(b)) If their gyration frequency,  $\omega_{ec}(=\frac{eB}{m_e})$  equals with the applied microwave of frequency ( $\omega_{MW}$ ), a resonance occurs which heat up the massive number of electrons. Where  $e$  is the electronic charge,  $m_e$  is mass of electron,  $\mathbf{E}$  is the strength of electric field and  $\mathbf{B}$  is the strength of magnetic field. These hot electrons collide with the atoms or ions and produce highly charged ions in a sequence of avalanche ionization steps.

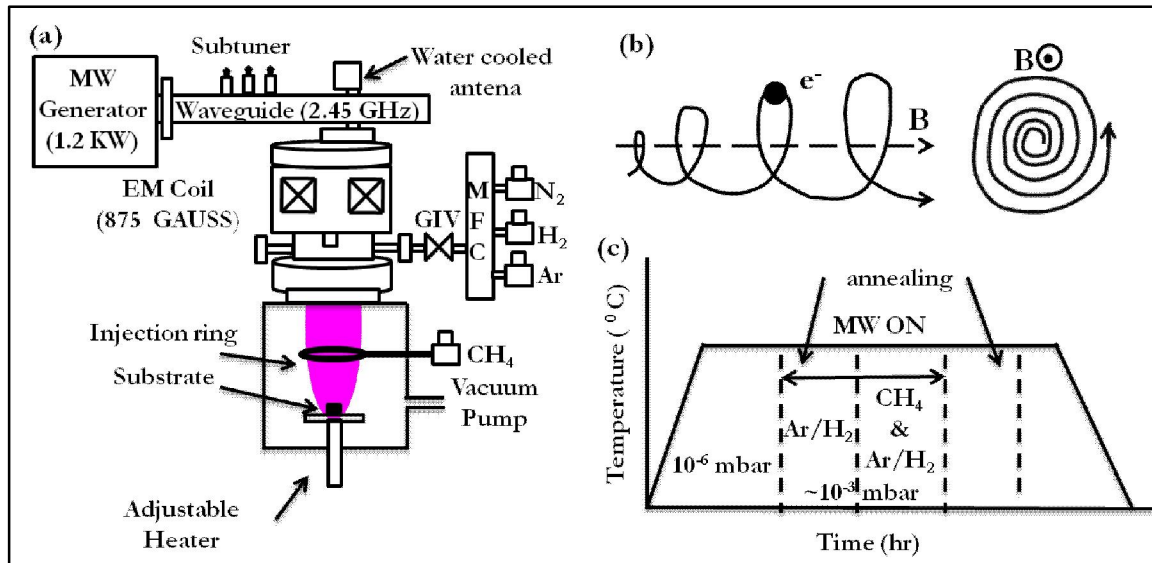


Figure 2.4: (a) A schematic of ECR-CVD for VGN growth, (b) path of electron in presence of magnetic and electric field and (c) typical growth profile of VGN

### Instrument details

Figure 2.4(a) depicts a schematic of ECR-CVD used for this work. The important components of ECR-CVD are as follows:<sup>5</sup>

- Vacuum pumping system:

Rotary pump: 350 lit/min

Turbo molecular pump: 1100 lit/s

Vacuum gauge: Pirani gauge ( $0.5 - 10^{-3}$  mbar) and Penning gauge ( $10^{-3} - 10^{-6}$  mbar)

- Vacuum chamber:

*Dimension:* diameter of 54 cm and height of 64 cm

*Heating element:* Resistive coil, maximum temperature 900°C, coupled with programmable PID temperature controller

*adjustable substrate holder* to adjust distance from plasma source to substrate

*Gas inlet valve and downstream injection ring* through which feedstock gases are fed into the chamber and flow rates are controlled by mass flow controller (MFC)

- Plasma Source:

*Microwave generator or magnetron:* 2.45 GHz with MW power upto 1.5 kW. MW launches as TE<sub>10</sub> waves and pass through three-port circulator. The circulator and water cooled dummy load are connected with magnetron to protect from reflected power. The impedance matching of MW transmission line with ECR plasma and minimizing of reflected power are carried out by three sub-tuners and sliding slot, respectively. The TE<sub>01</sub> rectangular mode is converted to TM<sub>01</sub> circular mode by a MW mode converter and then MW enters to vacuum chamber through MW introduction window.

*Microwave introduction window:* a quartz cup serve as a vacuum window and has required dimension for impedance matching of MW transmission line with ECR plasma and plasma shield. The quartz cup also serves as a separator between plasma

generator chamber and reaction chamber. A periodic cleaning of quartz cup is carried out to preserve the MW transmission.

*Electromagnet:* ECR condition is satisfied by a magnetic field of 875 Gauss for radial and axial confinement of plasma, generated from a water-cooled electromagnet coil. The top and bottom coil current are set to 130 A and 170 A, respectively.

### ***Kinetics of growth process***

The typical growth process of VGN by ECR-CVD in this thesis is depicted by temperature vs time curve in Fig. 2.4(b). The details of growth parameters for the particular growth are given in corresponding Chapters. The transport mechanisms and kinetics of the growth process are as follows:<sup>6</sup>

- (i). transport and diffusion of reactant gas species by forced convection from the upper zone, which is surrounded by ECR-magnet,
- (ii). activation of carrier gas plasma by MW power,
- (iii). insertion of hydrocarbon gas through the upper zone or downstream injection ring and collision of carrier gas activated species with hydrocarbon to produce plasma species by activation and dissociation,
- (iv). transportation of generated plasma species towards the surface of the substrate,
- (v). adsorption of plasma species through thermal-mediated surface processes: surface migration, nucleation and film growth,
- (vi). byproducts desorption from the surface,
- (vii). transport of byproducts by diffusion through boundary layer and back to main gas stream and by forced convection away from the deposition region.

## 2.3 Morphological characterization

### 2.3.1. Field Emission Scanning Electron Microscope (FESEM)

The field emission scanning electron microscope (FESEM) is one of the most popular imaging techniques to analyze the surface morphology, friction tracks etc of nanomaterials and nanostructures.

In principle, a electron beam is generated by applying voltage to the electron emitting filament. When beam of electrons interacted with specimen with very fine spot size of  $\sim 5$  nm and having energy ranging from a few hundred eV to 30 KeV, it undergoes either elastic or inelastic scattering. The emitted electrons after scattering with energy of  $< 30$  eV is called as secondary electron (SE). The elastically scattered electrons with angle  $> 90^\circ$  are referred as back scattered electrons (BSE). SE and BSE are carrying information of z-contrast and topography and the information is detected in corresponding detectors.

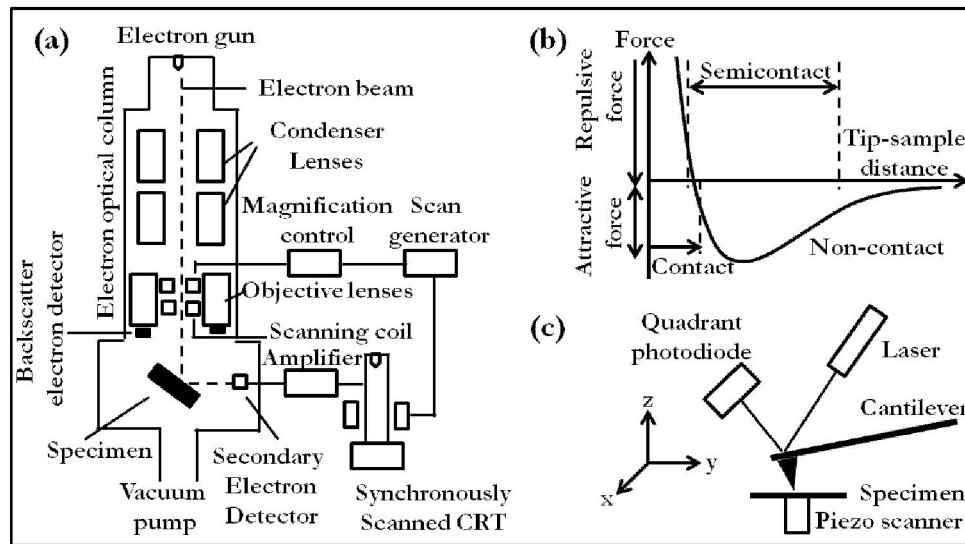


Figure 2.5: (a) schematic diagram of FESEM, (b) interaction force vs distance between tip and sample, and (c) schematic diagram of AFM.

A SEM consists of an electron gun (made of tungsten or  $\text{LaB}_6$ ), a lens system, scanning coil, electron collector and cathode ray display tube, as depicted in Fig. 2.5 (a).

The resolution of SEM is few nm, where magnification can be varied from 10 to 400k $\times$ . Morphological analysis (top view and cross sectional view) of VGN, in present thesis, is carried out using a FESEM (SUPRA 55, Zeiss) at electron accelerating voltage of 3kV. The working distance is kept around 2.5 mm and 25-300 k $\times$  magnification is used.

### **2.3.2. Atomic Force Microscopy (AFM)**

Atomic force microscopy is a 3D imaging technique based on the principle of force-distance relationship [Fig. 2.5(b)]. Main advantage of AFM can be used on both conductive and non-conductive surface and in air, vacuum or liquid medium. Its resolution is 0.01 nm and uses a micro-machined cantilever with a tip of 500  $\text{Å}$  at the end to sense the force from the surface. It is basically consists of a cantilever with probe tip, coarse tip positioning system, feedback system and piezoelectric sample scanner [Fig. 2.5(c)].

The deflection of cantilever beam depends on the nature of force and that information is collected from the position of a reflected laser spot falling on quadrant photodiode. AFM is operated in contact mode, non-contact mode and tapping mode depending on the nature of force.

The AFM (NT-MDT, NTEGRA) is used in this thesis to measure the height of nanographitic film and substrate roughness.

## **2.4 Structural characterization**

### **2.4.1. Transmission Electron Microscopy (TEM)**

The transmission electron microscopy (TEM) is another advanced technique to provide the morphological, compositional and crystallographic information.

When an electron beam, accelerated from electron gun with high voltage of the

range of 100-400 kV towards a thin specimen, it will be (1) scattered from specimen, (2) transmitted through specimen and (3) absorbed by the specimen. The specimen should be thin enough for the electrons to pass through and nanostructured materials are usually loaded on Cu grid for TEM analysis.

- **Electron diffraction:** The forward scattered and transmitted electrons form diffraction pattern in the back focal plane. The electron diffraction pattern obtained from the atoms plane space, which satisfy Bragg's law of equation

$$d = n\lambda/2\sin\theta \quad (2.2)$$

It provides information about crystalline phase, crystalline size, nature of defects, etc

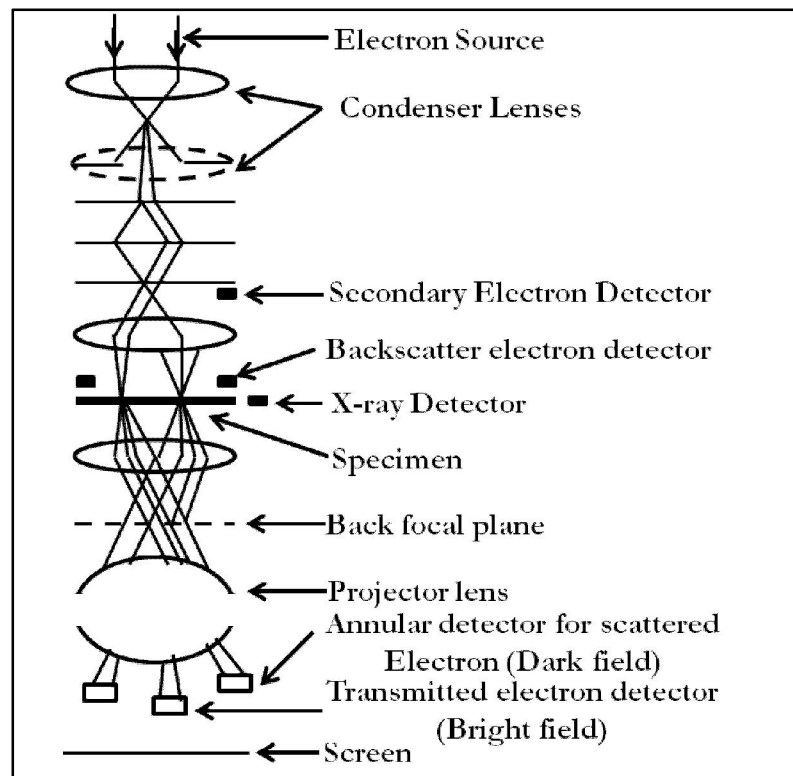


Figure 2.6: A schematic of transmission electron microscopy (TEM)

- **Dark Field imaging:** Image formed with specified diffracted beam are dark field image. It is useful for phase differentiation.

- **Bright field imaging:** Unscattered transmitted electron is used to form the bright field image. It gives the contrast based on thickness and density variation.
- **High resolution imaging:** It is a combination of diffraction and bright field imaging. It provides lattice parameters, grain orientation and information of individual defects.

From TEM analysis, one can obtain bright field and dark field images, selected area electron Diffraction (SAED) patterns, high resolution images (HRTEM) and fast Fourier transform (FFT) images. A schematic diagram is given in Fig. 2.6 and the major components of TEM are listed below with

- **Illumination system:** Electron gun, condenser lenses, condenser apertures
- **Objective lens/stage:** objective lenses, sample stage/holder
- **Imaging system:** Intermediate and projector lenses, fluorescent viewing screen or computer display via a detector, CCD, or TV camera.

#### 2.4.2. Electron Energy Loss Spectroscopy (EELS)

The EELS analysis is based on energy distribution of transmitted electron through the specimen. It is a very sensitive technique for low Z-elements ( $Z \leq 10$ ). The EELS spectra consists of<sup>1</sup>

**zero loss peak:** formed by unscattered and elastically scattered electron. Provide the information of spectrometer resolution

**low energy loss peak:** due to the plasmons, ranges from 0-40 eV. It forms by stimulated electronic transitions within valence band and stimulated collective oscillation of electron sea of solid

**high energy loss peak :** due to the inner shell ionization

The HRTEM images and EELS of VGN, in present thesis, is carried out using HRTEM (LIBRA 200FE, Zeiss) with 200 kV FE electron source. Samples are prepared by peeling the VGN from substrates and loaded on the Cu grids coated with lacey carbon.

### 2.4.3. Raman Spectroscopy

Raman spectroscopy is a well-established and powerful non destructive technique for structural characterization of nanomaterials. In addition to ascertaining the crystalline state, it is useful to investigate defects and disorder in the materials.<sup>1,7-9</sup>

When a light of energy  $h\nu_0$  ( $h$  = Plank constant,  $\nu_0$  = frequency of light) incident on the surface, it undergoes either elastic or inelastic scattering, schematic shown in Fig. 2.7(a). The elastic scattering is known as Rayleigh scattering, which has the highest probability. In inelastic scattering, vibrational energy changed by  $h\nu_s$ . The Raman line corresponds to energy of  $h\nu_0 - h\nu_s$  is referred as Stokes line, whereas energy of  $h\nu_0 + h\nu_s$  is referred as Anti-Stokes line [Fig. 2.7(a)]. The Stokes lines are generally recorded in spectrum due to its higher intensity compared to Anti-Stokes line. A general thumb rule is that molecules having polarizability are only Raman active.

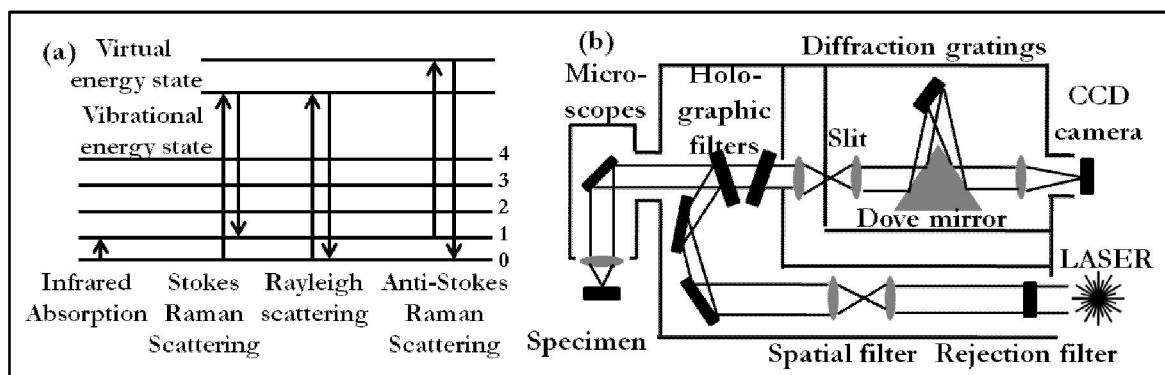


Figure 2.7: Schematic view of (a) scattering process in material with incident light, and (b) Raman spectrometer set up

The micro-Raman spectrometer (inVia, Renishaw, UK) extensively used for this thesis work is comprised of the following major components [Fig. 2.7(b)]:

- *Excitation Source*: Ar<sup>+</sup> laser with 514.5 and 488 nm excitation wavelengths
- Sample illumination through Leica *microscope* equipped with 10×, 20×, 50× and 100× *objective lenses*.
- *Diffraction gratings*: 1800 grooves/mm for the monochromatization of scattered signal
- *Thermoelectric cooled CCD* for detecting the signal in backscattering configuration

The detail analysis of the Raman spectra of VGN is given in Chapter 3 and 4. The laser power, throughout the thesis work, is kept below 3 mW to avoid sample heating and specimen decomposition. WIRE 3.2 software is utilized for fitting and extracting the data from Raman spectra. The Raman bands are fitted with Lorentzian peak after background subtraction.

#### 2.4.4. X-Ray Photoelectron Spectroscopy (XPS)

XPS is a surface sensitive analytical technique to give finger print information about chemical composition, nature of bonding and defects of the materials. The depth of information of this technique is 0.5-5 nm. When a surface is irradiated with X-rays in ultra-high vacuum, photoelectrons are emitted with the range of energy of 0-1400 eV. The schematic of photoelectron emission process is illustrated in Fig. 2.8(a). The kinetic energy of the emitted photoelectrons ( $E_k$ ) is given by

$$E_k = h\nu - E_b - W \quad (2.3)$$

Where  $h\nu$  is the energy of photons,  $E_b$  is the binding energy of the atomic orbital from which photoelectron emitted and  $W$  is the spectrometer work function. The chemical shifts,

arise due to the difference in chemical potential and polarizability of material, are used to identify the chemical state of the materials. The three basic components of XPS are given below [Fig. 2.8(b)]

- *X-ray source* : monochromatic Al ( $E_{K\alpha} = 1.4866$  keV) or Mg ( $E_{K\alpha} = 1.2566$  keV)
- *Ultra-high vacuum* ( $10^{-10}$  mbar) system
- *Hemispherical analyzer and detector*

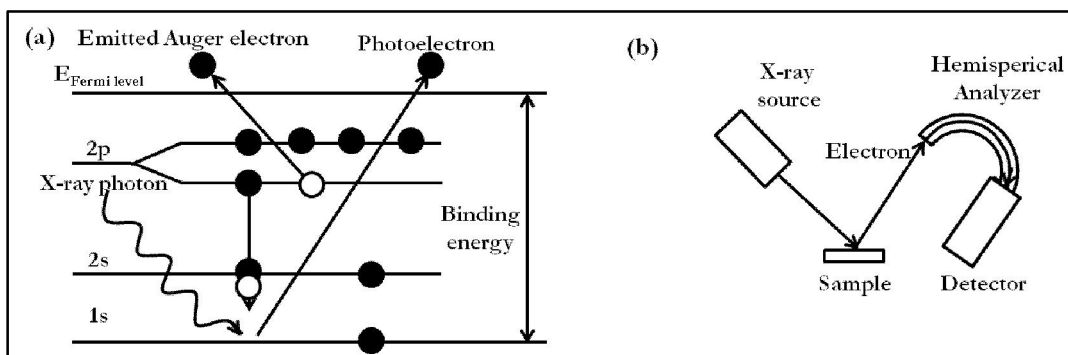


Figure 2.8: (a) Schematic view of X-ray induced photoelectron emission process and (b) block diagram of X-ray photoelectron spectroscopy.

The analysis of C1s spectra of VGN to investigate the growth mechanism can be found in Chapter 3. In this thesis, XPS (M/s SPECS, Germany) system with a monochromatic Al  $K\alpha$  (1.4866 keV) source at a relatively low power of 350 W and an analyser with pass energies of 10 and 50 eV are used. Curve fitting analysis was based on Shirley back-ground subtraction and application of Gaussian–Lorentzian line shapes.

## 2.5 Contact Angle measurement

The surface energy is one of the important parameters for the growth of thin film. In addition, wetting property of the thin film is subject of matter for their potential applications. The surface energy of substrate and wetting property of film are measured by “contact angle” of fluid droplet of a constant volume on the solid surface.

When a drop of liquid is placed on the solid surface, it experiences adhesive forces acting between the liquid/solid surface that favor spreading and cohesive forces within the liquid that counteract the spreading. The balance, is described by Young's equation (2.4), relates the contact angle to the surface free energies of a system containing solid (S), liquid (L), and vapor (V) phases, as shown in [Fig. 2.9(a)],

$$\gamma_{sv} - \gamma_{sl} = \gamma_{lv} \cos \theta \quad (2.4),$$

Where,  $\gamma_{sv}$ ,  $\gamma_{sl}$  and  $\gamma_{lv}$  represent the surface free energy of solid, solid/liquid interface and liquid, respectively. Depending on the value of contact angle, the wetting nature of the surface can be classified into four categories: hydrophilic, superhydrophilic, hydrophobic and superhydrophobic [Fig. 2.9(b)]. In addition to that, surface energy of the substrate also can be calculated from contact angle measurements by measuring it under different liquids. In general, higher the contact angle, lower the surface energy.

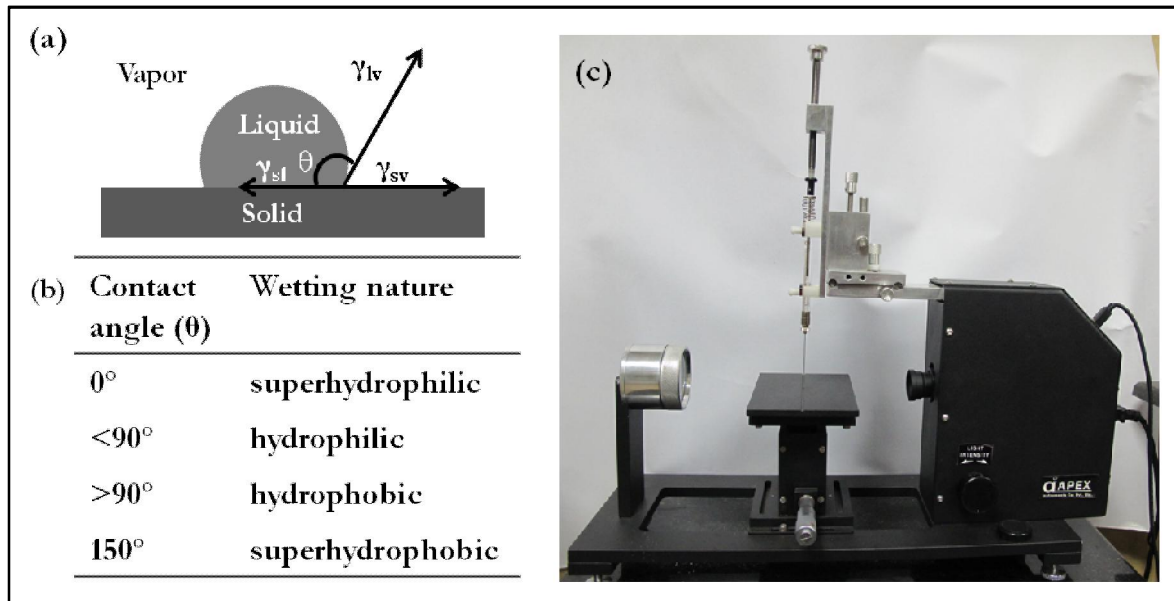


Figure 2.9: (a) Schematic of contact angles (CA) formed by sessile liquid drops on smooth homogeneous solid surface, (b) table of CA with wetting property and (c) Contact angle measurement set up in our lab.

The contact angle measurement set up is shown in Fig. 2.9(c). The major components of the set up are as follows:

*Light source*

*Microsyringe connected with screw gauge:* To put a droplet with constant volume

*CCD camera interfaced with computer:* to measure the contact angle

The contact angle of the VGN surface with water, 1M Na<sub>2</sub>SO<sub>4</sub>, 1M KOH and 1M H<sub>2</sub>SO<sub>4</sub> are measured by sessile drop method with the help of a CCD camera (Apex Instrument Co. Pvt. Ltd., India). The volume of the droplet is about 2μl and all measurements are carried out in ambient conditions. The value of contact angle is evaluated by half angle fitting method provided with the instrument.

## **2.6 Fourier Transform Infrared (FTIR) Spectroscopy**

FTIR is one of the vibrational spectroscopic tools, where infra-red (IR) spectra are measured relies on the principle of transmission of light.<sup>1</sup> When a infrared radiation incident on the sample, molecules of sample selectively absorb radiation of specific wavelengths which cause the change in dipole moment of sample molecules. Consequently, the vibrational energy levels of sample molecules transfer from ground state to excited state. The frequency of absorption band, in the range of 4000-10 cm<sup>-1</sup>, is proportional to the energy difference between the vibrational ground state and excited states. The number of absorption peaks depends on the number of vibrational degrees of freedom of the molecule. The intensity of absorption peaks depends on the the possibility of transition of energy levels and change in dipole moment. Therefore, it is utilized for identifying the structure and presence of functional group in the materials.

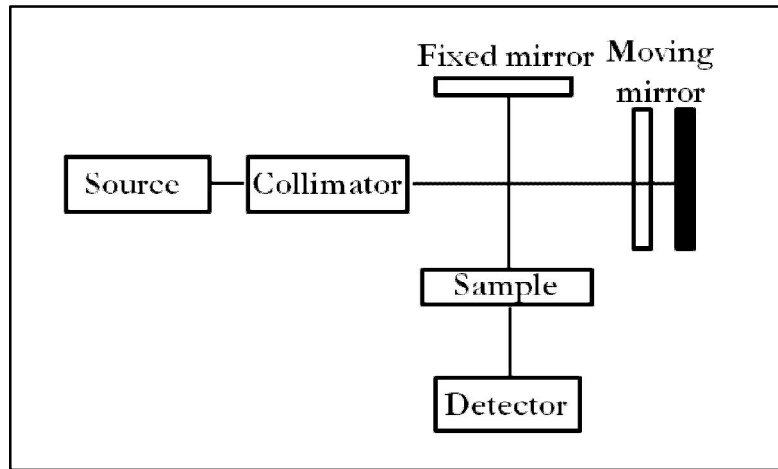


Figure 2.10: The block diagram of Fourier transform infra-red spectroscopy

The block diagram of FTIR is depicted in Fig. 2.10. FTIR spectra are recorded from  $4000\text{ cm}^{-1}$  to  $500\text{ cm}^{-1}$  on an ABB-MB3000 spectrometer equipped with a Deuterated Triglycine Sulphate (DTGS) detector. All measurements are made using 32 scans and  $4\text{ cm}^{-1}$  resolution. Horizon MB Software is used to process and analyze the spectra.

## 2.7 Four-probe Resistive method

The sheet resistance is one of the parameters of electrical properties of the material.<sup>10</sup> The four-point probe is generally used to measure the sheet resistance. Considering arbitrary shape of the material [Fig. 2.11(a)] and assuming the following conditions,

- (i) contacts are at the circumference of the sample and sufficiently small,
- (ii) the sample is uniformly thick and surface of the sample is singly connected,

the sheet resistance ( $R_{sh}$  in  $\Omega / \square$ ) can be expressed as

$$R_{sh} = \frac{\rho}{t} = \frac{\pi}{\ln 2} \left( \frac{R_{12,34} + R_{23,41}}{2} \right) F \quad (2.5)$$

where  $\rho$  is the resistivity of the material and  $t$  is the layer thickness

resistance  $R_{12,34}$  is defined as

$$R_{12,34} = \frac{V_{34}, \text{ voltage difference between contacts 3 and 4}}{\text{current}(I_{12}) \text{ enters sample through contact 1 and leaves through contact 2}} \quad (2.6)$$

similarly  $R_{23,41}$  and  $F$  is van-der Pauw correction factor, which is satisfying the relation

$$\frac{R_r - 1}{R_r + 1} = \frac{F}{\ln 2} \operatorname{ar\,cosh} \left( \frac{\exp(\ln 2)/F}{2} \right) ; R_r = \frac{R_{12,34}}{R_{23,41}} \quad (2.7)$$

Fig. 2.11(b) illustrated the dependence of  $F$  on  $R_r$ .

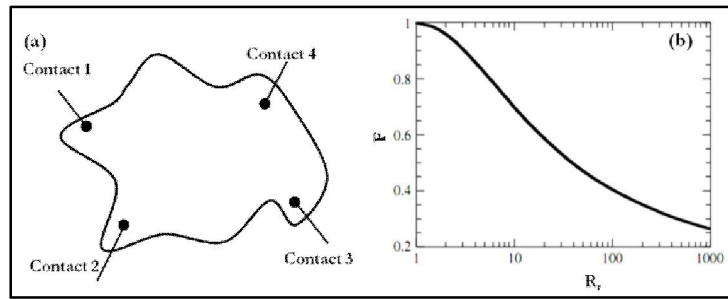


Figure 2.11: (a) Four point probe contact on the arbitrary shape of the material, and (b) the van der Pauw correction factor,  $F$  vs  $R_r$  (taken from Ref. <sup>10</sup>)

From the macroscopic point of view, considering the VGN as a plane membrane, the sheet resistance in current thesis is measured using Agilent B2902A precision source/measure unit. The contacts are made by Ag paste and Cu thin wire.

## 2.8 Three electrode electrochemical set up

The most suitable technique for fundamental studies on the electrochemical performance of single electrode is three electrode system.<sup>11</sup> A schematic of three-electrode system is depicted in Fig. 2.12(a). The major components are

- **Working electrode:** an electrode on which electrochemical reactions occur
- **Counter electrode:** serves as current source/sink. In general, inert materials like graphite, platinum foil, gold and glassy carbon are used to complete the circuit.

- **Reference electrode:** to maintain the constant potential during experiments. Most commonly and commercially available reference electrodes are Silver/Silver Chloride, Saturated Calomel, Mercury/Mercury (mercurous) Oxide, Mercury/Mercury Sulfate and Copper/Copper Sulfate.
- **Electrolyte:** an electrically conducting solution, where electrodes are immersed for carrying out the electrochemical experiments.

Figure 2.12(a) shows the block diagram of potentiostat/galvanostat of AUTOLAB, Metrohm, which is used for electrochemical performance of working electrode. The electrochemical performance as supercapacitor electrode are carried out by three different techniques in three-electrode system:

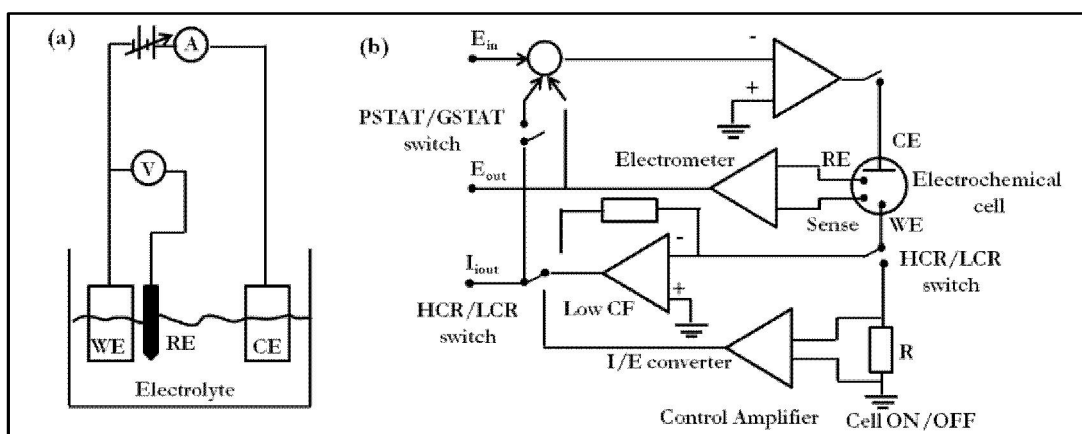


Figure 2.12: (a) Schematic of three-electrode system, and (b) block diagram of potentiostat/galvanostat

- **Cyclic Voltammogram:** it is a plot of current flow through the cell against the fixed potential window at a constant scan rate. Potential window depends on the nature of electrolyte and electrolyte/electrode interaction. Generally the potential window is fixed below the thermodynamic stability window of water for aqueous electrolyte and it can be increased while using organic electrolyte. A linear voltage ramp is used for the scanning within the defined potential window.

- **Charge-discharge:** it's a plot of voltage vs time of interaction at a fixed current. An ideal capacitor can be charged and discharged for infinite cycles, thus cycle life is one of the important parameters for the electrochemical performance of material.
- **Impedance Spectroscopy:** Electrochemical impedance spectroscopy (EIS) is a fundamental tool to get insights of the behavior of electrode materials used for energy storage in an electrolyte.<sup>12-15</sup> It is a technique to find out dependence of impedance on frequency by applying small ac perturbation to the electrochemical cell and one can obtain Nyquist plot (real vs imaginary part of impedance at corresponding frequency), Bode plot (Phase angle vs frequency) and frequency dependent capacitance.

More details on the cyclic voltammogram (CV), charge-discharge, impedance spectroscopy and equivalent circuit model is discussed in Chapter 5. The electrical contact on top of VGN is made by thin copper wire and Ag paste. Electrochemical experiments are performed using Metrohm-Autolab work station (model PGSTAT302N, Netherland). The VGN, Ag/AgCl (3M KCl) and Pt foil (1.5 cm × 1.5 cm) are used as working, reference and counter electrodes, respectively. The EIS measurements are performed in the frequency range 10 kHz to 0.1 Hz at open circuit potential with an ac perturbation of 10 mV. The Nyquist plots are fitted with appropriate equivalent electric circuit using EIS spectra analyzer software to understand the electrolyte/electrode interface behaviour.<sup>16</sup>

## 2.9 Summary

The experimental techniques utilized for the study of VGN are described briefly with basic working principle of operation, major components of the apparatus and their technical specifications with schematic or block diagrams.

**2.10 References**

1. Chu, P. K., and Li, L., *Mater. Chem. Phys.* (2006) **96** (2), 253
2. Jaeger, R. C., *Upper Saddle* (2002)
3. Gordillo Vazquez, F. J., *et al.*, *Chem. Vap. Deposition* (2007) **13** (6-7), 267
4. Levchenko, I., *et al.*, *J. Vac. Sci. Technol. A* (2013) **31** (5), 050801
5. Singh, S., *et al.*, *Bull. Mater. Sci.* (2008) **31** (5), 813
6. Muñoz, R., and Gómez-Aleixandre, C., *J. Phys. D: Appl. Phys.* (2014) **47** (4), 045305
7. Ferrari, A. C., and Robertson, J., *Philos. Trans. R. Soc. London, Ser. A* (2004) **362** (1824), 2477
8. Ferrari, A. C., and Basko, D. M., *Nat. Nanotechnol.* (2013) **8** (4), 235
9. Malard, L., *et al.*, *Phys. Rep.* (2009) **473** (5), 51
10. Schroeder, D. K., *New York: John Wiley and Sons Publisher* (1990)
11. Compton, R. G., and Banks, C. E., *Understanding voltammetry*. World Scientific: 2007
12. Rubinson, J. F., and Kayinamura, Y. P., *Chem. Soc. Rev.* (2009) **38** (12), 3339
13. Sugimoto, W., *et al.*, *J. Phys. Chem. B* (2005) **109** (15), 7330
14. Wang, D.-W., *et al.*, *J. Phys. Chem. B* (2006) **110** (17), 8570
15. Bandarenka, A. S., *Analyst* (2013) **138** (19), 5540
16. Bondarenko, A., and Ragoisha, G., *Progress in Chemometrics Research, Nova Science Publishers, New York* (2005), 89

# 3

## **Growth Mechanism of Vertical Graphene Nanosheets**

*To get to know, to discover, to publish - this is the destiny of scientist*

*Francois Arago*

The present Chapter focuses on understanding growth of vertical graphene nanosheets (VGN) under complex plasma chemistry. The influence of growth time, feedstock gas composition and growth temperature on the growth of VGN on SiO<sub>2</sub>/Si using electron cyclotron resonance-plasma chemical vapor deposition are investigated. The synthesized materials are characterized by scanning electron microscopy, transmission electron microscopy, Raman spectroscopy, X-ray photoelectron spectroscopy and four probe sheet resistance measurements. Based on the above experimental observations, a phenomenological four-stage model is discussed to substantiate the nucleation and growth mechanism of VGN, by invoking substrate–plasma interaction during growth.

### **3.1 Introduction**

The growth, morphology and structure-property of vertical graphene nanosheets (VGN) grown by plasma enhanced chemical vapor deposition (PECVD) are strongly influenced by several process parameters during growth. The major parameters include chamber geometry, plasma source, growth time, feedstock gas composition, growth temperature, nature of substrates and substrate position in plasma plume. Despite several existing reports, it should be noted that there is still no unique theory that can explain the atomistic growth mechanism to provide guidelines for optimizing the process parameters for a given plasma source deposition system. Further, the PECVD synthesized materials suffer from large amount of defects due to ion bombardment from the high density plasma. In order to realize and enhance the full potential of these materials, a systematic study on growth of VGN under different gas compositions in single growth technique is highly desirable. Moreover, the study is required for clear understanding on defect induced growth to tune their structure-property. While the feedstock gas compositions decide the plasma environment, growth temperature is found to play a role on surface reaction kinetics and growth time allows the structure with its most favorable form. Therefore, the growth of VGN is carried out with the variation of growth time, feedstock gas composition and growth temperature, while effects of other process parameters like microwave power and distance from plasma source to substrate on the growth are addressed in Chapter 4.

### **3.2 Time dependent growth**

The time dependent growths of VGN were carried out by varying growth time from 10 sec to 45 min, while other process parameters are kept constant. The growth parameters are listed in Table 3.1. Ultrasonically, cleaned substrates were loaded into the substrate

holder kept at a distance of 40 cm from plasma source and the chamber was evacuated down to a base pressure of  $5 \times 10^{-6}$  mbar by turbo molecular pump. The substrate temperature was increased to 750 °C and after 20 min annealing, the substrate was cleaned by Ar plasma for 10 min at 200 W MW power. After that CH<sub>4</sub> was fed into the chamber through a circular showerhead at 2.5 sccm flow rate, while the Ar flow was reduced to 2.5 sccm. Following the growth, the plasma was turned off and the substrates were annealed for 10 min at the same growth temperature. Finally, samples were cooled to room temperature and were taken out for various characterizations.

Table 3.1: Experimental parameters for time dependent growth of VGN

CH <sub>4</sub> /Ar flow (sccm)	Growth temperature (°C)	Microwave power (W)	Chamber pressure (mbar)	Growth time
2.5/2.5	750	400	$1 \times 10^{-3}$	10 sec – 45 min

### 3.2.1 FESEM analysis

The surface morphologies of the VGN are characterized by FESEM at different stages of growth [Fig. 3.1(a–f)]. At the very early stages of growth, of about 10 sec duration, the film consists of many island-like structures over the smooth substrate as seen in Fig. 3.1(a). It should be noted that, the film is found to be continuous and electrically conductive with sheet resistance of about 30 kΩ/□ even at this short growth duration. As seen from Fig. 3.1 that the nanocrystalline graphitic film (NG) is getting transformed to vertically oriented open network structure with increasing growth time. The insets in Fig. 3.1(c–f) show the corresponding cross-sectional FESEM images of VGN that indicate the increment of vertical height to 48 nm at 45 min of growth. Further, a detailed Raman and

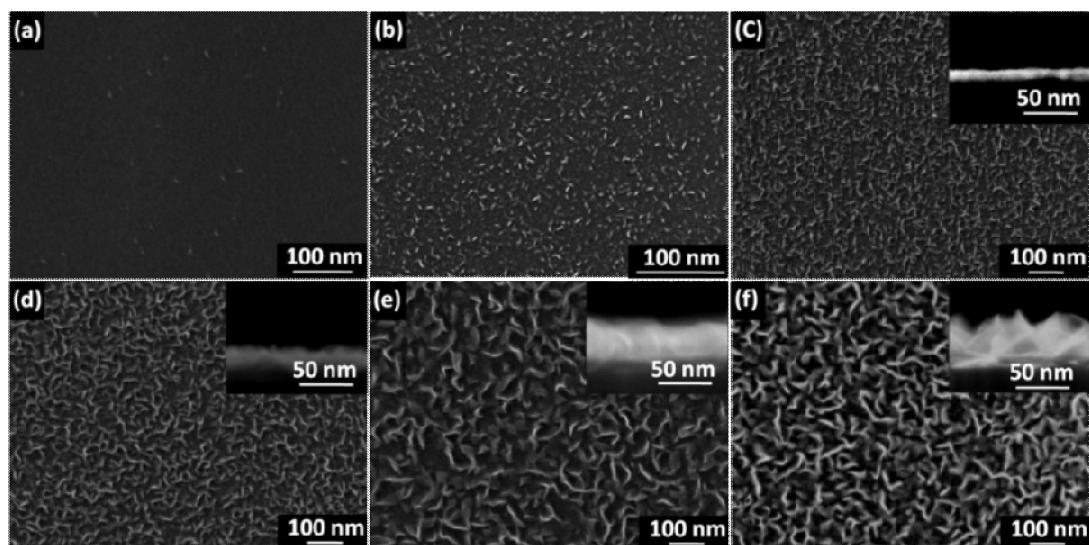


Figure 3.1: FESEM micrographs of VGN grown at different duration of (a) 10 sec, (b) 1 min (c) 5 min, (d) 10 min, (e) 20 min, and (f) 45 min. Inset of Fig. (c-f) represent corresponding cross-sectional FESEM micrograph of the films.

XPS analyses are carried out to substantiate the growth mechanism as discussed in the succeeding text.

### 3.2.2 Disorder induced two-stage growth

The typical Raman spectra of VGN is shown in Figs. 3.2(a) and 3.2(b). The spectra consist of two prominent bands - G and G' (also called as 2D) centered at  $\sim 1580$  and  $2700$   $\text{cm}^{-1}$ , respectively, which are characteristic of graphitic structure. The G band is associated with the bond stretching of all pairs of  $sp^2$  atoms in both rings and chains.<sup>1</sup> The G' band is due to the inter-valley double resonance (DR) or triple resonance process.<sup>2</sup> Also, the spectra consists of bands due to one phonon defect-assisted processes, such as D, D' and D'' bands and two phonon defect-assisted processes, such as 2D', D+D' and D+D'' bands. The D, D', 2D', D'', D+D' and D+D'' bands are activated only by defects and these bands are absent in graphene. Also, these bands are strongly dispersive with excitation energy due to the presence of defects and disorder.<sup>3</sup> The D band ( $\sim 1350$   $\text{cm}^{-1}$ ) and D' band ( $\sim 1620$

$\text{cm}^{-1}$ ), respectively, originate from the process of inter-valley and intra-valley DR. The D band is due to the breathing mode of  $sp^2$  atoms in rings.<sup>1</sup> The  $2D'$  band is the overtone of D' band and appears at  $\sim 3250 \text{ cm}^{-1}$ . The peak at  $\sim 2485 \text{ cm}^{-1}$  is assigned to  $D+D''$  band, which is due to the combination of D phonon and the zone boundary phonon corresponding to LA branch at  $1100 \text{ cm}^{-1}$ .<sup>3</sup> The weak and broad band around  $1100 \text{ cm}^{-1}$ , as shown in inset of Fig. 3.2(a), could arise from bond stretching mode of  $sp^3$  sites of hydrogenated carbon traces.<sup>4</sup> Figure 3.2(c) shows the Raman spectra of VGN grown for different deposition time ranging from 10 sec to 45 min. The Raman spectrum of the film grown for 10 sec shows a very broad D and G bands with nearly negligible  $G'$  band intensity indicative of a more disordered structure in NG. The intensity increases and full width at half maximum (FWHM) of the D, G, and  $G'$  bands decreases with growth time [Figs. 3.2(c,d)]. In addition to that the intensity ratio of  $G'$  and G band ( $I_{G'}/I_G$ ) is found to increase with growth time [Fig. 3.2(e)]. The increase in growth time shifts the G band position [Pos(G)] from  $1598.0$  to  $1590.7 \text{ cm}^{-1}$  indicating improvement in crystallinity [Fig. 3.2(f)].<sup>5</sup> The other two bands, D and  $G'$ , do not show any systematic change in peak position with respect to growth time. The observed large D band intensity is due to the presence of disorder, which arises from large amount of edge states,  $sp^3$  bonded C-H species, nanographitic base layer and ion-induced defects from the plasma during growth.

Since, all VGN consist of large amount of defects, it is important to study defects associated with growth and their correlation. In recent times, considerable efforts are devoted to investigate the nature of defects and its quantification by introducing specific type of defects in graphene through controlled bombardment by  $\text{Ar}^+$ -ion or plasma surface modification.<sup>6-11</sup> According to resonant Raman scattering theory, intensity of defect bands ( $I_D, I_{D'}$ ) not only depends on the amount of defects but also on the type of defects

associated with it. The ratio,  $I_D/I_{D'}$  would provide information about the types of defects present in the material and listed in Table 3.2. Figure 3.2(g), plot of  $I_D/I_G$  vs  $I_{D'}/I_G$ , shows a linear behavior and agrees well with earlier reports.<sup>12</sup> The observed slope is found to be  $8.6 \pm 2.9$  indicating the existence of combined vacancy-like and hopping defects in the VGN.<sup>11,12</sup>

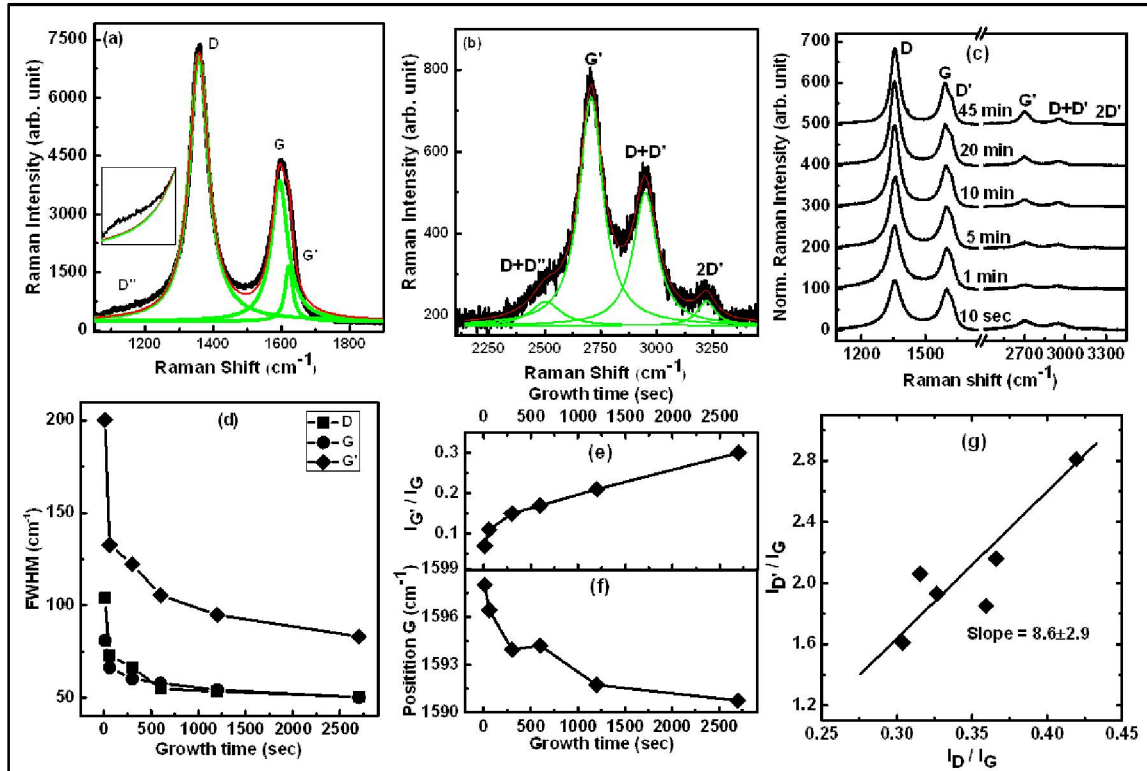


Figure 3.2: (a) First order and (b) second order typical Raman spectrum of vertical graphene nanosheets (VGN) and its deconvolution with Lorentzian line shape, (c) vertically stacked up of Raman spectra of VGNs at different growth duration of 10 sec, 1, 5, 10, 20, and 45 min, (d) FWHM of D, G, and G'-bands, (e) variation of G-band position (f)  $I_G/I_G$  with respect to growth time and (g) plot of  $I_D/I_G$  vs  $I_{D'}/I_G$  for VGN. Connecting solid lines in Fig. 4(d-f) are guide to eye.

Table 3.2: Types of defects in graphitic structure based on  $I_D/I_{D'}$  ratio<sup>11,12</sup>

$I_D/I_{D'}$	13	10.5	7	3.5	1.3
Type of defects	$sp^3$ related	hopping	vacancy-like	boundary-like	on-site

In a disordered graphitic system, it is known that the  $I_D/I_G$  provides a measure of defects/disorder in the film. Figure 3.3(a) shows the variation of  $I_D/I_G$  with respect to growth time. It indicates that the  $I_D/I_G$  ratio has a non-monotonic dependence on increasing growth time, i.e., increases with growth time up to 10 min, and then decreases beyond 10 min. However, as discussed earlier [Fig. 3.3(d)], the decreased FWHM of D, G, and G' bands signify the reduction of defects and disorder in VGN with growth time. Hence, the non-monotonic behavior of  $I_D/I_G$  ratio with growth time suggests the existence of two disorder-induced competing mechanisms contributing to the D band intensity. This behavior can be understood in terms of amorphization trajectory model of graphitic materials, proposed by Ferrari and Robertson.<sup>1</sup> The transformation of primarily  $sp^2$  bonded graphite into primarily  $sp^3$  bonded tetrahedral amorphous carbon ( $ta-C$ ) occurs through three stages, viz.

- (i) graphite to NG [low defect (LD)],
- (ii) NG to nominal  $sp^3$   $a-C$  [high defect (HD)], and
- (iii) nominal  $sp^3$   $a-C$  to primarily  $sp^3$   $ta-C$ .

The origin of D band intensity is different in each stage. It is established that the  $I_D$  is directly proportional to the amount of defects in stage 1 and inversely proportional to defects in stage 2, while  $I_G$  is always proportional to the amount of  $sp^2$  rings present in the sample.<sup>8,12</sup> Hence, the non-monotonic behavior of  $I_D/I_G$  with growth time is attributed to the transformation of defects and disorder from stage 2 to stage 1. Thus, the VGN grown for  $\leq 10$  min and  $> 10$  min follow the stage 2 and stage 1, respectively. According to the model developed by Cancado *et al.*,<sup>8</sup> the inter defect distance ( $L_D$ ) and defect density ( $n_D$ ) can be estimated in ion bombarded graphene by Raman spectroscopy with appropriate boundary conditions and quantified in stage 1 and stage 2 as given in the succeeding text.

$$\text{Low Defect regime: } L_D^2 = 4.3 \times 10^3 E_L^{-4} \left[ \frac{I_D}{I_G} \right]^{-1} \quad (3.1)$$

$$n_D = 7.3 \times 10^9 E_L^4 \left[ \frac{I_D}{I_G} \right] \quad (3.2)$$

$$\text{High Defect regime: } L_D^2 = 5.4 \times 10^{-2} E_L^{-4} \left[ \frac{I_D}{I_G} \right] \quad (3.3)$$

$$n_D = 5.9 \times 10^3 E_L^{14} \left[ \frac{I_D}{I_G} \right]^{-1} \quad (3.4)$$

where  $E_L$  is excitation laser energy. The  $L_D$  and  $n_D$  calculated using Eqns. 3.1, and 3.2 are valid for LD regime (stage 1), for films grown for  $>10$  min and  $L_D$  and  $n_D$  evaluated using Eqns. 3.3, and 3.4 are valid for HD regimes (stage 2), for films grown for  $\leq 10$  min.

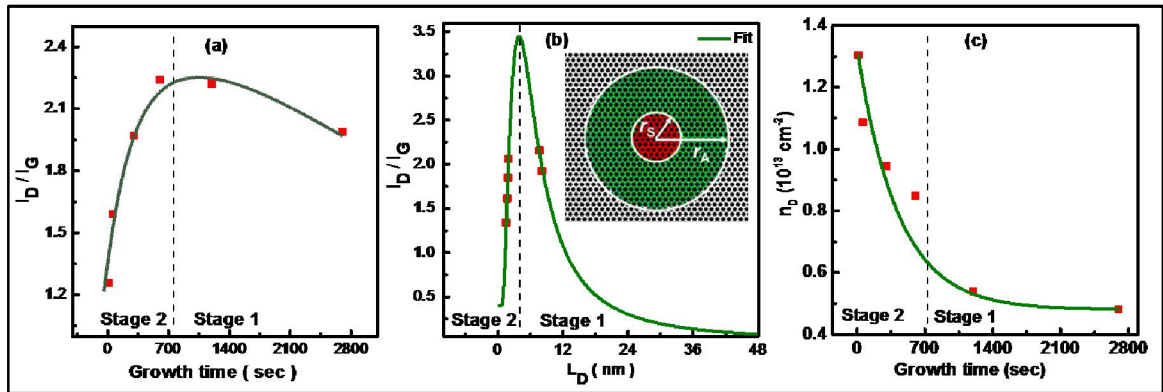


Figure 3.3: (a) Variation of  $I_D/I_G$  with respect to growth time, (b) the plot of  $L_D$  vs  $I_D/I_G$  and inset represents the schematic definition of “activated” A-region (green) and “structurally-disordered” S-region (red) according to Lucheese’s model. (Ref. <sup>9</sup>) (c) the calculated defect density with growth time for VGN. Solid line in Fig. 3.3(b) is fit to the experimental data along with simulated curve with the same fitting parameters ( $0 < L_D < 50$  nm). The fitting is performed using Eqn. 3.5. Solid line in the Fig. 3.3(a and c) is guide to eye.

The non-monotonic behavior is also observed from the plot of  $I_D/I_G$  with respect to  $L_D$  [Fig. 3.3(b)]. The mechanism for such behavior is discussed earlier [Fig. 3.3(a)] and is also reported for ion bombarded graphene which is explained with a phenomenological model for quantifying ion-induced defects in graphene.<sup>9</sup> According to the model,

$$\left[\frac{I_D}{I_G}\right] = C_A \left(\frac{r_A^2 - r_S^2}{r_A^2 - 2r_S^2}\right) \left[ \exp\left(\frac{-\pi r_S^2}{L_D^2}\right) - \exp\left(-\pi \frac{r_A^2 - r_S^2}{L_D^2}\right) + C_S \left\{1 - \exp\left(\frac{-\pi r_S^2}{L_D^2}\right)\right\} \right] \quad (3.5)$$

where  $C_A$  and  $C_S$  are the maximum possible value of  $I_D/I_G$  when the hexagonal network of carbon atoms are not disturbed and highly disordered limit, respectively. The parameters  $r_A$  and  $r_S$  are the radius of defect activated region and structurally disordered region, respectively (with  $r_A > r_S$ ) [inset of Fig. 3.3(b)]. The solid line in Fig. 3.3 (b) is the fit to the experimental data along with simulated curve with the same fitting parameters ( $0 < L_D < 50$  nm) and finds an excellent agreement with the model. The best fit parameters are found to be  $r_A = 3.81$  nm,  $r_S = 1.08$  nm,  $C_A = 5.0$ , and  $C_S = 0.4$ , which are closely matching to the reported values.<sup>9</sup> The fitted curve indicates an initial increase of  $I_D/I_G$  ratio up to a critical  $L_D$  value of about 3.8 nm and then a monotonic decrease with increase in  $L_D$ .<sup>7-9</sup> Hence, this plot clearly indicates, in present scenario, that the transformation of defects and disorder with growth time, which demonstrates the cross over from stage 2 to stage 1 of Ferrari and Robertson model.<sup>1</sup> As it can be seen from the Fig. 3.3(c), the defect concentration continuously decreases with growth time. Thus, the Raman studies verify the defect associated evolution of VGN. It is found that the defect density is very high at early stage of growth due to the NG island formation. Later, the defect density monotonically decreases because of the formation of high pure VGN. These observations are in excellent agreement with the growth mechanism as discussed in FESEM analysis.

### 3.2.3 XPS analysis

In order to strengthen the growth mechanism obtained from FESEM and defect transformation at different stages obtained from Raman spectroscopy, XPS studies of VGN are carried out. The Fig. 3.4(a) shows the high resolution C1s XPS spectra of the films grown for 10 sec, 10 min and 45 min. The XPS spectra show a clear asymmetry in the

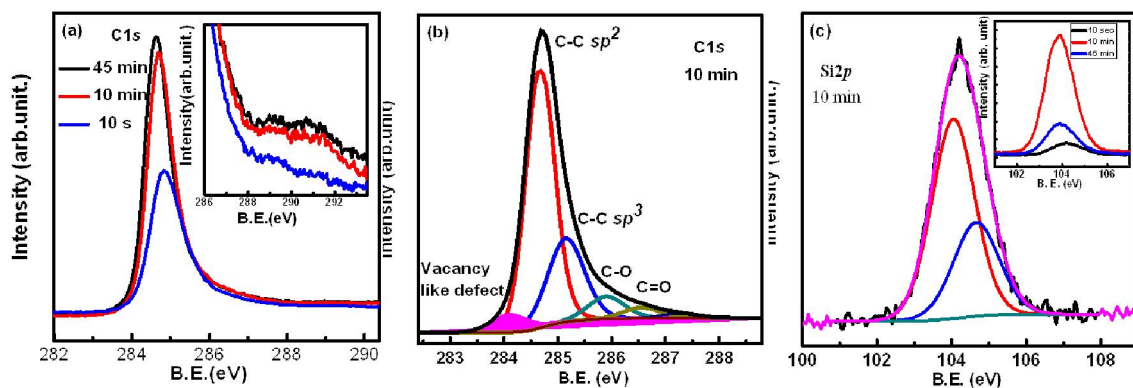


Figure 3.4: (a) The high resolution C1s spectra for the films grown for 10 s, 10 min, and 45 min, The inset in Figure (a) is an extended region of C1s at higher BE. (b) deconvoluted C1s spectrum for the film grown for 10 min, and (c) the Si2p XPS spectrum for 10 sec grown film.

higher binding energy (BE) regime for all the three samples, which is typically observed for high conductive metals and also the asymmetry is found to increase with increasing growth time. These observations suggest the highly conducting graphitic nature of VGN.<sup>13,14</sup> As seen in Fig. 3.4(a), the peak position of C1s spectra is found to shift toward lower BE with growth time. The deconvoluted high resolution C1s spectrum of the film is shown in Fig. 3.4(b). The main peak at 284.4 eV corresponds to C=C  $sp^2$  bonded graphitic structure and peak around 285.1 eV corresponds to defect structure arising from C–H related  $sp^3$  bonded structure.<sup>15–17</sup> This C–H related  $sp^3$  bonded structure is further confirmed by FTIR spectroscopy, which shows absorption peaks at around 2958 and 2875  $\text{cm}^{-1}$  corresponding to the asymmetric and symmetric  $sp^3$ –CH<sub>3</sub> vibration, respectively [Fig. 3.5(a)].<sup>18</sup> In addition, the peaks related to C–O, C=O bonding, probably from adsorbed impurities, are also observed. One more peak near 284.1 eV, which is closely matching to the BE for Si–C formation, is also observed. In order to verify Si–C formation at SiO<sub>2</sub>-NG interface during the nucleation process, Si2p XPS spectra are recorded for all the three samples and shown in Fig. 3.4(c). The absence of peak at 100.8 eV rules out the possibility

for the formation of Si–C. This result also agrees with the Raman measurements, where no Si–C formation is observed, which should have a phonon mode at about  $800\text{ cm}^{-1}$ .<sup>17,19</sup> Hence, we exclude the phenomenon of Si–C formation, which is reported in some earlier studies. To account for the peak with chemical shift lower to BE of C1s, Barinov *et al.*<sup>20</sup> had demonstrated that the peak in multiwalled CNT was due to the vacancies and they also verified it on the intentionally introduced vacancy-like defects in highly oriented pyrolytic graphite (HOPG). Hence, the peak at around 284.1 eV can be assigned as the signature of vacancy-like defects in VGN. This result shows an excellent agreement with the Raman analysis. Moreover, the hopping defects and vacancies are closely related in disordered system because the hopping of charge carriers/atoms can take place on the vacancy sites.<sup>20</sup> As shown in Table 3.3, area under the curves for defect related peaks continuously decreases, which indicates the lowering of defect density with growth time. Further, as seen in inset of Fig. 3.4(a),  $\pi$ - $\pi^*$  energy loss peak increases with growth time indicating more conductive graphitic structure in the 45 min grown VGN. These results confirm the evolution of refined graphitic structure with time.

Table 3.3: Extracted parameters from XPS analysis of the VGN

Growth time	C=C $sp^2$		C-H $sp^3$ defect		C-O		C=O		Vacancy defect	
	BE (eV)	Area (%)	BE (eV)	Area (%)	BE (eV)	Area (%)	BE (eV)	Area (%)	BE (eV)	Area (%)
10sec	284.71	45.2	285.21	36.2	286.00	6.7	286.65	3.8	284.2	6.67
10min	284.65	59.8	285.15	24.3	285.90	6.5	286.55	3.1	284.1	4.98
45min	284.55	60.1	285.04	25.3	285.75	6.5	286.45	3.1	283.9	3.57

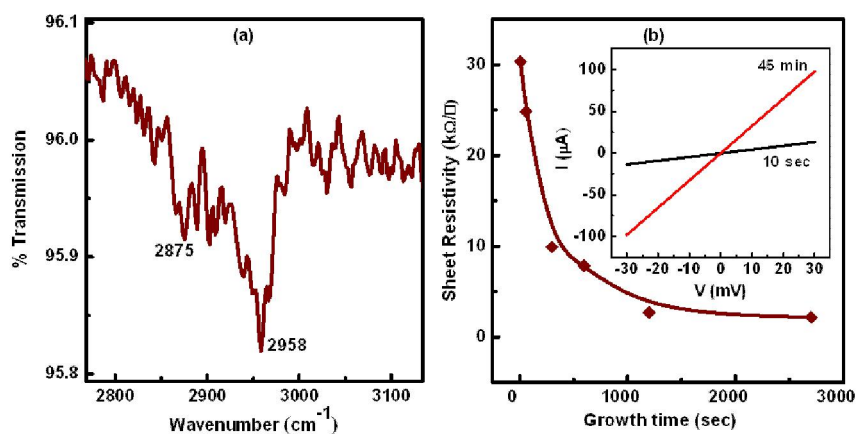


Figure 3.5: (a) FTIR spectra, and (b) the variation of sheet resistance vs growth time of VGN. Solid line in (b) is a guide to eye. Inset represents the Ohmic behavior of VGN grown at 10 sec and 45 min.

### 3.2.4 Electrical properties

Figure 3.5(b) shows room temperature sheet resistance of VGN, which decreases from 30 to 2.17 kΩ/□ with increasing growth time and the inset shows its Ohmic behaviour. The decrease in resistance with increasing growth time is mainly due to the growth of the high pure and high conductive VGN networks over the relatively high resistive NG layer. As growth time increases, the length and height of VGN increase with decrease in defect density as evidenced from Raman and XPS analysis. Hence, the sheet resistance decreases with growth time due to the domination of conducting pure VGN.

### 3.3 Role of feedstock gas composition

Growth experiments were carried out under various inlet gas compositions of CH<sub>4</sub>, Ar and H<sub>2</sub>, while other parameters like growth time, temperature, MW power and post-annealing time are kept constant. To make the analysis simple, samples are labeled in accordance with their constituent gas ratio (CH<sub>4</sub>:Ar:H<sub>2</sub>) and experimental results divided into three cases and listed in Table 3.4.

Table 3.4: Deposition parameters for VGN growth by ECRCVD under different feedstock gas composition

Growth time	30 min
Gas pressure	$2.8 \times 10^{-3}$ mbar
Microwave power	400 W
Growth temperature	800 °C
Distance between plasma source to substrate	40 cm
Case I: dilution of CH <sub>4</sub> (5 sccm) with Ar	5-35 sccm
Case II: dilution of CH <sub>4</sub> (5 sccm) with H <sub>2</sub>	5-35 sccm
Case III: dilution of CH <sub>4</sub> with a (Ar + H <sub>2</sub> )	
(a) dilution of CH <sub>4</sub> /H <sub>2</sub> (5sccm/5sccm) with Ar	0-35 sccm
(b) dilution of CH <sub>4</sub> /Ar (5sccm/5sccm) with H <sub>2</sub>	0-25 sccm
(c) increase CH <sub>4</sub> concentration in fixed Ar/H <sub>2</sub> (15sccm/5sccm)	5-25 sccm
Annealing time at 800 °C	30 min

### 3.3.1 FESEM analysis

#### *Case I: dilution of CH<sub>4</sub> with Ar*

Figure 3.6 shows the surface morphology of the NG structure (NGS) grown with CH<sub>4</sub> diluted with Ar in different ratios of CH<sub>4</sub>:Ar up to 1:7. It can be seen from Fig. 3.6(a) that decomposition of CH<sub>4</sub> alone can produce homogeneous film consisting of many island-like structures over the smooth substrate. Subsequently when Ar is introduced alongside CH<sub>4</sub>, the nanoisland structures get transformed into vertically oriented structures as shown in Fig. 3.6(b). A further increase in Ar increases the height of the VGN and decreases the number density of the sheets. However, the width and length of the vertical sheets increase with increased dilution by Ar as shown in Figs. 3.6(a)–(e). In addition, a substantial increase in height from 27.8 to 164.9 nm is observed when the Ar flow is increased from 5 to 35 sccm [Fig. 3.6(f)].

#### *Case II: dilution of CH<sub>4</sub> with H<sub>2</sub>.*

Figure 3.7 shows the surface morphology of NGS grown with CH<sub>4</sub> diluted with H<sub>2</sub> with different ratios of CH<sub>4</sub>:H<sub>2</sub> up to 1:7. The FESEM images show no specific features

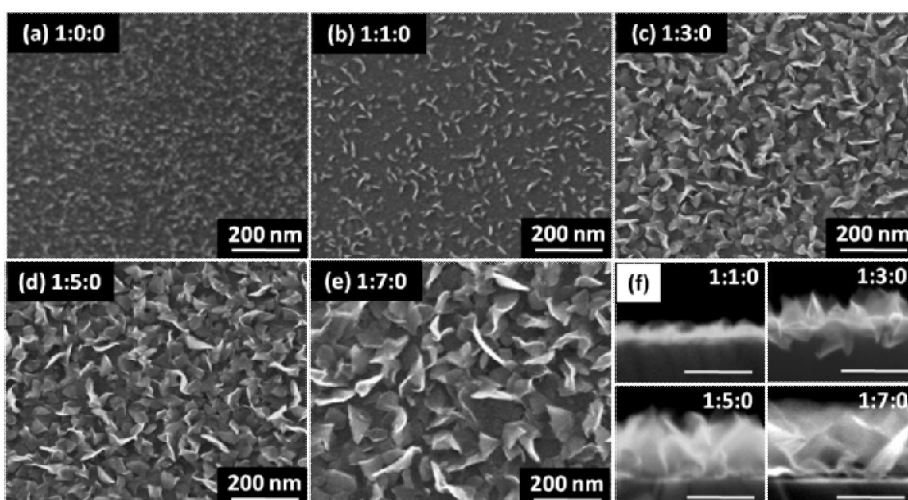


Figure 3.6: FESEM micrographs of VGN grown at different  $\text{CH}_4:\text{Ar}:\text{H}_2$  ratios: (a) 1:0:0, (b) 1:1:0, (c) 1:3:0, (d) 1:5:0, (e) 1:7:0 and (f) cross-sectional FESEM images of (b–e) with a 100 nm scale bar.

and the surfaces appear to be smooth. When  $\text{H}_2$  is introduced alongside  $\text{CH}_4$ , i.e. 1:1 and 1:3 ratios of  $\text{CH}_4:\text{H}_2$ , the apparent NGS [Fig. 3.7(a)] turned out to be a smooth few layer planar NG (FPNG) film [Figs. 3.7(b) and 3.7(c)]. A further increase in  $\text{H}_2$  flow leads to the formation of a NG structure over electrically continuous NGS, and to a discontinuous film for flow rates of  $\text{CH}_4:\text{H}_2$  at 1:5 and 1:7 ratios, respectively. Thus, with an increase in the  $\text{H}_2$  content, discontinuity in the films is observed with isolated clusters, and the growth of the film is hindered as shown in Figs. 3.7(a)–(d).

*Case III: dilution of  $\text{CH}_4$  with a gas mixture of  $\text{Ar} + \text{H}_2$*

As discussed in previous sections (cases I and II), the dilution of  $\text{CH}_4$  with Ar or  $\text{H}_2$  favors the formation of VGN and FPNG films, respectively. Taking a cue from these

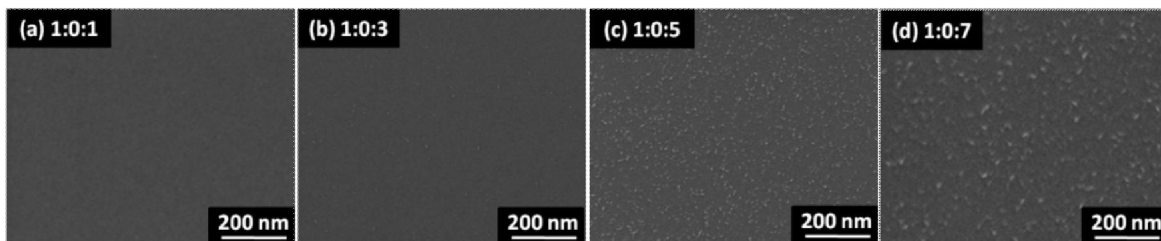


Figure 3.7: FESEM micrographs of a few layer planar nanographite films grown at different  $\text{CH}_4:\text{Ar}:\text{H}_2$  ratios (a) 1:0:1 (b) 1:0:3 (c) 1:0:5 and (d) 1:0:7.

experiments, a combination of these two dilution gases with  $\text{CH}_4$  was explored to study their impact on the morphology, growth rate and structural properties. The experiments performed were divided into three subcategories viz. (i) repetition of case I experiments with the addition of a constant volume of  $\text{H}_2$  [case III(a)], (ii) repetition of case II experiments with the addition of a constant volume of Ar [case III(b)] and (iii) increasing  $\text{CH}_4$  concentration with fixed Ar and  $\text{H}_2$  ratios [case III(c)].

Figure 3.8 shows the FESEM micrographs of the films grown with the dilution of  $\text{CH}_4$  with various concentrations of a gas mixture of Ar (or  $\text{H}_2$ ), containing a constant volume of  $\text{H}_2$  (or Ar). When repeating the case I and case II experiments with a mixture of constant  $\text{H}_2$  and Ar, respectively, the morphology of the NGS is found to change considerably. It is evident from the FESEM micrographs that the morphology can be tuned from perfect planar to highly dense vertical structures, with intermediate sparsely distributed vertical structures, which can be seen in Fig. 3.8. In case III(c), the concentration of  $\text{CH}_4$  alone is increased while keeping the amounts of Ar and  $\text{H}_2$  (1:3:1, 3:3:1 and 5:3:1 ratios) constant. The FESEM morphology of these films is shown in Figs. 3.8(b), 3.8(e) and 3.8(h). As shown in these images, the vertical structure systematically transforms into a planar structure upon increasing the  $\text{CH}_4$  concentration. The reason for the flipping of orientation is due to the abundance of nascent hydrogen that is released from fragmentation of  $\text{CH}_4$  in the plasma. Briefly, the morphology of NGS is mostly dependent on the nature of the dominant diluent gas. Hence, it is very clear that the surface morphology and the aerial density of the nanosheets can be completely controlled using optimal dilution ratios of Ar and  $\text{H}_2$  in  $\text{CH}_4$ .

Based on FESEM analysis, an attempt is made to derive a relationship between the morphology and the input gas compositions –  $\text{CH}_4$ , Ar and  $\text{H}_2$  – towards the growth of

NGS and a ternary field diagram demonstrating the growth regimes is derived and shown in Fig. 3.9. This figure provides an easy understanding of different growth morphologies

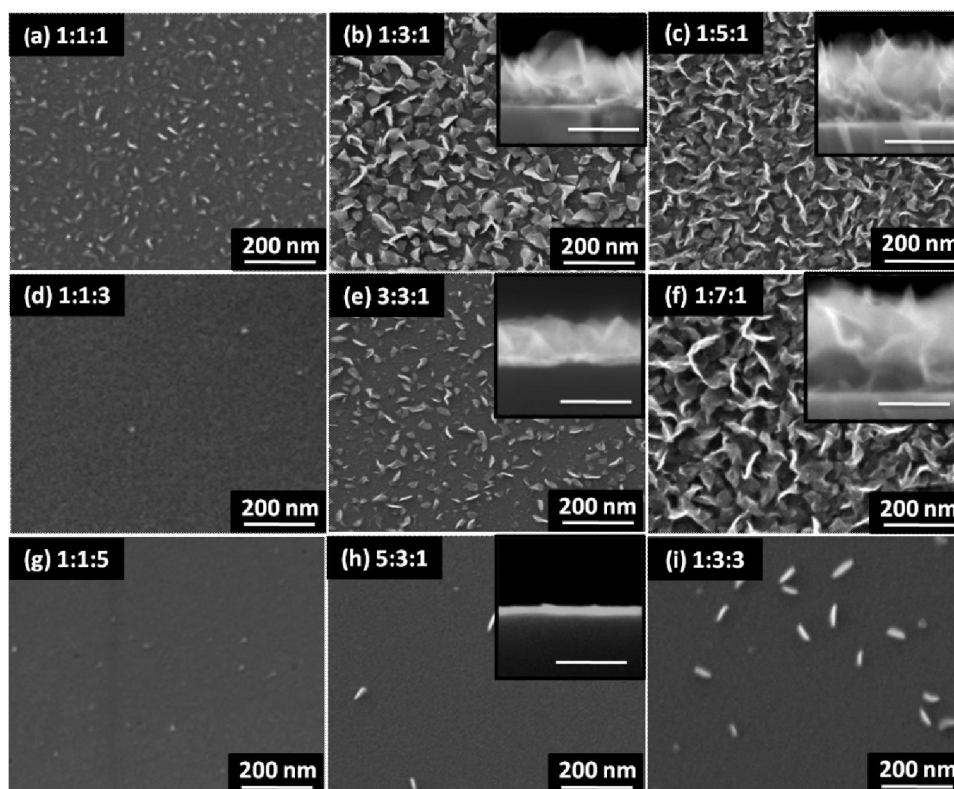


Figure 3.8: (a-i) FESEM micrographs of NGS grown under mixed Ar+H<sub>2</sub> dilution. The actual gas flow ratios are labeled on each image as CH<sub>4</sub>:Ar:H<sub>2</sub>, Insets represent cross-sectional FESEM image of respective film.

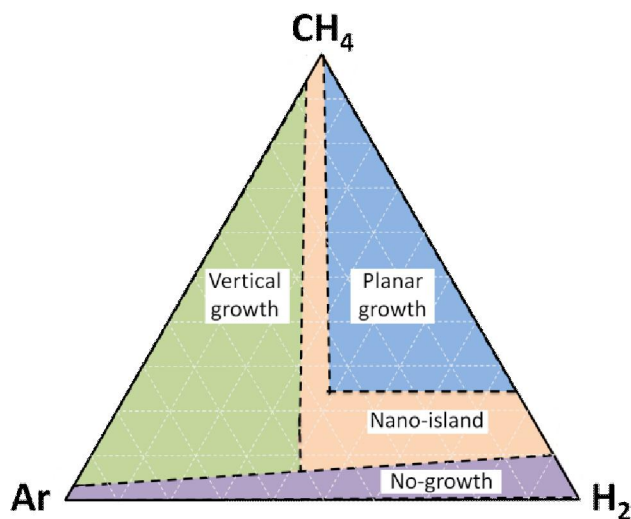
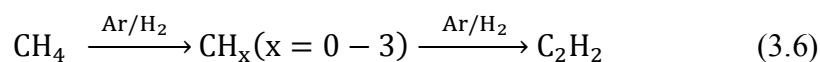


Figure 3.9: A tentative ternary field diagram indicating the growth of various NGS morphologies under different feedstock ratios.

and corresponding gas compositions. In essence, it is possible to tune morphological features of NGS with an optimal dilution of CH<sub>4</sub> with a mixed proportion of Ar and H<sub>2</sub> using a single experimental technique. The experimental observation shows that the vertical growth can be suppressed by tuning the H-content in the plasma. The growth kinetics that dictates formation of NGS of different morphologies can be better understood from the radicals produced in plasma under different dilution conditions. A few important metastable chemical reactions between the hydrocarbon and gases used for dilution in the plasma are given below<sup>21</sup>



C<sub>2</sub> and H<sub>2</sub> play an important role in the growth kinetics under MW plasma. C<sub>2</sub> and atomic hydrogen (H\*) radical density can be effectively controlled by H<sub>2</sub> content in the feedstock gases. If the plasma consists of a relatively high Ar concentration, the C<sub>2</sub> radicals' availability can be enhanced by energetic Ar<sup>+</sup> ions (Eqns. 3.6 and 3.7).<sup>21-23</sup> However, as the growth progresses, the H\* generated from the dissociation of CH<sub>4</sub> by MW energy also starts etching the growing film. Further, the H\* radicals can efficiently etch out *a*-C, weakly bonded carbon atoms and small graphitic fragments to prevent formation of additional graphene layers. Further, it enables the mobility of carbon adatoms to efficiently reduce the structural disorder.<sup>24</sup> The concurrent growth and etching processes cause the VGN to grow assisted by the inherent electric field, temperature and chemical potential gradient associated with plasma.<sup>25,26</sup> Further addition of H<sub>2</sub> in fixed proportion (5 sccm) along with Ar produces statistically more stable vertical structures while minimizing the

random orientations as evidenced by the cross sectional FESEM analysis [Figs. 3.6(f) and 3.8]. The preference for a planar morphology seen under H<sub>2</sub> dilution can be understood by the following: a higher dose of H<sub>2</sub> increases the density of C<sub>2</sub>H radicals (Eqn. 3.8) and thereby decreases the net C<sub>2</sub> density. In addition, the excess of H\* radicals leads to the chemical etching of the growing film as a result vertical growth is hampered under H<sub>2</sub>-rich dilution. However, a higher H<sub>2</sub> dilution leads to erosion of the initially grown layers into NG-islands over an electrically continuous NG film (1:0:5). A further increase in H<sub>2</sub> completely wipes out the film and forms discrete NG clusters over substrate surface (1:0:7).

### 3.3.2 HRTEM and EELS analysis

Figures 3.10(a,b) and 3.9(e,f) shows HRTEM micrographs of the films grown under the flow ratios of 1:7:0 and 1:0:5, respectively. The HRTEM analysis clearly confirms that NGS are composed of about 13 graphene layers as shown in Figs. 3.10 (a,e). The graphene sheets are by and large uniform in nature. However, the edges of VGN are found to be tapered [Fig. 3.10(a)]. The measured inter-layer spacings of the respective samples are found to be 0.356 and 0.364 nm, which are higher than that of graphite (0.334 nm). Figures 3.10(c) and 3.10(g) show the fast Fourier transform (FFT) images that correspond to the HRTEM images of Fig. 3.10(b) and (f) respectively. The elliptical pattern of both FFT images and increased interlayer spacing could be correlated to the stacking fault disorder called turbostratic graphite.<sup>27</sup> The enhanced growth kinetics under non-equilibrium conditions in the plasma leads to turbostratic disorder.

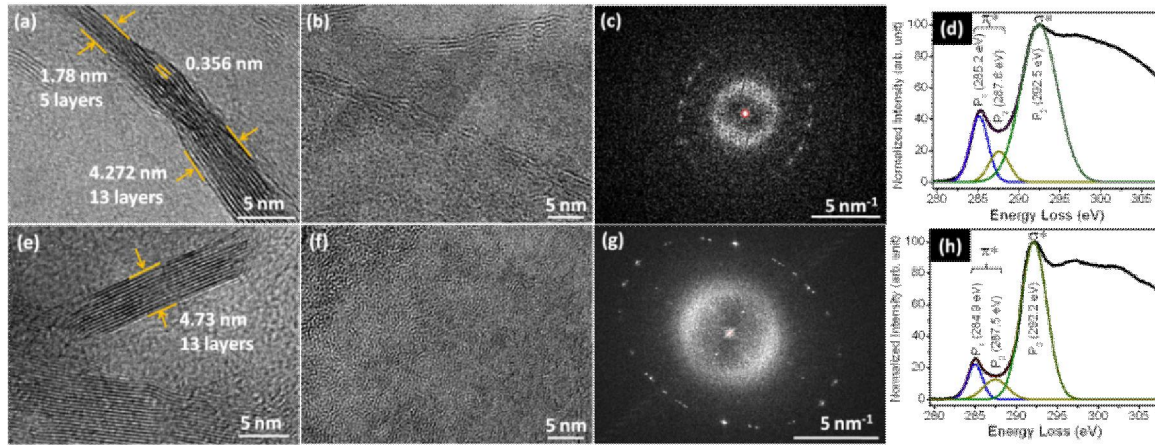


Figure 3.10: (a) and (b) HRTEM micrographs, (c) Fast Fourier transform (FFT) of (b) and (d) EELS of the sample grown with the composition of 1:7:0. (e) and (f) HRTEM image, (g) FFT of (b) and (d) EELS of the sample grown with the composition of 1:0:5.

Figures 3.10(d) and 3.10(h) represent the electron energy loss spectroscopy (EELS) of the film grown under 1:7:0 and 1:0:5, respectively in the region 280 – 310 eV. To quantify  $sp^2$  or  $sp^3$  fractions in the carbon system from EELS data, the C absorption K-edge is fitted with three Gaussian peaks after background subtraction and multiple scattering corrections. The first two peaks at 285 eV and intermediate around 287.6 eV originate due to the transition from the  $1s$  to the unoccupied  $\Pi^*$  states. The third peak at 292 eV represents the transition from the  $1s$  to the unoccupied  $\sigma^*$  states.<sup>28</sup> The quantification of  $sp^2$  and  $sp^3$  fraction is performed by following equations:

$$R_{gr} = \frac{Area(P_1+P_2)}{Area(P_1+P_2+P_3)} \quad (1.9); \quad R_{sample} = (1-x)R_{gr} \quad (1.10)$$

where,  $R_{gr}$  is the ratio of integral of  $P_1$  and  $P_2$  to total integral of functions of graphite, set as a material with 100%  $sp^2$  bonding. The  $x$  represents  $sp^3$  fraction for the probed volume of the sample. The  $sp^2$  fraction is found to be 74.2% and 60.7% for the film grown at 1:7:0 and 1:0:5 respectively. The  $sp$  contribution being low, is neglected for this study as  $x > 0.1$ .<sup>28</sup>

### 3.3.3 Raman spectroscopic analysis

The sample grown without any dilution gas (curve no. –1:0:0 in Fig. 3.11(a)), exhibits a complete overlap of G and D' bands, and the observed higher FWHM of the G' band ( $\sim 109 \text{ cm}^{-1}$ ) indicates high defect concentration in this sample. As seen in case I, the addition of Ar in CH<sub>4</sub> leads to a continuous decrease in D' band intensity and makes it appear as a shoulder in the G band [Fig. 3.11(a)] as well as the FWHM of the D, G and G' bands decrease monotonically (Table 3.5). This indicates a reduction of defects upon increasing the Ar content. Further, the case III(a) also exhibits a similar trend in terms of defects as evidenced from Fig. 3.11(c). On the other hand, for case III(b), no systematic variation is observed when a constant volume of H<sub>2</sub> is added along with Ar. Figure 3.11(b) shows the Raman spectra for the samples grown with the dilution of CH<sub>4</sub> with H<sub>2</sub> which is assigned as in case II. The FWHM of the D, G and G' bands decrease monotonically with H<sub>2</sub> dilution as shown in Table 3.5 except for at higher H<sub>2</sub> concentrations (1:0:  $\geq 5$ ). Also, it is clearly shown that there is a decrease in disorder, evidenced by the splitting of G and D' bands in contrast to the film grown without dilution. However, the defect density is found to still be larger than for case I. On the other hand, in the case of III(b) as shown in Fig. 3.11(d), the defect density is reduced further when Ar is introduced which is also evident from Table 3.5. Figure 3.11(e) shows the Raman spectra for samples grown at increasing concentrations of CH<sub>4</sub> with a fixed Ar and H<sub>2</sub> content. The D' band intensity decreases continuously with CH<sub>4</sub> and appears as a small hump in the G band. This can also be seen in Table 3.5 as a continuous decrease in the FWHM of the D and G bands, implying a decrease in defect intensity with increasing CH<sub>4</sub> concentration with fixed Ar and H<sub>2</sub> content. Further, except for a CH<sub>4</sub>:Ar:H<sub>2</sub> ratio of 5:3:1, the samples grown under feedstock compositions of 1:3:0, 1:0:3, 1:3:1 and 1:1:3 are found to possess lower defects in

comparison to the other compositions as indicated in Table 3.5. Thus, it may be inferred that the dilution of CH<sub>4</sub> with about 75% of Ar or H<sub>2</sub> is optimal to achieve lower defect concentrations in their respective morphology. However, the I<sub>D</sub>/I<sub>G</sub> ratio is not consistent with the FWHM of the Raman bands for the studied materials. The vertical structures have more edges whereas the planar structures have more grain boundaries. Hence, the relatively large D-band intensity in both cases is due to the combination of different types of defects such as stacking fault, hydrogenation, edges, grain boundaries, structural defects from various types of point defects and adsorbed functional groups. In such scenarios where more than two defects contribute, quantification of each of them is very complex and the extraction of individual contributions by different types of defects to the Raman band is difficult. Apart from this, the strain in the films is also known to contribute to the changes in the FWHM and the I<sub>D</sub>/I<sub>G</sub> ratio.<sup>29</sup> The line shape, width and position of the G' band can be used to probe the number of layers, their structural defects and doping.<sup>30</sup> Figure 3.11(f) shows the Raman spectra of the G' band for a few selected films and fitted with single Lorentzian peak and compared with that of HOPG. The films grown under different compositions also show a turbostratic stacking fault since the G' band could be fitted with a single Lorentzian profile for all the samples.<sup>31</sup> This supports the observation by HRTEM analysis as discussed earlier. The FWHM values, varying from 69.8 to 88.4 cm<sup>-1</sup> for these samples, indicate that these samples contain more than five layers of graphene.<sup>30</sup> On the contrary, the G' band of the multilayer HOPG film is composed of G'<sub>3DA</sub> and G'<sub>3DB</sub> bands as shown in Fig. 3.11(f). The position of the G' band of NGS with respect to G'<sub>3DA</sub> band of the HOPG, is also blue shifted indicating the presence of a few layer graphene.

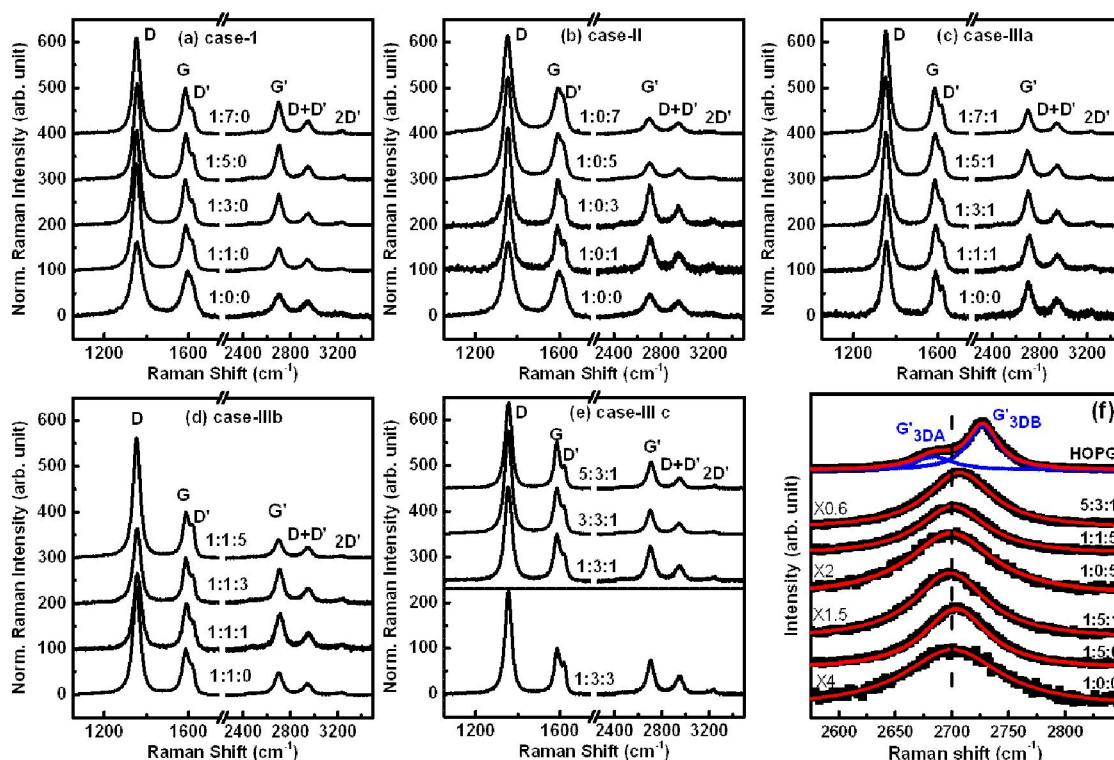


Figure 3.11: Raman spectra of NGS grown at different conditions by diluting (a)  $\text{CH}_4$  with increasing Ar [case I], (b)  $\text{CH}_4$  with increasing  $\text{H}_2$  [case II] (c)  $\text{CH}_4+5$  sccm of  $\text{H}_2$  with increasing Ar [case IIIa] (d)  $\text{CH}_4+5$  sccm of Ar with increasing  $\text{H}_2$  [case IIIb] and (e) increasing  $\text{CH}_4$  concentration with fixed Ar and  $\text{H}_2$  ratio [case IIIc]. Raman spectra are normalized with G band intensity of the respective curve and linearly shifted in the y-axis for clarity. The actual flow rates in sccm are given in the plots. (f) A Lorentzian fit (solid line) of G' band of NGS grown with different feedstock gas compositions along with highly oriented pyrolytic graphene.

The planar structures, that are grown under hydrogen dominant feedstock compositions, exhibit an up shift in G band frequency (up to  $\sim 1593 \text{ cm}^{-1}$ ) when compared to the vertical structures as shown in Table 3.5. The up shift in G band frequency can be attributed to substrate induced doping whereas free standing vertical graphene has less influence from substrates and hence a downshift in G band frequency is observed. The  $I_{\text{G}}/I_{\text{G}}$  ratio is also decreased for the FPNG in comparison to the vertical structures. These results are consistent with the influence of the substrate on the Raman spectroscopy of the

graphene surface.<sup>32</sup> However, the present Raman studies reveal that the defect density can be reduced by choosing an optimal composition of feed gases.

Table 3.5: Extracted parameters from Raman analysis for different NGS. The topography of the nanostructures are classified as isolated nanoclusters (I.N), vertical (V) and planar (P) structures as given in morphology column. The symbol ‘ \* ’ in column ‘*h*’ represents thickness measured by AFM and others values are measured by FESEM and *d* represents a discontinuous film.

CH <sub>4</sub> : Ar:H <sub>2</sub>	Dilution (%)	Topo- graphy	<i>h</i> nm	Peak Position (cm <sup>-1</sup> )			FWHM (cm <sup>-1</sup> )		
				D	G	G'	D	G	G'
<i>Case I dilution of CH<sub>4</sub> with Ar</i>									
1:0:0	0	I.N	12*	1355.4	1592.4	2703.5	57.9	57.3	109
1:1:0	50	V	28	1353.8	1587.5	2702.2	41.6	41.5	76.8
1:3:0	75	V	81	1353.9	1584.7	2702.4	39.6	34.8	65.9
1:5:0	86	V	137	1355.9	1586.7	2704.1	39.7	36.7	69.9
1:7:0	88	V	165	1353.1	1584.2	2701.5	39.3	36.1	68.6
<i>Case II dilution of CH<sub>4</sub> with H<sub>2</sub></i>									
1:0:0	0	I.N	12*	1355.4	1592.4	2703.5	57.9	57.3	109
1:0:1	50	P	4.7*	1356.2	1590.1	2707.2	43.2	35.5	77.1
1:0:3	75	P	5.2*	1354.5	1590.7	2705.2	37.7	34.9	69.8
1:0:5	83	P	4.3*	1354.2	1590.2	2702.9	46.8	45.2	88.4
1:0:7	88	I.N.	- <i>d</i> -	1352.7	1593.0	2699.2	48.6	50.4	94.5
<i>Case IIIa dilution of CH<sub>4</sub>/H<sub>2</sub> with Ar</i>									
1:0:1	50	I.N	4.7*	1356.2	1590.1	2707.2	43.2	35.5	77.1
1:1:1	67	I.N	<10	1354.2	1587.9	2701.3	41.8	40.5	75.4
1:3:1	80	V	118	1355.0	1585.9	2703.9	41.4	37.1	73.3
1:5:1	86	V	148	1352.8	1586.4	2698.9	43.2	42.8	79.4
1:7:1	89	V	160	1352.7	1585.1	2699.8	41.7	38.2	74.3
<i>Case IIIb. dilution of CH<sub>4</sub>/Ar with H<sub>2</sub></i>									
1:1:0	50	P	28	1353.8	1587.5	2702.2	41.6	41.5	76.8
1:1:1	67	P	<10	1354.2	1587.9	2701.3	41.8	40.5	75.4
1:1:3	80	P	-do-	1355.8	1588.0	2708.7	41.0	34.2	72.5
1:1:5	86	P	-do-	1353.6	1588.8	2701.2	39.0	37.0	75.2
<i>Case IIIc. increase of CH<sub>4</sub> concentration with fixed Ar and H<sub>2</sub></i>									
1:3:1	80	V	118	1355.0	1585.9	2703.9	41.4	37.1	73.3
3:3:1	57	I.N	72	1353.9	1585.5	2702.1	39.0	35.8	64.6
5:3:1	44	P	18	1355.3	1584.8	2707.4	38.2	29.3	69.7

### 3.4 Temperature dependent growth

The early stage nucleation and growth of VGN is investigated by changing the substrate temperature from 600 to 800°C under CH<sub>4</sub>/Ar gas environment, while other parameters are fixed and listed in Table 3.6. After deposition, the substrates are annealed at the growth temperature for 30 min and taken out after cooling down at room temperature.

Table 3.6 Experimental parameters for temperature dependent growth of VGN

CH <sub>4</sub> /Ar flow (sccm)	Growth time (min)	Microwave power (W)	Chamber pressure (mbar)	Growth temperature (°C)
5/25	30	400	1×10 <sup>-3</sup>	600-800

#### 3.4.1 FESEM analysis

Figures 3.12(a-f) represent the morphology of the films grown under various substrate temperatures. It is seen that an increase in substrate temperature leads to growth of VGN from the NG. No NGS could be grown at below 600 °C in this study as etching of graphene by hydrogen species dominates.<sup>33</sup> It can be seen from Fig. 3.12(a) that the continuous NG island can be grown at 600 °C and the higher magnified image of VGN is shown in inset of Fig. 3.12(a). The height of NG film is found to be 17.72 (±1.64) nm, with average NG island size of 28.62 (±17.41) nm and island density of 925(±161.37)/ μm<sup>2</sup>. The films are found to be electrically continuous with the sheet resistance of 5.6 kΩ/□. Such growth directly on insulating substrate at low temperature without post-growth treatment offers a good compatibility with the semiconductor processing technological advances. As temperature increases to 625 °C, the 2D structure gets transformed to 3D structure by growth of vertical sheets on the NG layer. At 625 °C, the grain boundary of nanoislands act as nucleation sites for vertical growth with the help of inherent localized electric field due

to plasma and thermophoretic force induced by a temperature gradient in the plasma [Fig. 3.12(b)]. As shown in Fig.3.12(c), the vertical sheets of height of  $37.45(\pm 8.94)$  nm are observed on the NG layer of thickness of  $11.69(\pm 1.97)$  nm. Hence, it is inferred that the height of NG layer decreases with respect to the growth temperature. In addition, the average size of island on the NG layer is found to be  $40.41(\pm 18.26)$  nm with density of  $768.75 (\pm 68.84)/\mu\text{m}^2$ . Further increase of temperature to  $650^\circ\text{C}$  [Fig. 3.12(d)] led to more number of vertical sheets as compared to previous sample and forms a sheet-like structure with the higher growth rate, as shown in Fig. 3.12(e). In addition, the sheets started to interlace together and the spacing between the vertical sheets while maintaining the sheet like features at  $800^\circ\text{C}$  [Fig. 3.12(f)]. Figure 3.12(g) shows the variation of growth rate with respect to the growth temperature. It is seen that the variation of growth rate vs growth temperature follow the Arrhenius equation and from this the activation energy is calculated. The activation energy is found to be 0.57 eV. Thornton *et al.*<sup>34</sup> observed that the substrate temperature did not affect the plasma density and composition significantly. Hence, this result is only due to the increased mobility of surface atoms such that adsorption rate and chemical surface reaction becomes higher at high temperature which minimizes the surface energy of the substrate. Therefore the migration of energetic plasma species reaching towards the substrate and adsorption rates become higher at higher growth temperature.<sup>35</sup> Such substrate temperature dependent growth is also seen in time dependent growth of VGN (Sec. 3.2.1). As growth time increases, the continuous NG island transforms into the VGN.

The water contact angle (CA) of the surface at ambient environment with growth temperature is shown in Fig. 3.12(h). The result reveals that depending on the morphology, hydrophilic surface with CA of  $80.3^\circ$  (sample grown at  $600^\circ\text{C}$ ) transforms into the near

superhydrophobic with CA 131.5° (sample grown at 800 °C).

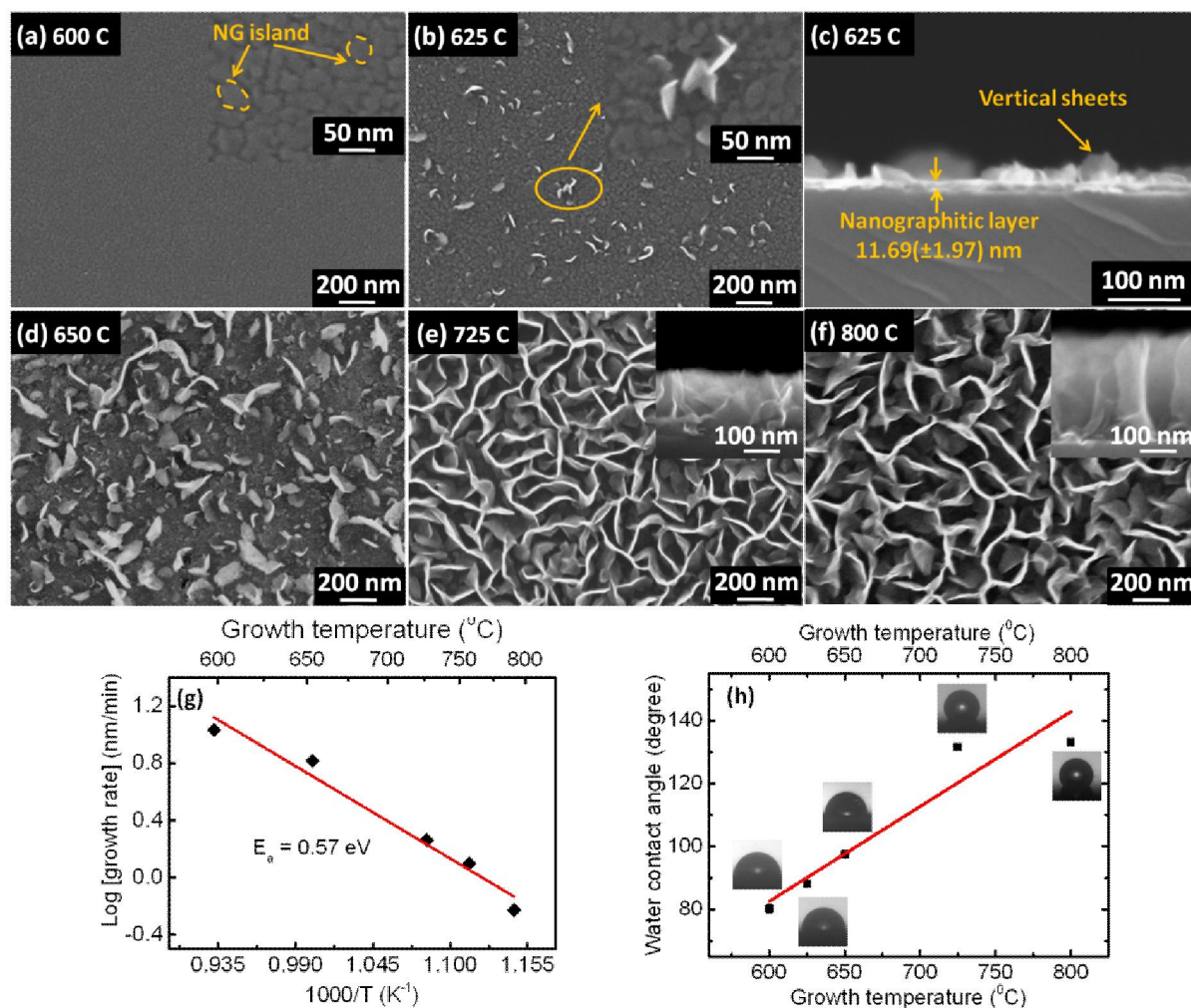


Figure 3.12: FESEM micrograph of VGN grown at (a) 600 °C, (b) 625 °C, (c) 625 °C (cross section image), (d) 650 °C, (e) 725 °C, and (f) 800 °C, (g) Arrhenius plot of growth rate vs inverse substrate temperature, (h) Water contact angle versus growth temperature of VGN

### 3.4.2 Raman spectroscopic analysis

Figure 3.13(a) represents the vertically stacked Raman spectra of plasma grown samples at various temperatures. It is observed that the D'-band intensity increases and starts to decrease, as growth temperature increases from 625 °C to 800 °C, while G'-band intensity behaves inversely. Similar result is observed for the FWHM of D, G and G'-bands, position of G-band and  $I_D/I_G$ . All these parameters increase as growth temperature

increases to 625 °C and then decreases with increasing temperature from 625 °C to 800 °C [Figs. 3.13(b) and 3.13(c)]. This result suggests the transformation of structure and found to be in good agreement with observations made from FESEM studies [Fig. 3.12]. At 625 °C the edges of vertical sheets started to form thus increasing defects in the structure; whereas further increase in temperature resulted in better degree of graphitization. In addition, the  $I_D/I_G$  is also found to be minimum for the sample grown at 800 °C.

This observation concludes that the higher growth temperature provides more migration energy/driving force to hydrocarbon species towards the substrate surface and higher deposition rate with better crystalline structure.

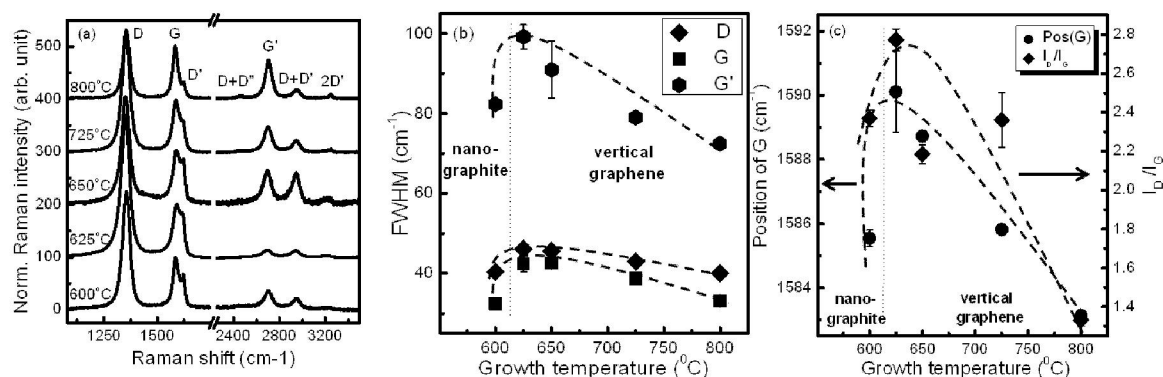


Figure 3.13: (a) Raman spectra of temperature dependent growth of VGN, (b) FWHM of D, G, G') and (c) position of G band and  $I_D/I_G$  vs growth temperature.

### 3.5 Discussion

From the sequence of observations made from FESEM studies, it is recorded that NGS structure transform into VGN while increasing the growth time and growth temperature and dilution of CH<sub>4</sub> with Ar. Based on the above experimental results, a phenomenological four stage growth model is proposed and the graphical representation of nucleation and

growth mechanism of VGN is shown in Fig. 3.14. The different stages of the nucleation and growth model are as follows:

- (i) First stage [Fig. 3.14(a)]: during pre-cleaning process, the Ar plasma removes surface contaminations and creates localized hot spots<sup>36</sup> on substrate surface at higher temperature. The nature (size, shape and density) of hot spots depends on several factors like substrate temperature, nature of substrate and plasma environment. These localized hot spots are the energetically most favorable regions to adsorb and acts as nucleation sites to hydrocarbon species.
  
- (ii) Second stage [Fig. 3.14(b)]: when CH<sub>4</sub> is fed into the growth chamber, MW energy in ECR-CVD creates a high density plasma with a variety of species such as C<sub>x</sub>H<sub>y</sub>, C<sub>2</sub>, CH, CH<sup>+</sup>, H, H<sup>+</sup>, H\*, Ar-H and their several possible combinations through dissociation and recombination of CH<sub>4</sub> with Ar.<sup>37</sup> The early stage of nucleation is based on direct adsorption of carbon and hydrocarbon onto the hot spots due to surface diffusion, initiating rapid nucleation of NGS. The sticking co-efficient of radicals depends on the nature of the substrate<sup>38</sup>, localized hot spot size and plasma process parameters (gas pressure, growth temperature, pressure, molar heat conductivity of gas). Thus the size, shape and density of NG islands depend on the characteristics of localized hot spots.
  
- (iii) Third stage [Fig. 3.14(c)]: the NG islands coalesce and form interfacial NG base layer or FPNG over the substrates. The interfacial base layer contains highly defective NG, *a*-C, carbon onions and point defects such as pentagon, heptagon rings. Zhao *et al.*<sup>26</sup>

reported that the nucleation of vertical growth could start either from the buffer layer or from the surface carbon anions.

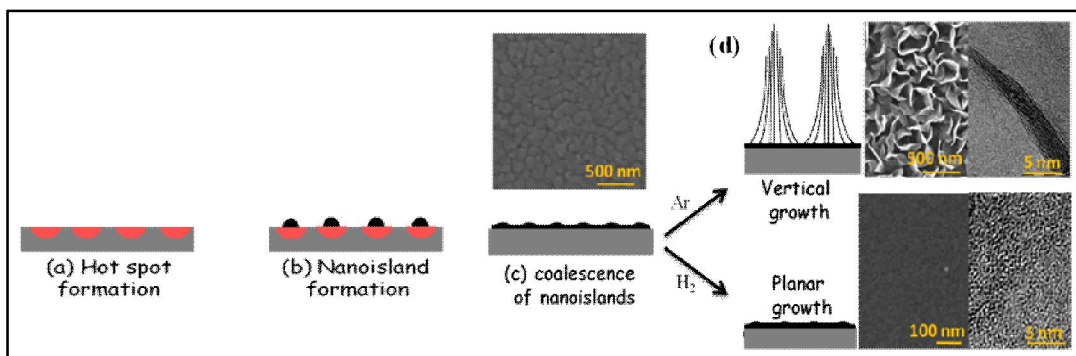


Figure 3.14: A phenomenological four stage growth model of VGN

(iv) Final stage [Fig. 3.14(d)]: coalescence of NG-islands and continuing growth causes stress at NG grain boundaries. Release of the stress favors nucleation and further growth of graphene nanosheets in the vertical direction.<sup>39</sup> In addition, the vertical growth is found to be influenced by the in-built electric field associated with the plasma.<sup>25</sup> Further, the plasma produces a relatively higher temperature and chemical potential gradients near the substrate surface enhancing the vertical growth. The feedstock gas composition then decides whether the growth of a vertical structure is continued or etched out. If the plasma was consisted of a relatively higher concentration of Ar, it would favor the continued growth of vertical layers. On the other hand, if the erosion is high due to the presence of excess H<sub>2</sub> concentration, it leads to the growth of FPNG films. Hence, further increase in carbon adatoms to the growing film and carbon diffusion takes place in the planar regions as well as the vertically growing graphene nanosheets. However, the carbon atoms diffusing to the edge of vertical graphene binds well due to strong in-plane C–C covalent bond and grow normal to the substrate. Whereas, the carbon species arriving at

planer region are re-evaporated because of the weak van der Waals force between the graphene layers.<sup>40</sup> These simultaneous growth and etching processes make the VGN to increase the height and decrease the number density with growth time.

### 3.6 Summary

The vertical graphene nanosheets (VGN) are grown on SiO<sub>2</sub>/Si substrate using electron cyclotron resonance chemical vapor deposition (ECR-CVD) technique. The morphology, growth rates and degree of graphitization of VGN are found to depend on the growth time, feedstock gas composition and growth temperature. The outcome of the present Chapter is as follows:

- Nanographitic structure is transformed into vertically oriented open three-dimensional interconnected network.
- Time dependent growth reveals the disorder induced growth mechanism through amorphization trajectory model by Ferrari-Robertson.
- A ternary field diagram on growth is established.
- The nucleation and growth mechanism of VGN is explained with a four stage phenomenological model invoking substrate–plasma interaction.

### 3.7 References

1. Ferrari, A., and Robertson, J., *Phys. Rev. B* (2000) **61** (20), 14095
2. Malard, L., *et al.*, *Phys. Rep.* (2009) **473** (5), 51
3. Ferrari, A. C., and Basko, D. M., *Nat. Nanotechnol.* (2013) **8** (4), 235
4. Karlin, S., and Colomban, P., *J. Raman. Spectrosc.* (1997) **28** (4), 219
5. Casiraghi, C., *phys. status solidi RRL* (2009) **3** (6), 175
6. Quinlan, R. A., *et al.*, *Carbon* (2013) **64**, 92
7. Ferreira, E. M., *et al.*, *Phys. Rev. B* (2010) **82** (12), 125429
8. Cançado, L. G., *et al.*, *Nano Lett.* (2011) **11** (8), 3190
9. Lucchese, M. M., *et al.*, *Carbon* (2010) **48** (5), 1592
10. Jorio, A., *et al.*, *Phys. Status Solidi B* (2010) **247** (11-12), 2980
11. Venezuela, P., *et al.*, *Phys. Rev. B* (2011) **84** (3), 035433
12. Eckmann, A., *et al.*, *Nano Lett.* (2012) **12** (8), 3925
13. Peltekis, N., *et al.*, *Carbon* (2012) **50** (2), 395
14. Cheung, T., *J. Appl. Phys.* (1982) **53** (10), 6857
15. Shang, N. G., *et al.*, *Adv. Funct. Mater.* (2008) **18** (21), 3506
16. Nikitin, A., *et al.*, *Surf Sci.* (2008) **602** (14), 2575
17. Medina, H., *et al.*, *Adv. Funct. Mater.* (2012) **22** (10), 2123
18. Dischler, B., *et al.*, *Solid State Commun.* (1983) **48** (2), 105
19. Malesevic, A., *et al.*, *Nanotechnology* (2008) **19** (30), 305604
20. Barinov, A., *et al.*, *Phys. Rev. Lett.* (2007) **99** (4), 046803
21. Vizireanu, S., *et al.*, *Surf. Coat. Technol.* (2012) **211**, 2
22. Cheng, C., and Teii, K., *IEEE Trans. Plasma Sci.* (2012) **40** (7), 1783
23. Jain, H. G., *et al.*, *Carbon* (2011) **49** (15), 4987

24. Hiramatsu, M., and Hori, M., *Carbon nanowalls: synthesis and emerging applications*. Springer: 2010
25. Wu, Y., *et al.*, *Adv. Mater.* (2002) **14** (1), 64
26. Zhao, J., *et al.*, *Nano Lett.* (2014) **14** (6), 3064
27. Pimenta, M., *et al.*, *Phys. Chem. Chem. Phys.* (2007) **9** (11), 1276
28. Hamon, A.-L., *et al.*, *J. Mater. Chem.* (2004) **14** (13), 2030
29. Mohiuddin, T., *et al.*, *Phys. Rev. B* (2009) **79** (20), 205433
30. Hao, Y., *et al.*, *small* (2010) **6** (2), 195
31. French, B., *et al.*, *Thin Solid Films* (2006) **494** (1), 105
32. Huang, C.-H., *et al.*, *Nanoscale Res. Lett.* (2014) **9** (1), 1
33. Liu, D., *et al.*, *Carbon* (2014) **72**, 387
34. Thornton, J. D., *Carbon Nanowalls: Processing, Structure and Electrochemical Properties*. Ph.D., North Carolina State University 2011
35. Wang, F.-J., *et al.*, *Appl. Surf. Sci.* (2015) **355**, 218
36. Ostrikov, K. K., *et al.*, *Nanoscale* (2010) **2** (10), 2012
37. Muñoz, R., and Gómez-Aleixandre, C., *J. Phys. D: Appl. Phys.* (2014) **47** (4), 045305
38. Ostrikov, K., *et al.*, *Adv. Phys.* (2013) **62** (2), 113
39. Yoshimura, A., *et al.*, *Carbon* (2012) **50** (8), 2698
40. Zhu, M., *et al.*, *Carbon* (2007) **45** (11), 2229



# 4

## **Tuning Morphology of Vertical Graphene Nanosheets and Study of its Thermal Stability**

*We must never make experiments to confirm our ideas, but simply to control them*  
– Claude Bernard

The emerging demand for the potential application of the materials should be compatible with current technology, which needs the uniform, homogeneous and thermally stable materials with desired morphology and higher growth rate over the large area substrate. Hence, this chapter describes the possibility of tuning morphology of vertical graphene nanosheets (VGN) with higher growth rate on various substrates. The variable parameters are microwave power, distance between plasma source to substrate and substrates in plasma enhanced chemical vapor deposition chamber. The homogeneity, uniformity and thermal stability of VGN are also investigated.

## 4.1 Introduction

The precise use of materials in industrial scale is one of the most important objective of the research. However, implementation of vertical graphene nanosheets (VGN) in industrial scale relies on several factors, namely, growth over large area, uniformity and homogeneity of growth, growth rate, possibility of use of different substrates of choice, and their stability under thermal processing. VGN has already shown its promise towards potential application in various fields (discussed in Section 1.3.2), but its realization is necessary. Towards this, the following aspects are addressed in this Chapter:

- (i) tuning the morphology, growth rate and structural quality of VGN,
- (ii) film uniformity and homogeneity over the deposition area,
- (iii) possibility to grow VGN on any arbitrary substrate and its role, and
- (iv) thermal stability of the material.

The morphology, structural quality and growth rate can be controlled by tuning the amount and nature of plasma species in terms of radical density and energy of ions which depend on the plasma power, position of substrate in the plasma plume and feedstock gas composition at a constant substrate temperature. The effect of feedstock gas composition has already been discussed in Section 3.3. Hence, this Chapter deals with the effect of plasma process parameters of microwave (MW) power and distance from plasma source to substrate (for sake of simplicity, referred as distance) on the final structure of VGN. The primary advantages for PECVD is the possibility to grow directly on any desired substrate. Hence, the growth is carried out on a wide range of substrates to understand the role of the substrate on growth and final morphology. Finally, thermal stability is one of the desired characteristics for using them in device. Hence, a time dependent high temperature annealing study of VGN is performed and discussed here.

## 4.2 Effect of radical plasma density

The radical plasma density across the substrate surface in the ECR-CVD chamber can be varied by changing the following parameters, namely, MW power and distance. The deposition parameters are tabulated in Table 4.1. The experimental method is discussed in Section 3.2.

Table 4.1: Experimental parameters to tune radical plasma density for VGN growth

Constant growth parameters	Case-I	Case-II
CH <sub>4</sub> /Ar : 5/25 (sccm)	MW power: 200-475 W	Distance from plasma source to substrate:
Growth temperature: 800°C	at a constant distance	40-10 cm at constant
Growth time : 30 min	of 30 cm from plasma	MW power of 375 W
Chamber Pressure: $1.5 \times 10^{-3}$ mbar	source to substrate	

### 4.2.1 Influence of microwave power

The panels (a)-(f) in Fig. 4.1 reveal the spatial distribution of vertical sheets and Fig. 4.1(g) shows the plot of growth rate vs MW power. These results emphasize that the growth rate and areal density of VGN can be controlled by changing the MW power from 200 W to 475 W. Interestingly, a higher growth rate is found for the sample grown at 375 W [circled point in Fig. 4.1(a)], while other parameters remain same. Increasing power beyond 375 W is found to reduce the growth rates [Fig. 4.1(g)]. Although the height of VGN decreases, the lateral length increases due to continuous availability of hydrocarbon radical and a better uniformity along the width is observed at high density plasma.<sup>1</sup> Raman spectra of VGN grown under different MW power [Fig. 4.1(h)] indicate a decrease in D' intensity with increasing MW power. No significant variations are observed in FWHM of D, G and G' bands. Figure 4.1(h) shows the variation in  $I_D/I_G$  with respect to MW power.

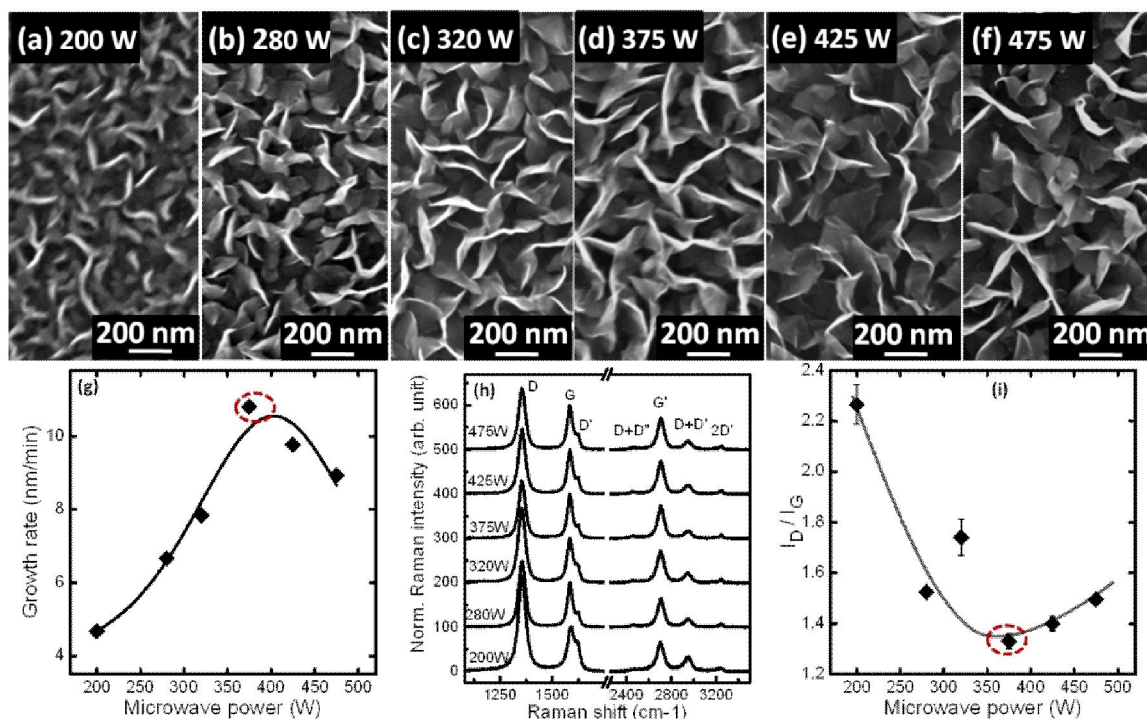


Figure 4.1: FESEM micrographs of VGN grown at MW power of (a) 200 W, (b) 250 W, (c) 320 W, (d) 375 W, (e) 425 W and (f) 475 W; (g) variation of growth rate, (h) stack of Raman spectra and (i)  $I_D/I_G$  of VGN with respect to MW power.

An intriguing observation is that the variation of growth rate and  $I_D/I_G$  shows a similar but opposite trend with MW power [Fig. 6(g)].

#### 4.2.2 Influence of distance from plasma source to substrate

Figures 4.2(a-d) depict the morphology of VGN deposited at different distances. It is observed that the number density of vertical sheets decreases with decreasing the distance. Meanwhile, length, height of the sheets and spacing between sheets are increases with decreasing the distance. In addition, the growth rates are found to increase from 5 to 25.5 nm/min as the distance is decreased from 40 cm to 10 cm [Fig. 4.2(e)]. Raman spectra of these VGN samples are shown in Fig. 4.2(f). A systematic decrease in the  $D'$  intensity with distance is clearly seen. Smaller FWHM of D, G and  $G'$  bands is observed at lower

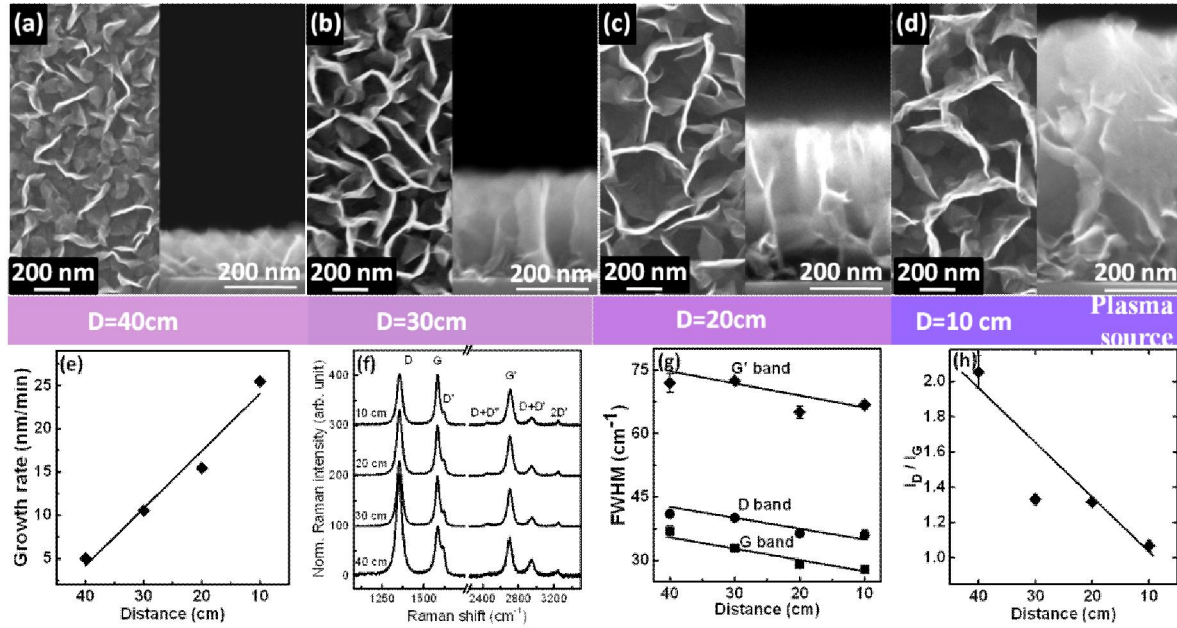


Figure 4.2: FESEM micrographs of VGN grown at a distance from plasma source of (a) 40 cm, (b) 30 cm, (c) 20 cm, and (d) 10 cm; (e) variation of growth rate, (f) stack of Raman spectra, (g) variation in FWHM of D, G and G' band, (h) variation in  $I_D/I_G$  of VGN with respect to distance.

distance [Figure 4.2(g)]. The lowest FWHM of G band is found to be  $27.9 \text{ cm}^{-1}$  for the sample grown at a distance of 10 cm. The  $I_D/I_G$  decreases i.e. crystalline size increases with decreasing distance, as shown in Fig. 4.2(h). This implies that the structural quality can be significantly improved by growing at close distance.

### 4.2.3 Discussion

The increase in plasma power and decrease in distance enhances the decomposition rate, density, momentum and temperature of ions, electrons and neutral species. Although the substrates temperature is maintained at  $800 \text{ }^\circ\text{C}$  in this study, plasma too heats the substrate influencing the local electric field intensity.<sup>2,3</sup>

As plasma power is increased and distance is decreased, the surface adatom mobility

increases and electrons move faster towards the substrate. Hence, the surface is covered by a *quasi stationary electron film*.<sup>4</sup> This negatively charged surface makes stronger electric field to attract the ion with higher acceleration. It should be noted that the growth of VGN is determined by the competition between deposition rate of carbon species and etching rate of carbon species by nascent H produced in plasma. In addition, the hydrogen species under plasma plays important role during the NG structure growth by PECVD as: (i) defining the morphology and graphitization, thus enhancing the quality of the structure, (ii) reducing the amount of C<sub>2</sub> species by recombination and (iii) etching the *sp*<sup>2</sup>-C, *sp*<sup>3</sup>-C and *a*-C at different rates. Thus the initial increase in growth rate and crystalline size with MW power can be attributed to increased availability of C<sub>2</sub> radicals towards the substrate and optimum C/H ratio. At higher power (>375 W), the amount and energy of hydrogen species also increase which in addition to reducing the C<sub>2</sub> radical density as well as etches out carbon species as well. This results in the decreased growth rate and reduced crystallinity. Hence, in this present study the 375 W is found to be optimum plasma power for VGN growth with highest growth rate and crystallite size.

At higher distance (40 cm), time of transport of carbon radicals (mainly C<sub>2</sub>) is high as well they will decay and form other species by recombining with each other. This leads to reduced radical density and ion energy of plasma species at the higher distance. Whereas, at closer distance, the ion density and ion energy of plasma species are very high and ions can reach the substrate without undergoing significant recombination. As a result, the growth rate is high for the substrate placed at 10 cm below the plasma source.

Through systematic study, it is found that plasma power and distance are the critical factors to define nature of plasma species, surface reaction kinetics and growth dynamics. They governed the final structure and controlled morphology of VGN.

### 4.3 Homogeneity and uniformity of vertical graphene nanosheets

The VGN is grown over 2.5 inch diameter Cu substrate to verify their homogeneity and uniformity across the substrate surface. The growth parameters are listed in Table 4.2.

Table 4.2: Experimental parameters for VGN on Cu substrate

CH <sub>4</sub> /Ar/H <sub>2</sub> (sccm)	Growth temperature	Growth time	Chamber Pressure	MW power	distance from plasma source to substrate
15/15/5	800°C	30 min	$1.5 \times 10^{-3}$ mbar	375 W	40 cm

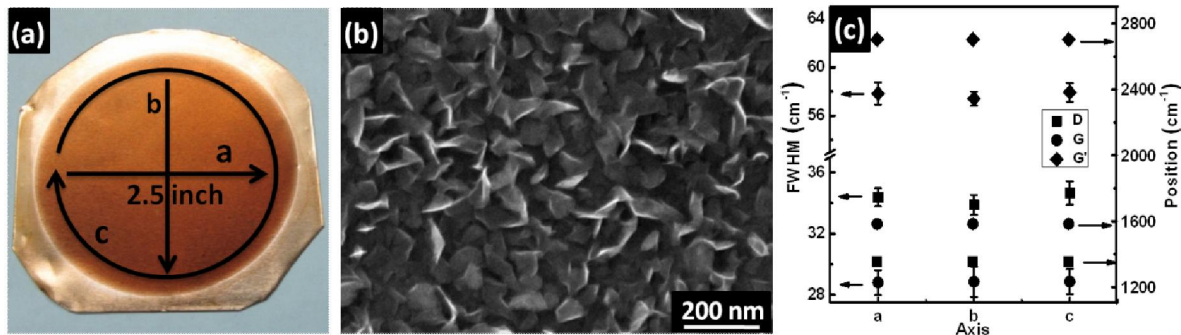


Figure 4.3: (a) Optical image of VGN grown on Cu substrate, (b) SEM micrographs of VGN (c) variation in FWHM and peak position of D-, G and G'-peak with respect to the axes (a, b and c)

Figures 4.3(a) and (b) shows the optical image and a typical FESEM micrographs of VGN. The FESEM micrographs at several places of the film confirm its homogeneity. The Raman spectra of VGN are taken along a-axis, b-axis and c-axis, as shown in Figs 4.3 (a). The extracted parameters such as peak position and FWHM of D, G and G' bands along the three axes are plotted in Fig.4.3(c). As shown in Fig. 4.3(c), no significant variation is observed in the position and FWHM of D, G and G' bands. This confirms that the film grown over 2.5 inch diameter is very uniform and homogeneous. This result ensured that a number of substrates of choice can be placed across an area of 2.5 inch diameter and VGN can be grown simultaneously on them. This is carried out to verify the

role of substrate on the growth kinetics and morphology, while all substrates are exposed to identical condition.

#### 4.4 Effect of substrates

The VGN are grown on different substrates ranging from metallic to insulators, such as Pt foil (125  $\mu\text{m}$ ), Ni foil (125  $\mu\text{m}$ ), Cu foil (125  $\mu\text{m}$ ), Au/Si(100), Si(111), Si(100), SiO<sub>2</sub> and quartz. The experimental details are mentioned in Section 3.2. The experimental conditions are listed in Table 4.3

Table 4.3: Experimental parameters for VGN on different substrates

CH <sub>4</sub> /Ar (sccm)	Growth temperature	Growth time	Chamber Pressure	MW power	Distance from plasma source to substrate
5/25	800°C	30 min	1.5×10 <sup>-3</sup> mbar	375 W	40 cm

##### 4.4.1 FESEM analysis

The morphologies of VGN grown simultaneously over different substrates are depicted in Fig. 4.4. The as-grown VGN are observed to be homogeneous, uniform and densely packed, except for those grown on quartz. However, a discernible variation in morphology is observed for the VGN grown on different substrates. The morphology of VGN grown on Pt is found to be maze-like, whereas it is petal-like on other substrates. The cross sectional height of VGN on different substrates varies from 169 to 264 nm, shown as inset in respective FESEM images [Fig 4.4 (c), (d), (e) and (g)]. The aerial density of VGN is found to be highest for Pt and lowest for quartz. The difference in height and aerial density of VGN grown on these substrates indicate that the nucleation and growth rates are different for different substrates. The difference in height of VGN grown on Si(111) (201.2 nm) and Si(100) (214.5 nm) substrates indicates the anisotropic nature of the growth.

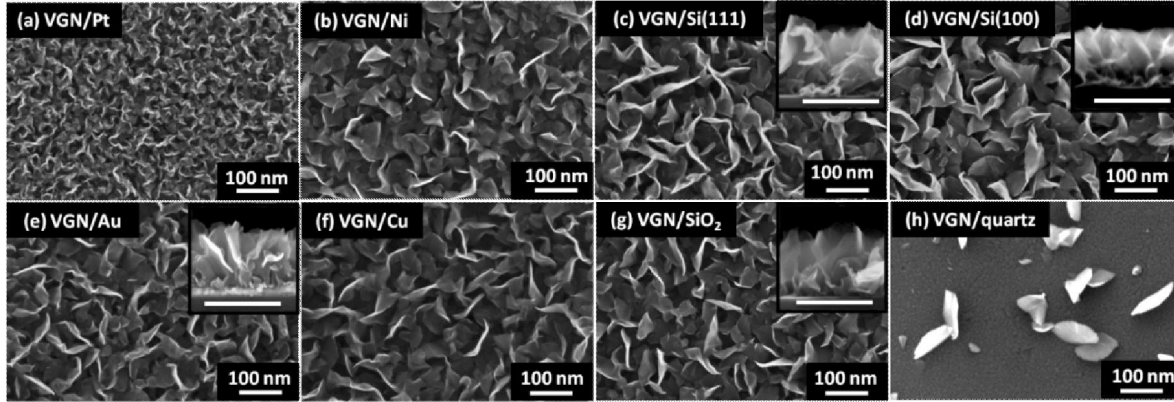


Figure 4.4: FESEM micrographs of VGN grown on (a) Pt, (b) Ni, (c) Si(111), (d) Si(100), (e) Au/Si, (f) Cu, (g) SiO<sub>2</sub>, and (h) quartz substrates

#### 4.4.2 Contact angle measurement

Table 4.4 shows water contact angle (CA) values measured over the substrate surfaces, before and after VGN growth. A representative image, depicting CA before and after growth of VGN on Si(100), is shown in Fig. 4.5. The pre-cleaned substrates exhibit CA less than 90° except for Cu indicating the hydrophilic nature. The Pt substrate shows the lowest CA of 62.9° and Cu shows the highest CA of 101.4°. The variation in CA can be attributed to the different surface energies of substrates. After the growth, VGN is found to be hydrophobic in nature. The VGN on Cu exhibits the highest hydrophobic behavior with CA of 136.6±0.2° while quartz shows the least hydrophobicity with CA of 105.9±3.7°. The difference in CA can be attributed to the variation in aerial density of VGN on the substrate. From the SEM micrographs, it is clear that aerial density of VGN on quartz is the least and it shows the lowest CA. The lower CA signifies higher surface energy. It should be noted that the surface energy of substrates can strongly influence the early stage nucleation of adatoms during thin film growth. A clear trend in aerial density of VGN with surface energy can be discerned from the SEM images, except in the case of quartz. The VGN on Pt with the highest surface energy has the highest aerial density followed by Ni.

The variation in aerial density is not much in the case of other substrates. Hence, surface energy is one of the factors affecting the nucleation density and hence the VGN morphology is different on various substrates. The lower area density of VGN on quartz may be due to substrate properties other than surface energy. The root mean square (*rms*) roughness measured over  $1 \times 1 \mu\text{m}^2$  area on different substrates is provided in Table 4.4. However, no significant correlation between roughness of pre-treated substrates and morphology of VGN is observed.

Table 4.4: Extracted parameter of contact angle measurement of different surfaces before and after growth of VGN, *rms* roughness of pre-cleaned substrates and their respective thermal conductivity from literatures

Substrates	Contact angle(CA) [Degree]		<i>rms</i> value nm	Thermal conductivity W/m-K
	Before growth	After growth		
Pt	62.9±3.2	121.9±0.9	2.0±0.5	71.9 <sup>5</sup>
Ni	71.7±4.1	123.1±2.8	2.5±1.9	93 <sup>5</sup>
Si(100)	72.8±0.7	135.2±0.9	0.4±0.1	133 <sup>6</sup>
Si(111)	76.5±1.4	133.7±0.1	0.4±0.1	156 <sup>7</sup>
Au	85.5±0.6	134.0±0.3	2.3±0.8	318 <sup>5</sup>
Cu	101.4±3.9	136.6±0.2	3.6±0.8	402 <sup>5</sup>
SiO <sub>2</sub>	79.1±2.4	131.6±0.2	0.4±0.1	1.29 <sup>6</sup>
quartz	75.3±0.8	105.9±3.7	0.5±0.1	1.5-3

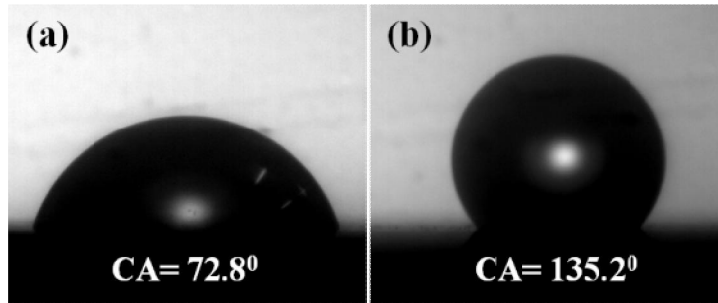


Figure 4.5: Water contact angle of Si(100) (a) before growth, and (b) after growth of VGN

### 4.4.3 Raman spectroscopic analysis

The Raman spectra of VGN grown on different substrates as shown in Fig. 4.6(a). The extracted parameters show differences in structural characteristics of VGN and are listed in Table 4.5. As shown in Fig. 4.6(a), the G and D' bands almost overlap for VGN grown on Pt which indicates presence of higher amount of defects. It is consistent with the observation made in the morphological studies that VGN on Pt substrate have higher areal density, more crumpled maze-like structure with higher sheet curvature than those for the samples grown on other substrates (Fig. 4.4). Similarly, the FWHM of D, G and G' bands of VGN on Pt are also higher than those for the samples grown on other substrates indicating presence of higher defects for samples grown on Pt (Table 4.4). The lowest FWHM of G-band ( $33.1 \text{ cm}^{-1}$ ) is found for VGN grown on quartz. Further, the position of G band on Pt is around  $1589 \text{ cm}^{-1}$  and for samples grown on all other substrates it is around  $1585 \text{ cm}^{-1}$ . Such variation in G-band position could be due to different levels of strain in VGN grown on different substrates.<sup>8</sup> The lattice mismatch between substrate and interfacial NG base layer or defects present can induce such strain.<sup>9</sup> Also, it is found that the  $I_D/I_G$  of VGN varies from 2.12 to 2.59 nm depending on the substrates, as given in the Table 4.5. Thus, the variation of parameters extracted from Raman spectra of VGN grown on different substrates is due to the variation in aerial density and degree of graphitization in the samples.

Furthermore, a closer view of Raman spectra shows that the valley between D and G bands is upshifted as shown in Fig. 4.6(b). The best fit for the first order Raman spectra is found to have two additional bands at about  $1140$  and  $1500 \text{ cm}^{-1}$  in addition to prominent D, G and D' bands. The peak at about  $1140 \text{ cm}^{-1}$  is assigned as D''-band,<sup>10</sup> which can originate due to high density of edges,<sup>11</sup> bond stretching mode of  $sp^3$  hydrogenated

carbon,<sup>12</sup> and presence of pentagon rings.<sup>13</sup> The peak at about  $1500\text{ cm}^{-1}$  is assigned as D\* band which is attributed to the presence of interstitial defects or out-of-plane defects,<sup>14</sup> pentagon-heptagon structure,<sup>13</sup> trans-polyethylene<sup>15</sup> and fullerene-like structures.<sup>16</sup>

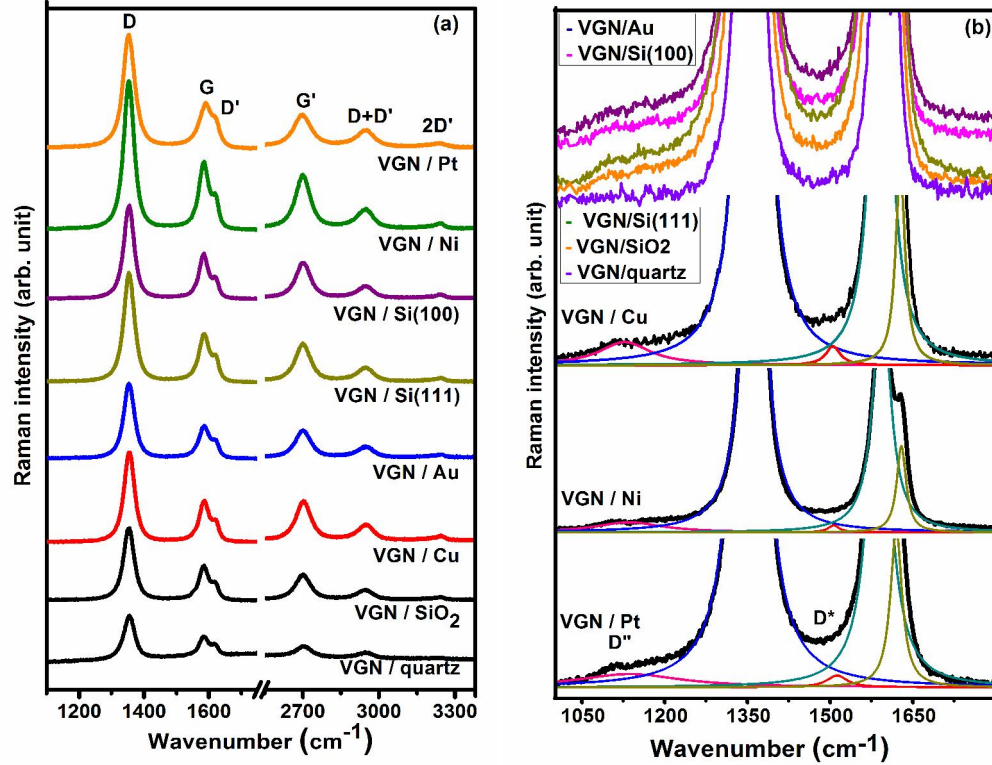


Figure 4.6: (a) Raman spectra, and (b) closer view of first order Raman modes of VGN grown on various substrates.

Table 4.5: Extracted parameters of Raman spectra of VGN grown on different substrates

Substrate	Pos <sub>D</sub> (cm <sup>-1</sup> )	FWHM <sub>D</sub> (cm <sup>-1</sup> )	Pos <sub>G</sub> (cm <sup>-1</sup> )	FWHM <sub>G</sub> (cm <sup>-1</sup> )	Pos <sub>G'</sub> (cm <sup>-1</sup> )	FWHM <sub>G'</sub> (cm <sup>-1</sup> )	I <sub>D</sub> /I <sub>G</sub>
Pt	1353.3±0.4	43.3±0.5	1589.1±0.2	46.7±0.5	2698.0±0.7	85.7±2.4	2.59
Ni	1353.8±0.0	37.3±0.2	1585.0±0.1	36.5±0.1	2700.5±0.1	69.1±0.2	2.23
Si <sub>100</sub>	1353.7±0.4	36.9±0.2	1584.5±0.3	34.9±0.7	2701.3±0.4	68.5±0.6	2.12
Si <sub>111</sub>	1353.7±0.1	38.5±0.2	1585.6±0.0	39.4±0.1	2700.0±0.1	72.9±0.9	2.26
Au	1353.7±0.3	39.1±0.3	1585.5±0.0	39.8±0.3	2699.9±0.2	73.5±0.7	2.34
Cu	1354.8±0.4	37.8±0.0	1585.9±0.4	36.9±0.1	2702.4±0.4	70.3±1.0	2.21
SiO <sub>2</sub>	1353.3±0.2	38.3±0.2	1585.0±0.3	35.8±0.2	2700.5±0.1	71.0±0.5	2.15
quartz	1355.1±0.4	38.7±0.2	1585.5±0.3	33.1±0.4	2703.8±0.7	70.5±1.8	2.36

#### 4.4.4 Discussion

As discussed earlier, FESEM analysis confirms that the aerial density, vertical height and shape of nanosheets (petal-like or maze-like) are found to vary with respect to substrate (Fig. 4.4). Further, the height of VGN and CA measured on these substrates increase with thermal conductivity of the substrates, as provided in Table 4.4 except for SiO<sub>2</sub> and quartz substrates. Thus, in addition to the surface energy, thermal conductivity of substrates influence early stage nucleation of VGN. The input power or total flux of heat towards substrate is given by equation 4.1<sup>17</sup>

$$\dot{Q}_{in} = \left[ \rho_S d_S A_S c_S \left( \frac{dT_S}{dt} \right) \right] + \left[ \alpha \chi p T_S A_S + \frac{\lambda_S}{d_S} A_S (T_S - T_H) + 2\sigma A_S (T_S - T_H) \right] \quad (4.1)$$

In Eqn. (4.1), the first and second terms represent the transferred power to heat the substrate and the liberated power from the substrate respectively. The  $\rho_S$ ,  $d_S$ ,  $A_S$ ,  $c_S$ , and  $\lambda_S$  are mass density, thickness, area, specific heat capacity and thermal conductivity, respectively.  $\alpha$  is the sticking co-efficient of plasma species on the substrate surface,  $\chi$  is the molecular heat conductivity of gas,  $p$  is the gas pressure (in 10<sup>-3</sup> mbar) and  $\sigma$  is the Stefan-Boltzmann constant. In the case of PECVD growth, the substrate surface temperature ( $T_S$ ) is always greater than the heater temperature ( $T_H$ ), due to the plasma surface interaction. As discussed earlier [Section 3.5], the nucleation of hydrocarbon species starts from localized hot spots. The size and density of such localized hot spots depend on the substrate and plasma characteristics. The adsorption rate or sticking co-efficient ( $\alpha$ ) of radicals depends on the nature of the substrate,<sup>18</sup> localized hot spot size and plasma process parameters ( $\chi$ ,  $p$ ,  $T_S$ ,  $T_H$ ). Thus the size, shape and density of NG islands depend on the characteristics of localized hot spots. In addition, the interfacial base layer,

which forms between substrate and vertical layer of graphene, contains highly defective NG, *a*-C, carbon onions and point defects such as pentagon, heptagon rings. Raman analysis confirms the presence of such defects from the observation of D'' and D\* in the first order Raman spectra [Fig. 4.6(b)]. Direct evidence of the defects viz. *a*-C and carbon onions are shown by Zhao *et al.*<sup>9</sup> using TEM.

It is noteworthy that the morphology of VGN on SiO<sub>2</sub> and quartz are entirely different even though both substrates have similar thermal conductivity, *rms* roughness and are amorphous in nature (Table 4.4). This is because of fact that the thermally oxidized Si (SiO<sub>2</sub>) contains large amount of defects which act as nucleation sites resulting in high density of VGN. Whereas quartz substrates with relatively less defects produce VGN of low density. Further investigation is required to understand the growth of VGN on SiO<sub>2</sub> and quartz substrates.

Overall, it is observed that the physical characteristics of NG interfacial layer play a crucial role in determining the growth rate, morphology and structure of VGNs grown on different substrates. The physical characteristics of NG base layer depend on the surface energy and thermal conductivity of substrates. A larger amount of hot spots are formed on the substrates when the thermal conductivity of the substrate is low and surface energy of the substrate is high which in turn lead to higher aerial density is achieved and vice versa. Thus, the substrates are found to plays an important role in deciding the final morphology of VGN through the formation of interfacial NG layer.

#### **4.5 Thermal stability of vertical graphene nanosheets**

Vertical graphene nanosheets are annealed under Ar/H<sub>2</sub> (9:1) atmosphere at the temperature of 800 °C. Prior to annealing, the chamber was evacuated down to  $1 \times 10^{-5}$

mbar using turbo molecular pump and purged a few times with Ar. The annealing process was carried out under Ar (5N purity) at flow rates of 18 sccm and H<sub>2</sub> (5N purity) at flow rates of 2 sccm. The pressure of the vacuum system under Ar/H<sub>2</sub> atmosphere was maintained at  $3.6 \times 10^{-3}$  mbar. The annealing time was varied from 2 to 16 hrs. The 16 hrs annealing at 800 °C was carried out in two stages of 8 hrs each without removing the sample from vacuum chamber. After annealing, the samples were allowed to cool down to room temperature in same environment.

#### 4.5.1. FESEM analysis

Figures 4.7(a) and 4.7(b) show the surface morphology of the pristine and 16 hrs annealed VGN, respectively and having wall density of about  $800/\mu\text{m}^2$ . The insets in Fig. 4.7 show the corresponding cross sectional image of VGN with vertical height of about 150 nm. No observable morphological change is detected in the scanning electron micrographs for the as-grown and samples annealed at 800 °C for 2, 4, 8 and 16 hrs.

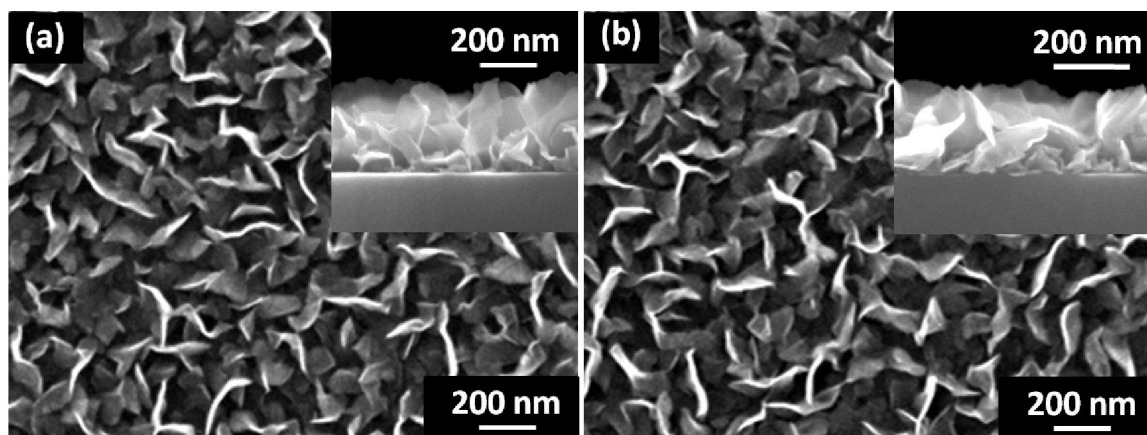


Figure 4.7 FESEM micrographs of (a) as-grown, and (b) 16 hrs annealed VGN. Insets represent corresponding cross sectional FESEM micrographs

#### 4.5.2. Raman spectroscopic analysis

Figure 4.8(a) represents Raman spectra of as-grown and annealed VGN. The spectra apparently do not show any variation with annealing. Further, the spectra are fitted with Lorentzian lineshape and the extracted parameters of FWHM and peak position of Raman bands - D, G and G' are shown in Figs. 4.8(b) and 4.8(c), respectively. Although thermal treatment is expected to improve the crystallinity, no systematical change in FWHM of D, G and G' band is observed with respect to annealing duration [Fig. 4.8(b)]. Also, the position of Raman bands is nearly unchanged with respect to annealing time [Fig. 4.8(c)]. However, the position of G band ( $1584\text{ cm}^{-1}$ ) and G' band ( $2698\text{ cm}^{-1}$ ) of the VGN is blue-shifted compared to the Pos(G)  $\sim 1580\text{ cm}^{-1}$  and Pos(G')  $\sim 2690\text{ cm}^{-1}$  of exfoliated single layer graphene.<sup>8</sup> This can be attributed to the unintentional hole doping by ambient  $\text{O}_2$  and  $\text{H}_2\text{O}$  molecules which make bonding with carbon atoms at the edges and other defect sites. Further, the FWHM (D/G/G') of the sample annealed for 16 hrs show slight broadening which can be due to temperature induced degradation in the graphitic structure.

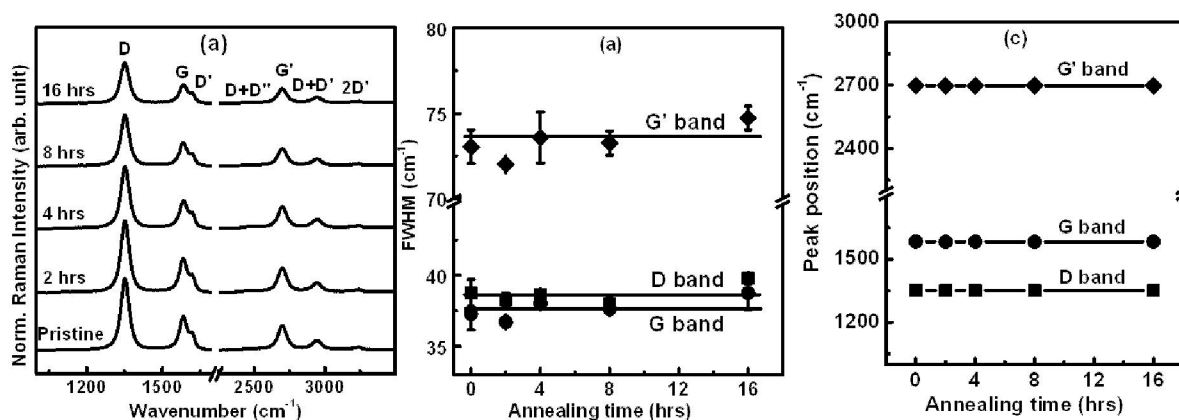


Figure 4.8: (a) Raman spectra of as-grown and annealed VGN, (b) FWHM and (c) position of D, G, G' bands of VGN as a function of annealing time

In order to get a clear picture, the analysis is further extended by comparing the intensity ratios of D to G ( $I_D/I_G$ ), D' to G ( $I_{D'}/I_G$ ) and G' to G ( $I_{G'}/I_G$ ) as a function of annealing time and plotted in Fig. 4.9. It is observed that both  $I_D/I_G$  and  $I_{D'}/I_G$  increases with increasing annealing time [Fig. 4.9(a-b)]. The increase of D and D' band intensities clearly indicate that the amount of defects increases with annealing time. It clearly indicates that the annealing introduces defects in the VGN without affecting the overall graphitization.

The edges are the most probable to get damaged during annealing while other types of defects are expected to decrease when annealing is performed under vacuum and inert atmosphere. Since, the growth of VGN was performed at 800 °C for 30 min duration, the possible bulk defects would have been removed during growth itself. Xu *et al.*<sup>19</sup> reported

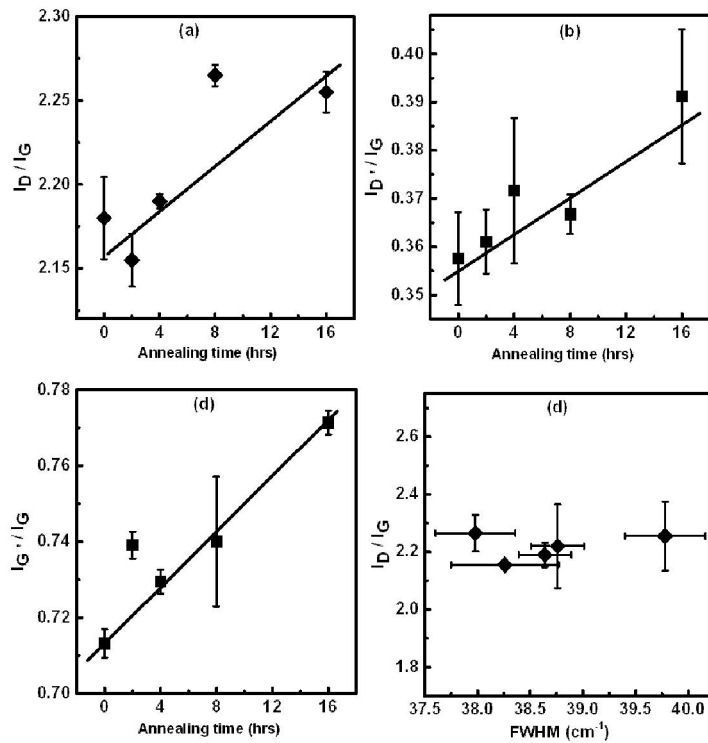


Figure 4.9: (a) Variation of  $I_D/I_G$  with annealing time (b) FWHM of G vs  $I_D/I_G$ , (c) variation of  $I_{D'}/I_G$  and (d)  $I_{G'}/I_G$  as a function of annealing time. Solid lines are guide to eye

that graphene edges are not stable and undergo modifications while annealing at temperature as low as 200 °C. Also, it is reported that the zig zag edges rearrange and form armchair segments. While, the armchair edges are fragmented further to armchair segments even at annealing temperature as high as 500 °C (Fig. 4.10).<sup>19</sup> Further, it should be noted that a perfect zig zag edge does not contribute to Raman D band intensity but it contributes for D' band intensity. Hence, the increase of  $I_D/I_G$  and  $I_{D'}/I_G$  can be correlated with the increase of armchair edge segments due to high temperature induced degradation of edges. The  $I_G/I_G$  also increases with annealing time as shown in Fig. 4.9(c). This trend is consistent with the improvement of crystallinity of few layer graphene with annealing. Figure 4.9(d) shows the plot of  $I_D/I_G$  as a function of FWHM of G band, as a collection of data from samples annealed for different durations. It shows a negligible variation of  $I_D/I_G$  with FWHM of G band. It is reported that the  $I_D/I_G$  ratio does not vary significantly with FWHM of G band for edge dominated defects in few layer graphene flakes. On the other hand,  $I_D/I_G$  increases with FWHM for the samples with large amount of bulk defects.<sup>20</sup> From the negligible variation of  $I_D/I_G$  with FWHM of G band variation, it can be concluded that the edges dominates the Raman defect band intensity in comparison to bulk defects.

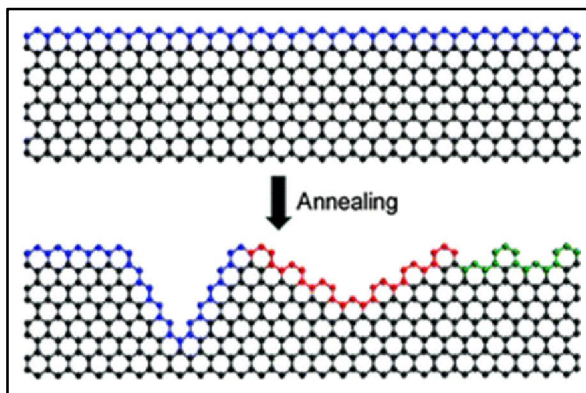


Figure 4.10: Schematic of edge fragmentation of graphene upon annealing (Ref<sup>19</sup>)

### 4.5.3. Electrical properties

The variation of sheet resistance with annealing time is investigated by four probe resistivity method. The annealed VGN exhibits smaller sheet resistance than that of pristine VGN. Initially, the sheet resistance decreases from  $1.24 \text{ K}\Omega/\square$  to  $0.99 \text{ K}\Omega/\square$  for annealing upto 8 hrs and then it shows a slight increase in sheet resistance to  $1.06 \text{ K}\Omega/\square$  for 16 hrs annealing. The decrease in resistance indicates that the structural quality of VGN improves or the net carrier concentration increases upon annealing. Also, it is known that the adsorption of atmospheric molecules on graphene surfaces increases after high temperature annealing.<sup>21</sup> Increased adsorption of atmospheric molecules on fragmented graphene edges introduce heavy hole doping in VGN which eventually decreases the sheet resistance.

## 4.6 Discussion

In conclusion, the effect of high temperature annealing on the structural properties of VGN under different duration is investigated. SEM analysis suggests no observable change in morphology upon annealing. Raman spectroscopic analysis shows insignificant change in FWHM and peak position of pristine and annealed samples. However, the intensities of defect bands (D and D') show a small increase with annealing time. The increase of defect band intensities implies that graphene edges density increases upon annealing. Hence, the thermal annealing deteriorates the graphene edges and creates more edge segments upon annealing because of temperature induced degradation of the edges. However, the graphitic structure is not significantly modified even for annealing at  $800 \text{ }^\circ\text{C}$  for 16 hrs. Further, the sheet resistance also decreases with annealing. This study

concludes that the VGN are stable under high temperature annealing, which may help one to design the material for electronic, sensing, and energy storage applications.

#### **4.7 Summary**

The results and inference of this chapter is summaries as follows

- The precise control of the final structure and morphology of uniform and homogeneous VGN over a large area are achieved by tuning the plasma process parameters like MW power and distance from plasma source to substrate in PECVD system.
- The substrate properties like thermal conductivity, surface energy and atomic density are found to play responsible role on the final morphology and structure.
- The VGN are found to be thermally stable under high temperature annealing.

## 4.8 References

1. Levchenko, I., *et al.*, *Physics of Plasmas (1994-present)* (2007) **14** (6), 063502
2. Xiong, G., *et al.*, *Diamond Relat. Mater.* (2012) **27**, 1
3. Srivastava, S. K., *et al.*, *Thin Solid Films* (2005) **492** (1), 124
4. Neyts, E. C., *Plasma Chem. Plasma Process.* (2016) **36** (1), 185
5. Uher, C., Thermal conductivity of metals. In *Thermal Conductivity*, Springer, (2004), pp 21
6. Kim, J. H., *et al.*, *J. Appl. Phys.* (1999) **86** (7), 3959
7. Glassbrenner, C., and Slack, G. A., *Phys. Rev.* (1964) **134** (4A), A1058
8. Wang, Y. y., *et al.*, *J. Phys. Chem. C* (2008) **112** (29), 10637
9. Zhao, J., *et al.*, *Nano Lett.* (2014) **14** (6), 3064
10. Ferrari, A. C., and Basko, D. M., *Nat. Nanotechnol.* (2013) **8** (4), 235
11. Wang, J., *et al.*, *Appl. Phys. Lett.* (2004) **85** (7), 1265
12. Karlin, S., and Colomban, P., *J. Raman. Spectrosc.* (1997) **28** (4), 219
13. Tarrant, R., *et al.*, *Diamond Relat. Mater.* (2004) **13** (4), 1422
14. Rouzaud, J., *et al.*, *Thin Solid Films* (1983) **105** (1), 75
15. Ferrari, A. C., and Robertson, J., *Philos. Trans. R. Soc. London, Ser. A* (2004) **362** (1824), 2477
16. Blank, V., *et al.*, *Nanotechnology* (2007) **18** (34), 345601
17. Kersten, H., *et al.*, *Vacuum* (2001) **63** (3), 385
18. Hori, M., and Goto, T., *Appl. Surf. Sci.* (2007) **253** (16), 6657
19. Xu, Y. N., *et al.*, *ACS nano* (2010) **5** (1), 147
20. Bracamonte, M. V., *et al.*, *J. Phys. Chem. C* (2014) **118** (28), 15455
21. Ni, Z. H., *et al.*, *J. Raman. Spectrosc.* (2010) **41** (5), 479

# 5

## **Electrochemical Performance of Vertical Graphene Nanosheets as Supercapacitor Electrode**

*Vision without execution is delusion  
Thomas Edison*

The electrochemical performances and capacitance of VGN electrodes of different morphology are studied using three-electrode system in 1M H<sub>2</sub>SO<sub>4</sub>, 1M Na<sub>2</sub>SO<sub>4</sub>, and 1M KOH electrolytes. The charge storage performance is investigated by the help of cyclic voltammetry, charge-discharge, electrochemical impedance spectroscopy and equivalent circuit modeling. A high areal specific capacitance of about 188  $\mu\text{F}/\text{cm}^2$  at a scan rate of 100 mV/s is observed for the VGN directly grown on the Si(100) substrates without use of any additional binder and current collector. To further improve its performance, the VGN surface is decorated with MnO<sub>2</sub> and their electrochemical properties are studied. The variation in electrochemical performances with VGN morphology, aqueous electrolyte and MnO<sub>2</sub> decoration provide important scientific inferences required for fabricating VGN based energy storage devices with superior electrochemical performances.

## 5.1 Introduction

Due to the inherent properties, vertical graphene nanosheets (VGN) meets the criteria for utilization as a supercapacitor (SC) electrode. Since, the SC performance depends on the morphology of electrode material, the electrochemical performances of VGN with different morphology are carried out in 1M H<sub>2</sub>SO<sub>4</sub> electrolyte. It should be noted that, the SC performance not only depends on the morphology of electrode material, but also on the choice of suitable electrolyte used. Hence, the capacitive performance using VGN of suitable morphology is investigated in 1M Na<sub>2</sub>SO<sub>4</sub> and 1M KOH in addition to 1M H<sub>2</sub>SO<sub>4</sub>. Moreover, to improve the performance of VGN electrode, MnO<sub>2</sub> is decorated on VGN and the electrochemical performance is studied.

## 5.2 Role of morphology

To study the role of morphology on electrochemical performance as SC electrode, VGN with different morphology are synthesized. The altered morphologies are resulted due to changes in plasma condition achieved by variation of CH<sub>4</sub>/Ar ratio and deposition time. Growth conditions for VGN of different morphology are listed in Table 5.1. Films are grown under 5/7 sccm of CH<sub>4</sub>/Ar for 30 min, 5/25 sccm of CH<sub>4</sub>/Ar for 30 min and 60 min are labeled as VGN1, VGN2 and VGN3, respectively. The details of growth conditions for VGN are briefed in Section 3.2.

Table 5.1: Growth conditions for VGN electrode of different morphology

Sample	Fixed parameters	Gas flow rate [sccm]		Growth time (min)
		CH <sub>4</sub>	Ar	
VGN1	Temp: 800C	5	7	30
VGN2	Distance:40cm	5	25	30
VGN3	Power:375W	5	25	60

### 5.2.1 FESEM analysis

The morphology of electrode materials in terms of open network and accessible surface area are the important factors for charge storage systems. The morphologies obtained are shown in Fig. 5.1(a-c). The highest areal density and well separated vertical sheets are observed in VGN1 [Fig. 5.1(a)]. VGN2 contains interconnected vertical network. On the other hand VGN3 contains lowest wall density with large interconnected open networks which ensure larger available geometrical surface area than VGN1 and VGN2. In addition, the maximum lateral length of each sheet is found to be close to one micrometer in length.

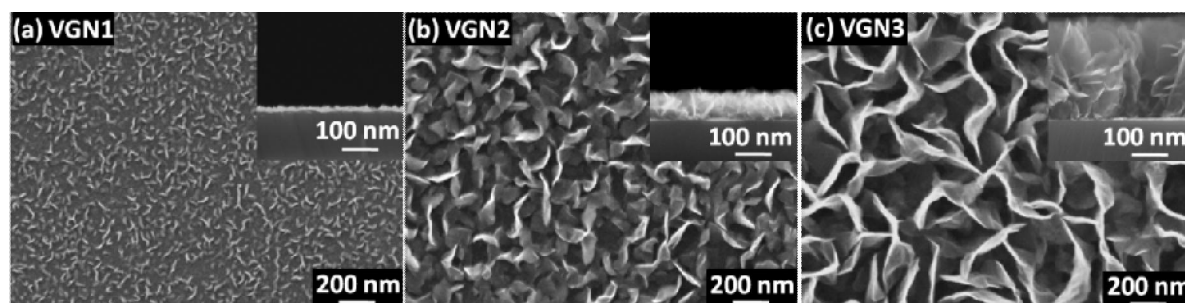


Figure 5.1: FESEM micrographs of VGN electrode grown under different process parameters. Insets represent corresponding cross sectional FESEM micrographs of VGN.

As shown in inset of Fig. 5.1(a-c), the cross sectional height of VGN varies from 27 nm to 589 nm. The stress between the sheets leads to their bending, folding and subsequent falling down on each other. A closer view of inset of Fig. 5.1(c) reveals the formation of secondary sheets through sidewise growth from the vertical sheets.<sup>1</sup>

### 5.2.2 Raman spectroscopic analysis

Figure 5.2(a) shows representative Raman spectra of VGN1 and similar spectra are also observed for VGN2 and VGN3. Extracted parameters are listed in Table 5.2. No

systematic or significant change in full width at half maximum (FWHM) of D/G/G' band is found for those three samples.

### 5.2.3 XPS analysis

Figure 5.2(b) shows the photoemission signal of VGN1 and the inset represents C1s spectrum. The details of the peaks and their origin are already discussed in Section 3.2.3. The  $sp^2$  content of all the VGN samples obtained from the C1s spectra are listed in Table 5.2. As XPS is a surface sensitive technique, the C1s spectra are of similar nature.

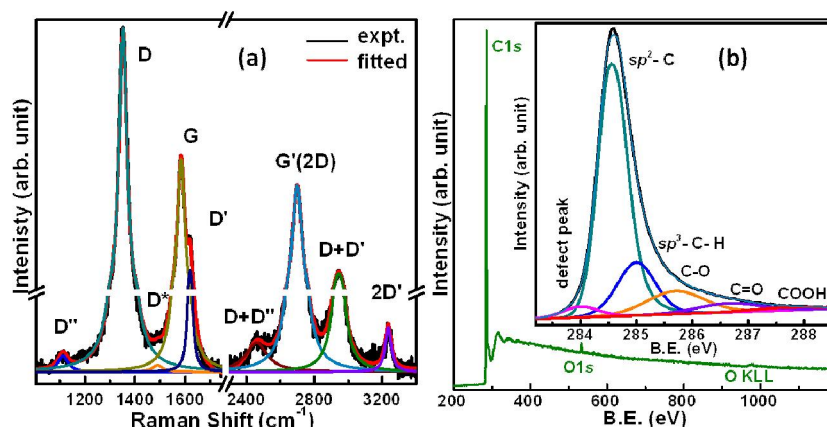


Figure 5.2: (a) Raman spectra and (b) photoemission signal of VGN1 and inset represents the C1s of VGN1

The results of Raman and X-ray photoelectron spectroscopy indicate no chemical and structural differences in samples with different morphologies. To probe it further, sheet resistance of these samples are measured.

### 5.2.4 Electrical properties

The sheet resistance of the films are measured by four-probe resistive method and the results are listed in Table 5.2. VGN3 shows low sheet resistance of  $0.86 \text{ K}\Omega/\square$  compared to VGN1 ( $3.09 \text{ K}\Omega/\square$ ) and VGN2 ( $1.88 \text{ K}\Omega/\square$ ). From the analysis of SEM

micrograph, Raman spectra and XPS spectra, the change in sheet resistance of the sample can be interpreted as a result of modification in geometry of the structure. The high conducting nature of the film decreases the internal resistance and thereby enhances the electron transfer as well as assist in accumulation of charges for electric double layer (EDL) formation.

Table 5.2: Extracted physical parameters of VGN

sample	Vertical height nm	FWHM of D/G/G' (cm <sup>-1</sup> )	<i>sp</i> <sup>2</sup> content (%)	Sheet Rest. KΩ/□	C <sub>s</sub> at 100 mV/s (μF/cm <sup>2</sup> )	C <sub>v</sub> at 100 mV/s (F/cm <sup>3</sup> )
VGN1	27.8	32.5/28.9/62.8	78.6	3.09	11.22	4.04
VGN2	150.3	39.4/35.9/71.7	78.7	1.88	40.59	2.70
VGN3	421.3	37.8/34.1/69.4	78.8	0.86	188.04	4.47

### 5.2.5 Cyclic Voltammetry study

The cyclic voltammogram (CV) of VGN electrodes at scan rates in the range of 50 to 500 mV/s is shown in Fig. 5.3. The scan rate is found to be inconsequential towards shape of the CV. Without any obvious redox peak, the increasing current density with scan rate indicates excellent stability as well as superior capacitive behavior. The symmetric shape of CV at both positive and negative polarization confirms the diffusive ingress of electrolyte ions into the structure. However, shape of the CV is observed to deviate from typical rectangular shape observed for pure SC. This deviation is due to the pseudocapacitance arising from oxygen- and/or -OH containing functional groups present on the edges of VGN, as shown in XPS result. The specific capacitance of electrode materials (C<sub>s</sub> in F/cm<sup>2</sup>) is calculated from CV using the formula given below

$$C_s = \frac{\int Idv}{s.A.\Delta V} \quad (5.1)$$

where,  $s$  is the scan rate for the particular CV,  $A$  is the area exposed to electrolyte and  $\Delta V$  is the potential window through which active electrode material is scanned.

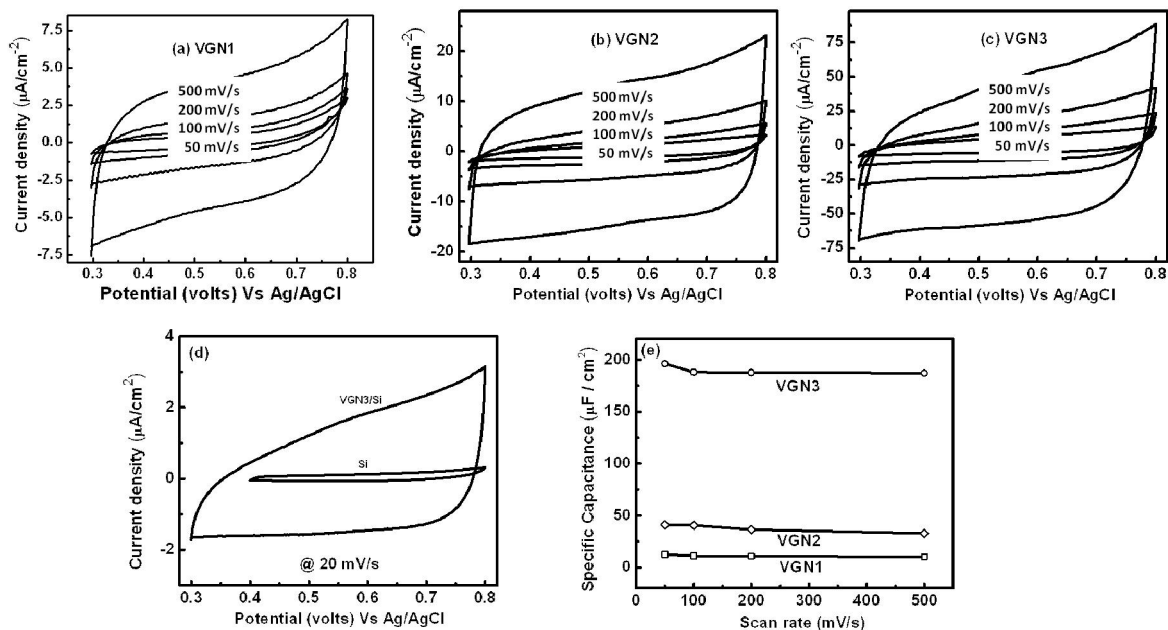


Figure 5.3: Cyclic voltammogram (CV) of (a) VGN1, (b) VGN2, and (c) VGN3 at scan rates in the range of 50-500 mV/s in 1M  $\text{H}_2\text{SO}_4$  electrolyte, (d) comparison of CV of Si and VGN/Si at 20 mV/s scan rate and (e) plot of specific capacitance vs scan rate for VGN

The observation from CV for bare Si substrate confirms that the result depicted in Fig. 5.3 corresponds to VGN and the contribution from Si substrate is negligible. Here, Si just acts as a mechanical support. The specific capacitance values at scan rate of 100 mV/s found for VGN1, VGN2 and VGN3 are 11.22, 40.59 and 188.04  $\mu\text{F}/\text{cm}^2$ , respectively. The result is comparable with the reported value, where Ni, Ni foam, Pt or other additional current collectors were used.<sup>2-5</sup> The obtained result can be explained in terms of unique geometry of VGN, where the cavities (space between the vertical sheets) can serve as “ion buffering reservoir” such that the electrolyte ions can access full sheet surface area and each vertical sheet can serve as nanoelectrode.<sup>6,7</sup> In addition to that, secondary walls nested

inside the cavities also participate in the charge storage performance. The direct growth of VGN without the use of binder and additional current collector is one of the advantages over the other materials where use of binder and current collector are necessary for SC electrode fabrication. The present  $C_s$  value can be further increased by increasing the height of VGN.<sup>8</sup> This can be achieved by optimizing the growth parameters, as discussed in Chapter 3 and Chapter 4. The volumetric capacitance ( $C_v$ ) is calculated from  $C_s$  by dividing it with vertical height and the values are listed in Table 5.2. It is seen that VGN2 has less  $C_v$  compared to the VGN1, while VGN3 shows higher  $C_v$  than that of VGN1. Although VGN2 has more vertical height with nanocavities compared to VGN1, the accessibility of electrolyte ions is found to be low due to the poor open structure. This situation leads to the less capacitive performance. The high capacitance value of VGN3 ( $4.5 \text{ F/cm}^3$ ), can be attributed to the availability of excess open porous structure, large accessible area and more conducting nature.<sup>2</sup> Therefore it is concluded that VGN should have optimum vertical height and cavity size for effective performance.

### 5.3 Role of different aqueous electrolytes

Since VGN3 has optimum vertical height and cavity size, it is used for the study of the effect of electrolyte on electrochemical performance. The electrochemical performance of VGN3 in  $\text{Na}_2\text{SO}_4$ ,  $\text{KOH}$  and  $\text{H}_2\text{SO}_4$  electrolytes are investigated by CV, charge-discharge and electrochemical impedance spectroscopy (EIS) to choose suitable electrolyte for effective utilization of VGN. The wetting properties of VGN3 in different aqueous electrolyte are analyzed by contact angle measurement. An electrical equivalent circuit is simulated from the impedance plot to understand the VGN/aqueous electrolyte interfaces.

### 5.3.1 Wetting properties

The wetting property of the film is one of the key parameters for their application as SC electrode. The water contact angle of  $133^\circ$  confirms the near superhydrophobic nature of the film. The initial contact angles of VGN3 in 1M  $\text{Na}_2\text{SO}_4$ , 1M KOH and 1M  $\text{H}_2\text{SO}_4$  electrolyte solution are  $126.8^\circ$ ,  $118.9^\circ$  and  $130.7^\circ$ , respectively. The time dependent wettability of VGN3 with the electrolyte solutions are shown in Fig. 5.4. The slope of the curve represents the change in wettability (hydrophobic to hydrophilic) with time and found to be  $0.74^\circ$ ,  $1.77^\circ$  and  $0.81^\circ$  per minute. The result clearly indicates that the wettability of KOH is higher than the other two electrolytes.

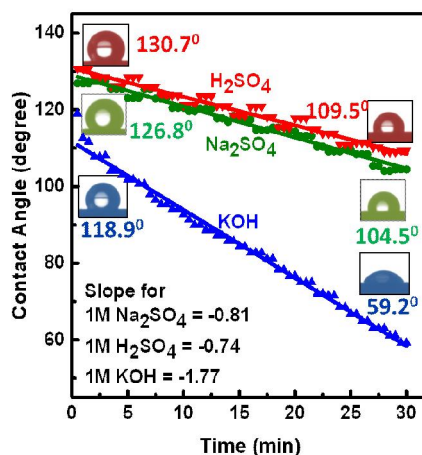


Figure 5.4: Time dependent wettability of VGN3 in 1M  $\text{Na}_2\text{SO}_4$ , 1M KOH, and 1M  $\text{H}_2\text{SO}_4$  electrolyte medium

### 5.3.2 Cyclic Voltammetry study

The current response voltammograms of VGN3, at 100 to 500 mV/s scan rates, in 1M  $\text{Na}_2\text{SO}_4$ , 1M KOH, and 1M  $\text{H}_2\text{SO}_4$  electrolyte are illustrated in Fig. 5.5(a-c). The voltage range is fixed from the results of a preliminary CV. The fixed ranges are 0.1-0.6 V, (-) 0.2-0.3 V and 0.3-0.8 V, respectively. The potential window (0.5 V) is found to be same for all the electrolytes studied. It is seen from Fig. 5.5(a-c) that the current response

increases with scan rate. The unaltered, mirror symmetric and quasi-rectangular shape of CV at various scan rates for the VGN3/Na<sub>2</sub>SO<sub>4</sub>, VGN3/KOH and VGN3/H<sub>2</sub>SO<sub>4</sub> systems confirm the near ideal capacitive behavior with good electrochemical reversibility. The maximum C<sub>s</sub> is found for the VGN3/KOH system (197 μF/cm<sup>2</sup>), followed by 188 μF/cm<sup>2</sup> for VGN3/H<sub>2</sub>SO<sub>4</sub> system at 100 mV/s. The results are found to be in good agreement with the existing literature.<sup>2</sup> The observed lowest C<sub>s</sub> of 44 μF/cm<sup>2</sup> for the VGN/Na<sub>2</sub>SO<sub>4</sub> system is still higher than the reported double layer capacitance of highly porous interconnected carbon nanosheets and advanced activated carbon in organic electrolyte medium (10 μF/cm<sup>2</sup>).<sup>9</sup>

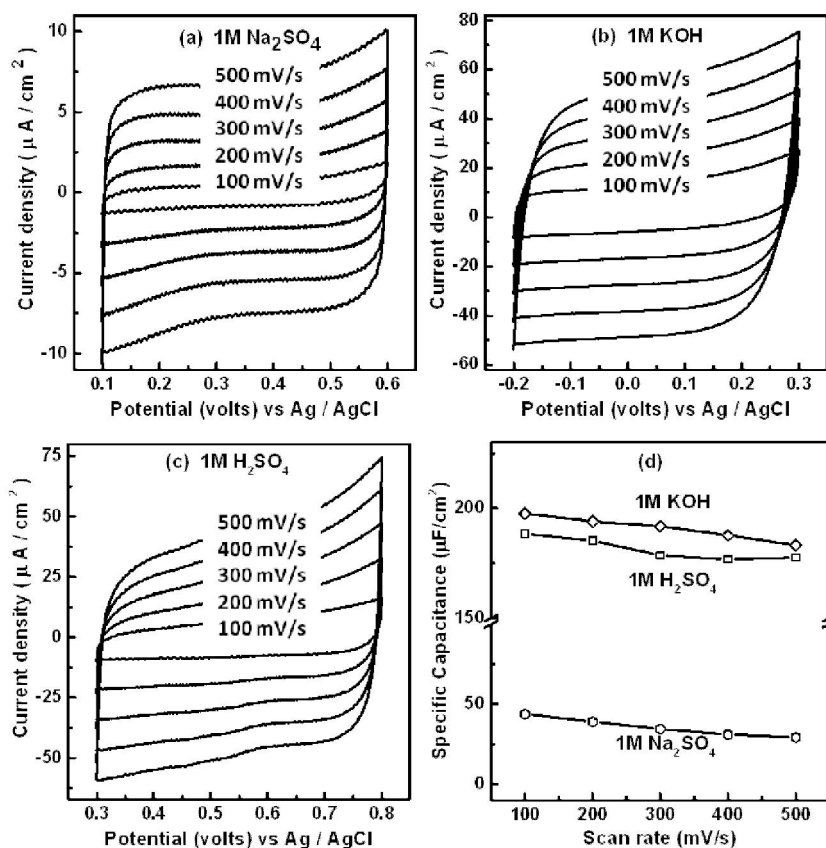


Figure 5.5: Cyclic voltammogram of VGN3 in (a) 1M Na<sub>2</sub>SO<sub>4</sub>, (b) 1M KOH, and (c) 1M H<sub>2</sub>SO<sub>4</sub> medium at scan rate ranges 100, 200, 300, 400, 500 mV/s. (d) Specific capacitance vs scan rate of VGN3 in different aqueous electrolytes

The variation in  $C_s$  values in different systems can be attributed to the difference in ion permeability into the active matrix.<sup>10</sup> The different rate of accessibility of vertical surface by the ions in the matrix depends on ionic radius, ionic mobility and molar ionic conductivity.<sup>11</sup> The corresponding parameters are listed in Table 5.3. The  $C_s$  is found to be slightly higher in KOH than that in  $H_2SO_4$ , although the size of  $K^+$  ions are larger compared to  $H^+$  ions. This can be attributed to the higher wettability of VGN3 in 1MKOH, as shown in Fig. 5.4. The relatively large  $C_s$  in  $H_2SO_4$  medium can be attributed to the higher ionic mobility and molar ionic conductivity of  $H^+$  ions. On the other-hand, the relatively low  $C_s$  in  $Na_2SO_4$  is due to the higher radius of  $Na^+$  ions ( $3.58 \text{ \AA}$ ), and therefore lower ionic mobility and molar ionic conductivity compared to those of  $H^+$  ions. The  $C_s$  values for all the systems are found to decrease with increasing scan rate [Fig. 5.5(d)]. This can be attributed to the reduced access to the interior of the interconnected network by ions at higher scan rate.

Table 5.3: Characteristic parameters of ions of the distinct aqueous electrolyte<sup>12,13</sup>

Ion	Ionic radius ( $\text{\AA}$ )	Radius of hydrated sphere ( $\text{\AA}$ )	Ionic mobility $10^{-8} \text{ m}^2\text{s}^{-1}\text{V}^{-1}$	Molar ionic conductivity $\text{ms.m}^2.\text{mol}^{-1}$
$Na^+$	1.02	3.58	5.19	5.01
$K^+$	1.38	3.31	7.62	7.32
$H^+(H_3O^+)$	0.021	2.80	36.23	34.96
$OH^-$	0.46	3.00	20.64	19.91
$SO_4^{-2}$	2.30	3.79	8.29	16.00

### 5.3.3 Charge-discharge study

The charge-discharge responses for different VGN3/electrolyte systems at various current densities are shown in Fig. 5.6 (a-c). As it can be seen, non-linear charging profile is observed in all the cases at low current density. At high current density, the voltage-time

curves for the VGN3/ $\text{Na}_2\text{SO}_4$  and VGN3/ $\text{H}_2\text{SO}_4$  systems are nearly linear and symmetric without obvious potential drop. Whereas, non-linear charging profile and asymmetric voltage-time response is observed for the VGN3/ $\text{KOH}$  system. This observation indicates better EDL formation, across the electrode/electrolyte interface in VGN3/ $\text{Na}_2\text{SO}_4$  and VGN3/ $\text{H}_2\text{SO}_4$  systems.

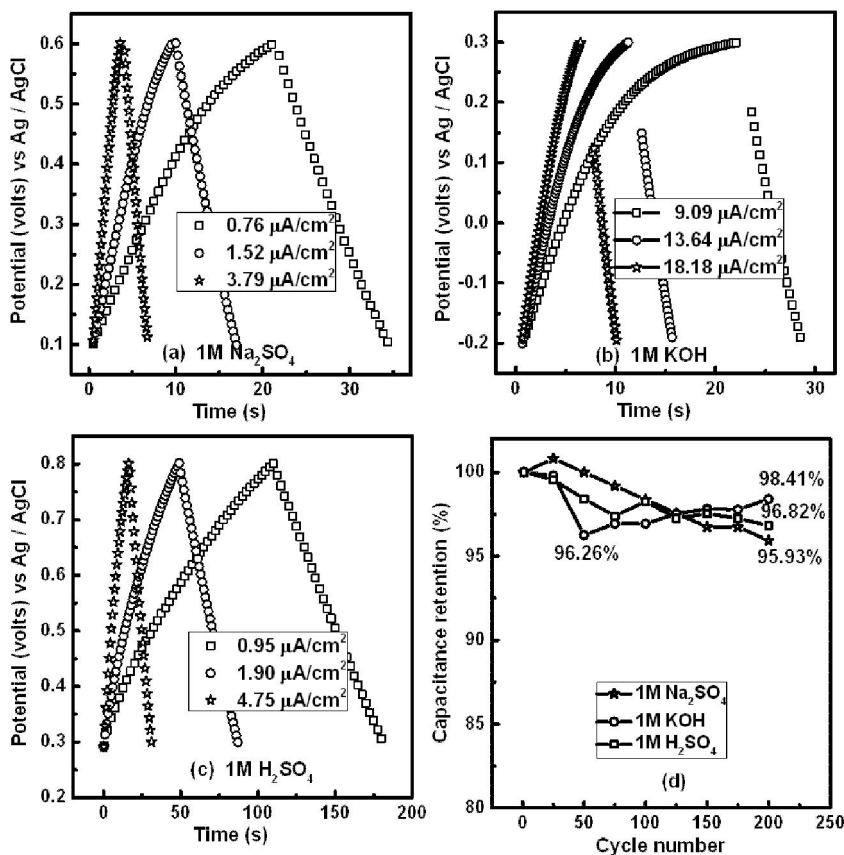


Figure 5.6: Charge-discharge profile of VGN3 at different current density in (a) 1M  $\text{Na}_2\text{SO}_4$ , (b) 1M KOH, and (c) 1M  $\text{H}_2\text{SO}_4$  and (d) capacitance retention vs cycle number of VGN3 in different aqueous electrolytes

To get further insights, energy efficiency ( $\eta$ ) is calculated using the equation (5.2).

$$\eta = \frac{t_D}{t_C} \quad (5.2)$$

where,  $t_D$  and  $t_C$  are discharging and charging time, respectively. The  $\eta$  of VGN3/ $\text{Na}_2\text{SO}_4$ ,

VGN3/KOH, and VGN3/H<sub>2</sub>SO<sub>4</sub> systems are 62.1% at 0.76  $\mu\text{A}/\text{cm}^2$ , 27.6% at 9.09  $\mu\text{A}/\text{cm}^2$  and 64.4% at 0.95  $\mu\text{A}/\text{cm}^2$ , respectively.

### ***Cycle stability***

The cycle life is one of the significant parameters of the SC electrode for evaluating the electrochemical performance. The electrochemical stability of the VGN3/Na<sub>2</sub>SO<sub>4</sub>, VGN3/KOH, and VGN3/H<sub>2</sub>SO<sub>4</sub> systems are evaluated by repeating 200 charge-discharge cycles for corresponding current density and potential window. Figure 5.6(d) shows the capacitance retention of VGN3 in various electrolytes as a function of charge-discharge cycle number. The VGN3/H<sub>2</sub>SO<sub>4</sub> system exhibits excellent electrochemical stability (96.82 %) with only 3.18% deterioration of initial C<sub>s</sub> after 200 cycles. The VGN3/Na<sub>2</sub>SO<sub>4</sub> system shows 95.93 % capacitance retention. For the VGN3/KOH system, the capacity retention shows increasing trends with cycle number after 50 cycles. This can be attributed to the improvement in wettability.<sup>10</sup>

### **5.3.4 Electrochemical Impedance study**

To find charge transfer kinetics and possible explanation for the difference in electrochemical performance, the electrochemical behavior of the VGN/electrolyte systems is investigated by EIS.

### ***Bode plot***

Figure 5.7(a) represents the variation of phase angle as a function of frequency, which is known as Bode plot. The phase angles are found to be -85°, -65° and -82° at low frequency in the VGN3/Na<sub>2</sub>SO<sub>4</sub>, VGN3/KOH and VGN3/H<sub>2</sub>SO<sub>4</sub> systems, respectively [Fig. 5.7(a)]. In general, phase angle approaching to -90° confirms good capacitive

performance and rapid charge-discharge process.<sup>14</sup> The present result indicates faster ion diffusion in electrolyte and faster ion adsorption onto the electrode surface in Na<sub>2</sub>SO<sub>4</sub>, and H<sub>2</sub>SO<sub>4</sub> compared to KOH.

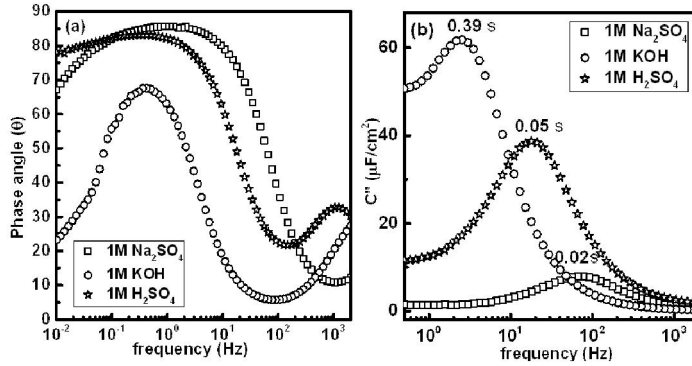


Figure 5.7: (a) Phase angle vs frequency (Bode plot) and (b) evolution of imaginary part of the complex capacitance vs frequency of VGN3 in various electrolyte systems

The relaxation time constant,  $\tau_0$ , defines the time required to deliver the stored charge effectively.<sup>14</sup> To find out time constant of the systems ( $\tau_0$ ), imaginary part of the capacitance ( $C''(\omega)$ ) is calculated using Eqn. (5.3) and plotted against frequency for VGN3/electrolyte systems, as shown in Fig. 5.7(b).

$$C''(\omega) = \frac{Z'(\omega)}{\omega \cdot [Z'(\omega)^2 + Z''(\omega)^2] \cdot A} \quad (5.3)$$

Time constant,  $\tau_0$ , is obtained from the frequency corresponding to maximum  $C''(f_0)$ , using the relation,  $f_0 = 1/\tau_0$ . The  $\tau_0$  values obtained for the VGN3/Na<sub>2</sub>SO<sub>4</sub>, VGN3/KOH and VGN3/H<sub>2</sub>SO<sub>4</sub> systems are 20 ms, 390 ms and 50 ms, respectively. This trend of  $\tau_0$  implies that Na<sub>2</sub>SO<sub>4</sub> and H<sub>2</sub>SO<sub>4</sub> electrolytes are better than KOH in the context of quick delivery of stored charge.

### Nyquist plot

The panels (a), (b) and (c) in Fig. 5.8 represent the Nyquist plot of the VGN3/electrolyte systems after 1st and 200<sup>th</sup> cycles. The insets of Fig. 5.8 show the expanded

high frequency region. In general, the impedance spectrum consists of three regions: a semicircle at high frequency region, a 45° linear region followed by a vertical line in the intermediate to low frequency regime. At high frequency region [inset of Fig. 5.8(a-c)], compared to VGN3/KOH system, a smaller semicircle is observed for the VGN3/Na<sub>2</sub>SO<sub>4</sub> and VGN3/H<sub>2</sub>SO<sub>4</sub> system. This indicates low interfacial charge-transfer resistance. The 45° slopped portion is seen only in the case of VGN3/KOH clearly, after 200 cycles of charge-discharge [inset of Fig. 5.8(b)]. The 45° slopped portion corresponds to the Warburg region and represents higher variation in ionic diffusion path length and increased obstruction of ion movement.<sup>15</sup> The negligible Warburg region of the VGN3/electrolyte system implies short diffusion length of ions in electrolyte. Additionally, it is seen that after 200 cycles of charge-discharge, the Nyquist plots deviates from the original one for the VGN3/KOH system. The observed deviation indicates degradation of the VGN3/KOH interface and can be attributed to the oxidation by KOH.<sup>10</sup> The negligible deviation in the spectra after 200 cycles for VGN3/Na<sub>2</sub>SO<sub>4</sub> and VGN3/H<sub>2</sub>SO<sub>4</sub> systems indicates their excellent electrochemical stability.

This observation is in good agreement with those reported by Ruiz *et al.*<sup>10</sup> The evaluated vertical slopes from Fig. 5.8(a-c) are 87.6°, 84.8°, 86.5° for the VGN3/Na<sub>2</sub>SO<sub>4</sub>, VGN3/KOH, and VGN3/H<sub>2</sub>SO<sub>4</sub> systems, respectively. The slopes close to 90° is indicative of the good capacitive performance.

### ***Simulation of equivalent circuit***

The interpretation of the Nyquist plot usually relies on the construction of a suitable equivalent electric circuit.<sup>16-18</sup> In general, simple Randles circuit was used to represent the electrochemical system [Fig. 5.9(a)]. Our experimental impedance spectra could not be

fitted with this simple model, hence modification to the Randles circuit is required. Since, VGN has varying pore size distribution, inhomogeneity and surface disorder, the capacitance can be replaced by constant phase element (CPE). The presence of CPE indicates the frequency dispersion of EDL and can be expressed as

$$Z_{CPE} = 1/C_{dl}' (j\omega)^n ; 0 < n < 1 \quad (5.4)$$

where  $C_{dl}'$  is proportional to the double layer capacitance and  $j$  is the imaginary unit. The exponent ( $n$ ) is related to the frequency dispersion. For a smooth and clean electrode,  $n$  equal to unity represents the ideal capacitive behavior.<sup>17</sup> The physical structure of VGN3 consists of interconnected array of vertical nanosheets separated by 40-250 nm. In addition to the interconnected vertical sheets, there are secondary walls normal to them. This gives rise to nano and micro cavities of various sizes. The distribution in pore size gives rise to differences in ion mobility and their adsorption. In view of this, a simple modification to the Randles circuit [Fig. 5.9(a)] is used to simulate an appropriate equivalent circuit [Fig. 5.9(b)].

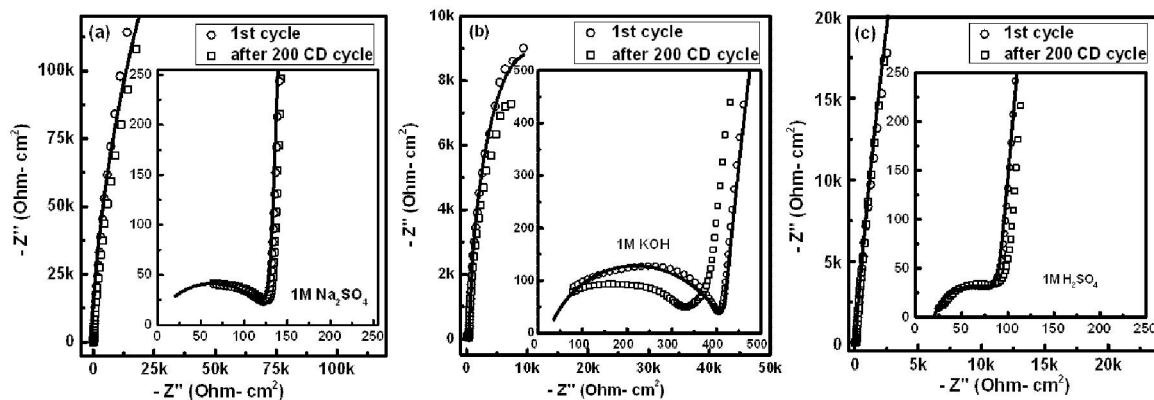


Figure 5.8: Nyquist plot of VGN3 in (a) 1M  $\text{Na}_2\text{SO}_4$ , (b) 1M  $\text{KOH}$ , and (c) 1M  $\text{H}_2\text{SO}_4$  spectra before and after 200 charge-discharge cycles. Insets of (a), (b), (c) represent the expanded high frequency Nyquist plot and solid line indicates fitted data using equivalent circuit [Fig. 5.9(b)]



Figure 5.9: (a) Simple Randles circuit, and (b) modified electrical equivalent circuit for VGN3 electrode in aqueous medium

The fitted curve based on the modified circuit is given in Fig. 5.8(a-c). In the equivalent circuit, resistor element ( $R_s$ ) is the series resistance of the electrolyte and contact. The  $R_s$  value for all systems is found to be almost same. In the case of VGN/electrolyte systems, the formation of EDLC under an ac perturbation involved three processes,<sup>19,20</sup> viz,

- (i) charge accumulation on VGN edges in contact with the electrolyte (high frequency region represented by  $R_1$ ,  $CPE_1$ ,  $n_1$ )
- (ii) the ion diffusion in the cavity, formed by vertical sheets, which allows the migration of ions to the walls of vertical sheets ( $R_2$ , and ( $CPE_2$  and  $n_2$ )) and
- (iii) distributed ionic resistance and double layer capacitance in the secondary walls, nested inside the cavities, represented by  $R_3$ , and ( $CPE_3$  and  $n_3$ ).

The  $R$ ,  $CPE$  and  $n$  values extracted from the fitted spectra are given in Table 5.5. The charge transfer resistance ( $R_1$ ) can also be attributed to the potential gradient between the electroactive species in electrolyte and electrode surface.<sup>18</sup> The higher of  $CPE$  values in  $H_2SO_4$  medium can be attributed to the higher ionic mobility and higher molar ionic conductivity of  $H^+$  ions. The total calculated  $CPE$  is compared with the capacitance value obtained from CV in table 5.4. The good agreement between them, further confirms the validity of simulated circuit.

Table 5.4 : The extracted parameters of equivalent circuit of VGN in different aqueous electrolytes obtained through EIS spectrum analyser

	1M Na <sub>2</sub> SO <sub>4</sub>	1M KOH	1M H <sub>2</sub> SO <sub>4</sub>
R <sub>s</sub> [ $\Omega$ -cm <sup>2</sup> ]	21.68	20.54	21.58
CPE <sub>1</sub> [ $\mu$ F/cm <sup>2</sup> ]	1.87	1.41	14.11
n <sub>1</sub> [0<n<1]	0.7487	0.7549	0.8375
R <sub>1</sub> [ $\Omega$ -cm <sup>2</sup> ]	110.26	370.50	72.02
CPE <sub>2</sub> [ $\mu$ F/cm <sup>2</sup> ]	17.88	143.42	90.00
n <sub>2</sub> [0<n<1]	0.9761	0.9421	0.9516
R <sub>2</sub> [ $\Omega$ -cm <sup>2</sup> ]	10 <sup>6</sup>	19327	739460
CPE <sub>3</sub> [ $\mu$ F/cm <sup>2</sup> ]	15.39	50.00	76.35
n <sub>3</sub> [0<n<1]	0.2227	0.9885	0.9746
R <sub>3</sub> [ $\Omega$ -cm <sup>2</sup> ]	3.13	29.40	8.07
Total CPE [ $\mu$ F/cm <sup>2</sup> ]	35.14	194.83	180.46
C <sub>s</sub> @100 mV/s [ $\mu$ F/cm <sup>2</sup> ]	43.84	197.63	188.48

Table 5.5: Comparison of electrochemical performance of VGN in various aqueous electrolytes

	1M Na <sub>2</sub> SO <sub>4</sub>	1M KOH	1M H <sub>2</sub> SO <sub>4</sub>
C <sub>s</sub> @100 mV/s [ $\mu$ F/cm <sup>2</sup> ]	43.84	197.63	188.48
Capacitance retention after 200 C-D cycles	95.9 %	98.4 %	96.8 %
Columbic efficiency	62.1 %	27.6 %	64.4 %
Vertical slope from Nyquist plot	87.6°	84.8°	86.5°
Phase angle from Bode Plot	-85°	-60°	-80°
Time constant (ms)	20	390	50
Charge transfer resistance (R <sub>ct</sub> ) [ $\Omega$ -cm <sup>2</sup> ]	110.26	370.50	72.02

The various electrochemical parameters of the VGN3/electrolyte systems are compared in Table 5.5. To further investigate the reason behind the different electrochemical behavior, the Raman spectroscopic experiments are carried out on the

exposed area of the VGN3 electrodes after electrochemical performance. Very similar Raman spectrum is observed before and after electrochemical experiments, implying the structural stability of VGN3 [Figs. 5.10 (a) and (b)]. As discussed in Section 3.2.2, the FWHM of Raman modes are a measure of doping and defect, induced after the electrochemical experiment. A small broadening in FWHM of D band is observed after the electrochemical studies. The relatively higher broadening is observed in KOH due to its oxidizing nature. KOH is expected to have caused surface oxidation of VGN after 200 cycles of charge-discharge, resulting in local structural damage. This is also reflected in the Nyquist plot as deviated from original spectra after 200 cycles. The results are in good agreement with that of Zhu *et al.*<sup>11</sup>

Hence, it is obvious that proper choice of electrolyte solutions is very essential for the development of SC. The superior capacitance performance, excellent capacity retention, good cycle life and low resistance of VGN3/H<sub>2</sub>SO<sub>4</sub> system can be attributed to the compatible ionic size to access nanoporous structure of VGN3 efficiently as well as higher ionic conductivity and fast electron kinetics.

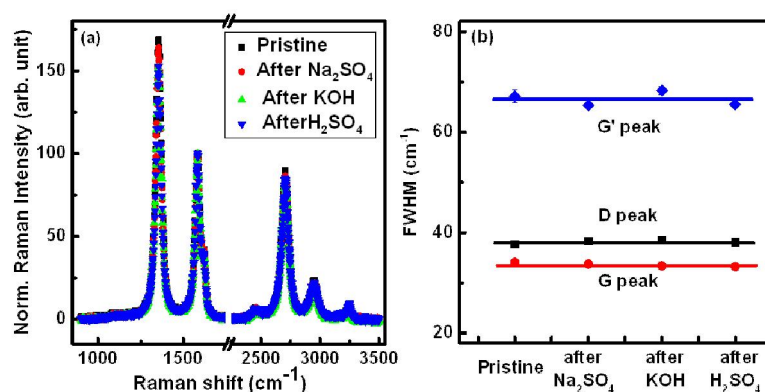


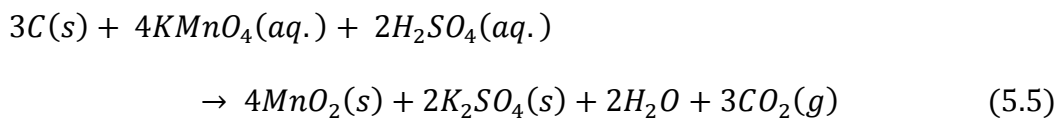
Figure 5.10: (a) Raman spectra, and (b) FWHM of D/G/G' of pristine VGN3 and after electrochemical experiment in 1M Na<sub>2</sub>SO<sub>4</sub>, 1M KOH and 1M H<sub>2</sub>SO<sub>4</sub>

## 5.4 Influence of MnO<sub>2</sub> decoration

It is been reported in literature that the capacitance of VGN can be improved by decorating MnO<sub>2</sub> on the VGN surface.<sup>3,21,22</sup> To understand the effect of MnO<sub>2</sub> decoration, the VGN3 sample are decorated with MnO<sub>2</sub> and their electrochemical performances are carried out. In literature, most of the studies pertaining to MnO<sub>2</sub>/VGN composite as SC electrodes are carried out in Na<sub>2</sub>SO<sub>4</sub> electrolyte.<sup>3,21,22</sup> Since we obtained better results in H<sub>2</sub>SO<sub>4</sub> electrolytes, the electrochemical performance MnO<sub>2</sub>/VGN3 is studied and compared with that in Na<sub>2</sub>SO<sub>4</sub>.

### 5.4.1. MnO<sub>2</sub> decoration

The VGN3 on *n*-Si(100) are decorated with MnO<sub>2</sub> by dipping them in 10 mM KMnO<sub>4</sub> acidic aqueous solution at 80 °C for 5 minutes. The reaction between VGN and acidic KMnO<sub>4</sub> aqueous solution is given as follows:<sup>21</sup>



The electrodes are then taken out and washed in deionized water followed by drying in open atmosphere for 30 min. Thus, without any binder MnO<sub>2</sub>/VGN3 electrode is prepared for their electrochemical investigation.

### 5.4.2. Raman spectroscopic analysis

To study the effect of MnO<sub>2</sub> deposition, the MnO<sub>2</sub>/VGN3 electrodes are analyzed using Raman spectroscopy. The decoration of MnO<sub>2</sub> on VGN3 does not show any significant variation in the Raman spectra except minute broadening of the D, G and G'

bands ( $\sim 2\text{-}4\text{ cm}^{-1}$ ) and blue shift in position ( $\sim 2\text{ cm}^{-1}$ ). The presence of  $\text{MnO}_2$  layer over VGN3 is confirmed from the presence of band at  $652.0\text{ cm}^{-1}$  [Fig. 5.11]. The FWHM of the Raman band is found to be  $26.3\text{ cm}^{-1}$  indicating excellent structural quality of the  $\text{MnO}_2$  layers. The extracted parameters of Raman spectra of VGN3 and  $\text{MnO}_2/\text{VGN3}$  are listed in Table 5.6.

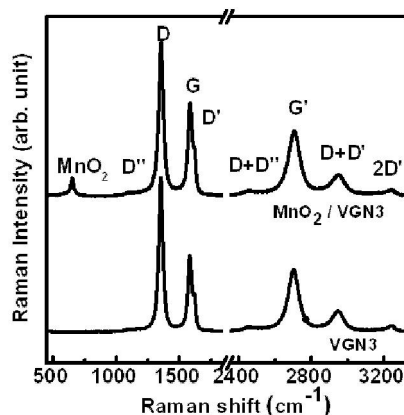


Figure 5.11: Raman spectra of VGN3 and  $\text{MnO}_2/\text{VGN3}$

Table 5.6: Extracted parameters of Raman analysis of VGN3 and  $\text{MnO}_2/\text{VGN3}$

	D-band		G-band		G'-band		MnO <sub>2</sub>	
	Position (cm <sup>-1</sup> )	FWHM (cm <sup>-1</sup> )	Position (cm <sup>-1</sup> )	FWHM (cm <sup>-1</sup> )	Position (cm <sup>-1</sup> )	FWHM (cm <sup>-1</sup> )	Position (cm <sup>-1</sup> )	FWHM (cm <sup>-1</sup> )
VGN3	1353.7	37.7	1583.5	36.0	2701.8	69.42	-	-
$\text{MnO}_2/\text{VGN3}$	1355.6	42.2	1585.3	38.8	2705.2	75.16	652.0	26.3

### 5.4.3. Cyclic Voltammetry study

The cyclic voltammetric studies of  $\text{MnO}_2/\text{VGN3}$  are carried out in  $\text{Na}_2\text{SO}_4$  and 1M  $\text{H}_2\text{SO}_4$  for comparison. Figure 5.12(a-b) shows the CV curves of  $\text{MnO}_2/\text{VGN3}$  acquired at scan rates of 100-500 mV/s in 1M  $\text{Na}_2\text{SO}_4$  and 1M  $\text{H}_2\text{SO}_4$  electrolyte, respectively. The nearly rectangular and symmetric CV curves of  $\text{MnO}_2/\text{VGN3}$  in both electrolytes ensure

the highly capacitive behavior accompanied with good ion diffusivity. Figure 5.12(c) depicts the CV of VGN3 in 1M H<sub>2</sub>SO<sub>4</sub>, MnO<sub>2</sub>/VGN3 in 1M Na<sub>2</sub>SO<sub>4</sub> and MnO<sub>2</sub>/VGN3 in 1M H<sub>2</sub>SO<sub>4</sub> electrolyte at 100 mV/s scan rate for easy comparison. The plot of specific capacitance vs scan rate is depicted in Fig. 5.12(d).

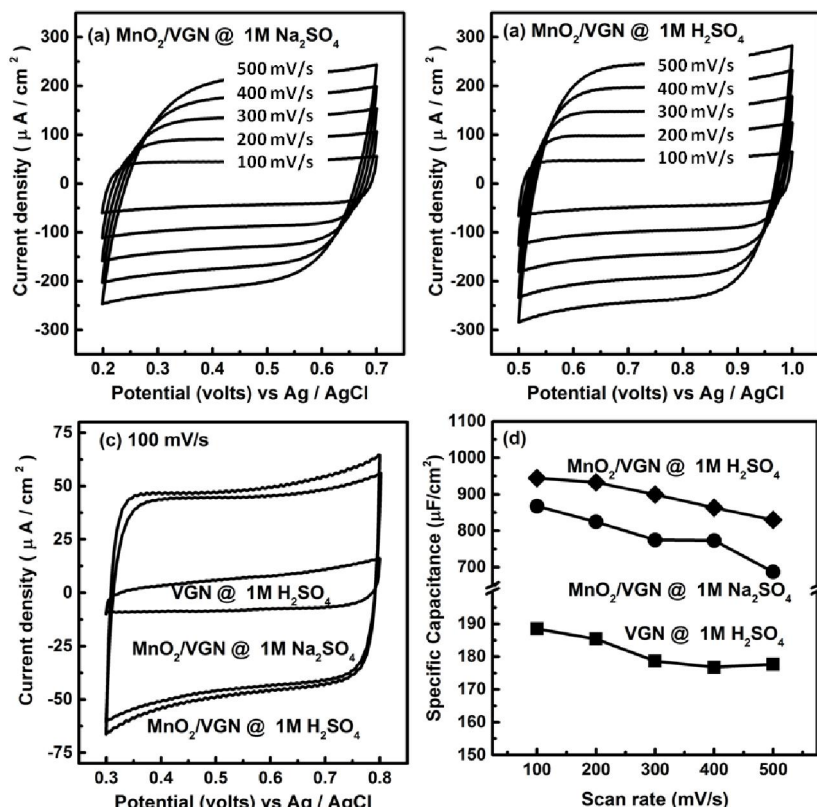


Figure 5.12: Cyclic voltammogram (CV) of MnO<sub>2</sub>/VGN3 in (a) 1M H<sub>2</sub>SO<sub>4</sub> and (b) 1M H<sub>2</sub>SO<sub>4</sub> at scan rates of 100-500 mV/s, respectively; (c) Comparative CV of VGN3 in 1M H<sub>2</sub>SO<sub>4</sub>, MnO<sub>2</sub>/VGN3 in 1M Na<sub>2</sub>SO<sub>4</sub> and MnO<sub>2</sub>/VGN3 in 1M H<sub>2</sub>SO<sub>4</sub> electrolyte at scan rate of 100 mV/s; (d) Specific capacitance vs scan rate of VGN3 in 1M H<sub>2</sub>SO<sub>4</sub>, MnO<sub>2</sub>/VGN3 in 1M Na<sub>2</sub>SO<sub>4</sub> and MnO<sub>2</sub>/VGN3 in 1M H<sub>2</sub>SO<sub>4</sub>

The specific capacitance of MnO<sub>2</sub>/VGN3 are calculated using Eqn. 5.1 and found to be 867.4 and 944.6 μF/cm<sup>2</sup> in 1M Na<sub>2</sub>SO<sub>4</sub> and 1M H<sub>2</sub>SO<sub>4</sub> electrolyte, respectively at 100 mV/s scan rate. It is clear that the MnO<sub>2</sub>/VGN3 show enhanced charge storage

capacity about 4.6 times in 1M Na<sub>2</sub>SO<sub>4</sub> and 5 times in 1M H<sub>2</sub>SO<sub>4</sub> over that of VGN3 in 1M H<sub>2</sub>SO<sub>4</sub> electrolyte, respectively. This enhancement can be further improved by growing VGN with more open network and higher height as well as by tuning the temperature of acidic KMnO<sub>4</sub> aqueous solution and dipping time.<sup>21</sup> The higher capacitance value of MnO<sub>2</sub>/VGN3 in 1M H<sub>2</sub>SO<sub>4</sub> electrolyte is due to the higher mobility of H<sup>+</sup> ions, as discussed in Section 5.3. The capacitive behavior of MnO<sub>2</sub>/VGN3 is a combined effect which arises from EDLC of VGN and pseudocapacitance of MnO<sub>2</sub>. In addition, VGN serve as an excellent backbone for the effective utilization of MnO<sub>2</sub> as a energy storage material.

#### 5.4.4. Charge-discharge study

The panels (a) and (b) of Fig. 5.13 represent charge-discharge profile of MnO<sub>2</sub>/VGN3 in 1M Na<sub>2</sub>SO<sub>4</sub> and 1M H<sub>2</sub>SO<sub>4</sub> electrolyte at current density of 5-25 μA/cm<sup>2</sup>, respectively. The almost linear and unaltered charge-discharge profile ensures the excellent electrochemical behavior of MnO<sub>2</sub>/VGN3 in both electrolytes. The comparative charge-discharge profile of VGN3 in H<sub>2</sub>SO<sub>4</sub>, MnO<sub>2</sub>/VGN3 in Na<sub>2</sub>SO<sub>4</sub> and MnO<sub>2</sub>/VGN3 in H<sub>2</sub>SO<sub>4</sub> electrolyte at current density of 5 μA/cm<sup>2</sup> is shown in Fig. 5.13(c). Figure 5.13(d) shows capacitance retention of different systems as a function of cycle number. The VGN3 in 1M H<sub>2</sub>SO<sub>4</sub>, MnO<sub>2</sub>/VGN3 in 1M Na<sub>2</sub>SO<sub>4</sub> and MnO<sub>2</sub>/VGN3 in 1M H<sub>2</sub>SO<sub>4</sub> exhibited excellent electrochemical stability with capacitance retention of 91.4%, 84.4%, and 86.9%, respectively.

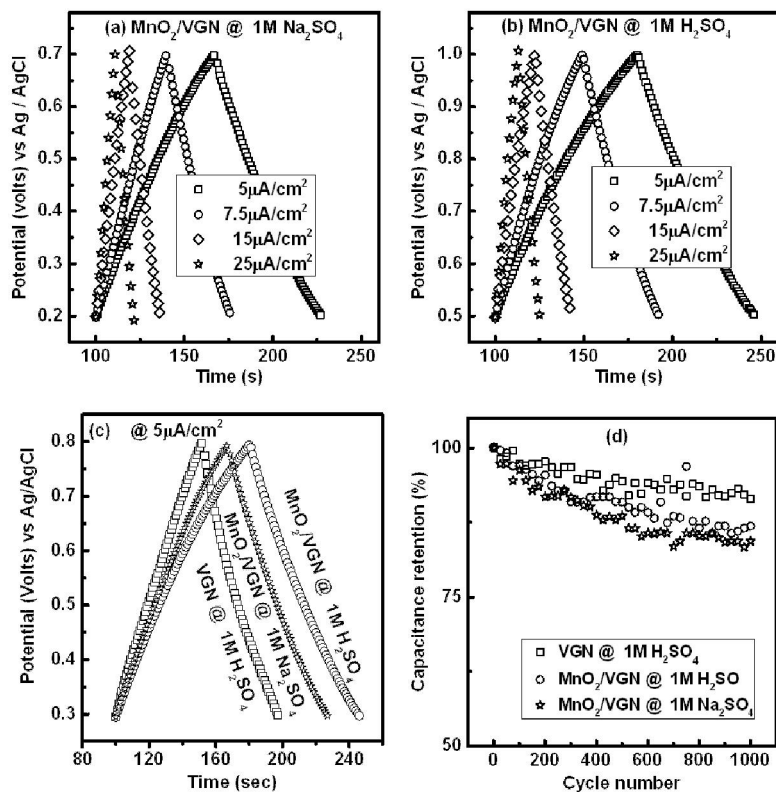


Figure 5.13: Charge-discharge profile of MnO<sub>2</sub>/VGN3 in (a) 1M Na<sub>2</sub>SO<sub>4</sub> and (b) 1M H<sub>2</sub>SO<sub>4</sub> electrolyte at current density in the range of 5-25 μA/cm<sup>2</sup>, respectively; (c) Comparative charge-discharge profile of VGN3 in 1M H<sub>2</sub>SO<sub>4</sub>, MnO<sub>2</sub>/VGN3 in 1M Na<sub>2</sub>SO<sub>4</sub> and MnO<sub>2</sub>/VGN3 in 1M H<sub>2</sub>SO<sub>4</sub> at current density of 5 μA/cm<sup>2</sup>; and (d) capacitance retention vs cycle number of VGN3 in 1M Na<sub>2</sub>SO<sub>4</sub>, MnO<sub>2</sub>/VGN3 in 1M Na<sub>2</sub>SO<sub>4</sub> and MnO<sub>2</sub>/VGN3 in 1M H<sub>2</sub>SO<sub>4</sub>.

#### 5.4.5. Electrochemical impedance study

The Nyquist plot of VGN3 in 1M H<sub>2</sub>SO<sub>4</sub>, MnO<sub>2</sub>/VGN3 in 1M Na<sub>2</sub>SO<sub>4</sub> and MnO<sub>2</sub>/VGN3 in 1M H<sub>2</sub>SO<sub>4</sub> electrolyte at low frequency and high frequency region is given in Fig. 5.14 (a) and (b), respectively. As observed from Fig. 5.14(a), the vertical line at low frequency region is steeper for MnO<sub>2</sub>/VGN3 in 1M H<sub>2</sub>SO<sub>4</sub> than that of MnO<sub>2</sub>/VGN3 in 1M Na<sub>2</sub>SO<sub>4</sub>. The observed 45° sloped portion for MnO<sub>2</sub>/VGN3 in both electrolytes indicates the higher variation in ionic diffusion path length and increased obstruction of ion movement [Fig. 5.14(b)].<sup>15</sup> It is also seen from Fig. 5.14(b) that the smaller semicircle at high frequency region of MnO<sub>2</sub>/VGN3 in 1M H<sub>2</sub>SO<sub>4</sub> compared to 1M Na<sub>2</sub>SO<sub>4</sub> indicates

low interfacial charge-transfer resistance in  $\text{H}_2\text{SO}_4$ . As seen in Section 5.3, better performance is observed in  $\text{H}_2\text{SO}_4$  electrolyte.

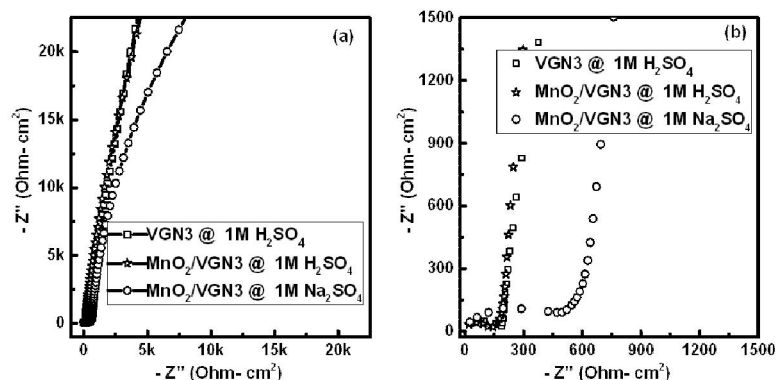


Figure 5.14: Nyquist plot of VGN3 in 1M  $\text{H}_2\text{SO}_4$ ,  $\text{MnO}_2/\text{VGN3}$  in 1M  $\text{Na}_2\text{SO}_4$  and  $\text{MnO}_2/\text{VGN3}$  in 1M  $\text{H}_2\text{SO}_4$  electrolyte at (a) low frequency and (b) high frequency region

## 5.5 Summary

The electrochemical behavior of vertical graphene nanosheets (VGN) and  $\text{MnO}_2/\text{VGN}$  are investigated using cyclic voltammetry, charge-discharge and electrochemical impedance spectroscopy.

- The conductive graphene sheets within the 3D networks serve as a current collector and provide multiple pathways to facilitate the transport of ions and electrons in the electrode surface.
- The charge storage mechanism is discussed with the help of EIS study, which supports the CV data.
- It is shown that  $\text{MnO}_2$  can be anchored efficiently on to VGN to enhance the specific capacitance of electrodes.
- The VGN and  $\text{MnO}_2/\text{VGN}$  in  $\text{H}_2\text{SO}_4$  medium is found to have better performance in terms of capacity retention, fast electron kinetics and minimal change in structure.

## 5.6 References

1. Mironovich, K. V., *et al.*, *Phys. Chem. Chem. Phys.* (2014) **16** (46), 25621
2. Miller, J. R., *et al.*, *Science* (2010) **329** (5999), 1637
3. Seo, D. H., *et al.*, *Adv. Energy Mater.* (2013) **3** (10), 1316
4. Cai, M., *et al.*, *ACS nano* (2014) **8** (6), 5873
5. Qi, J. L., *et al.*, *Nanoscale* (2015) **7** (8), 3675
6. Wang, D. W., *et al.*, *Angew. Chem.* (2008) **120** (2), 379
7. Heller, I., *et al.*, *Nano Lett.* (2005) **5** (1), 137
8. Dinh, T. M., *et al.*, *Nano Energy* (2014) **10**, 288
9. Sevilla, M., and Fuertes, A. B., *ACS nano* (2014) **8** (5), 5069
10. Ruiz, V., *et al.*, *Electrochim. Acta* (2009) **54** (19), 4481
11. Zhu, J., *et al.*, *Phys. Chem. Chem. Phys.* (2015), 28666
12. Nightingale Jr, E., *J. Phys. Chem.* (1959) **63** (9), 1381
13. Atkins, P., and De Paula, J., *Elements of physical chemistry*. Oxford University Press, USA: 2013
14. Ghosh, A., and Lee, Y. H., *ChemSusChem* (2012) **5** (3), 480
15. Zhang, K., *et al.*, *Chem. Mater.* (2010) **22** (4), 1392
16. Itagaki, M., *et al.*, *J. Power Sources* (2007) **164** (1), 415
17. Bandarenka, A. S., *Analyst* (2013) **138** (19), 5540
18. Kang, J., *et al.*, *Electrochim. Acta* (2014) **115**, 587
19. Sugimoto, W., *et al.*, *J. Phys. Chem. B* (2005) **109** (15), 7330
20. Wang, D.-W., *et al.*, *J. Phys. Chem. B* (2006) **110** (17), 8570
21. Zhang, Y., *et al.*, *ACS Applied Materials & Interfaces* (2016) **8** (11), 7363
22. Hassan, S., *et al.*, *J. Power Sources* (2014) **249**, 21

# 6

## **Conclusions and Future Prospect**

*To know more about the material, only possibility way is do more experiments*

## 6.1 Conclusions

The present thesis reports the growth of controlled and optimized vertical graphene nanosheets (VGN) in electron cyclotron resonance chemical vapor deposition by varying the growth parameters. The process parameters include growth time, growth temperature, feedstock gas composition, distance from plasma source to substrate, plasma power and substrates. The morphology and properties of VGN are investigated by several characterization techniques, mainly, scanning electron microscopy, Raman spectroscopy, contact angle measurement and four probe resistance measurement. Based on the above observations, a ternary field diagram and a four stage phenomenological growth stage model are developed to substantiate growth mechanism of VGN through plasma-surface interaction.

In view of outstanding geometry and proven capability, the electrochemical performance of VGN as a potential candidate for supercapacitor electrode is performed using three electrode system. The electrochemical performance of VGN is carried out by taking different morphology under various aqueous electrolytes. An equivalent circuit model is established from impedance spectroscopy to understand the electrolyte/electrode interaction. In addition to that, MnO<sub>2</sub> decorated VGN shows huge enhancement in charge storage capacity.

## 6.2 Future Prospects

The current thesis reports on the growth, studies and electrochemical performance of vertical graphene nanosheets (VGN). An attempt has given to understand the plasma-surface interaction and VGN growth. However, still several issues listed below, need to be addressed to get clear picture on the growth:

- influence of local electric field due to plasma on the growth of VGN,
- insights of interface between vertical graphene and substrate to understand its nucleation process,
- Origin of  $D'$  peak ( $\sim 1140\text{ cm}^{-1}$ ) and  $D^*$  ( $\sim 1500\text{ cm}^{-1}$ ) in Raman spectra of VGN

In addition to the growth, VGN can be utilized in wide range of applications, which need further explorations are

- electrochemical performance of VGN under different organic electrolytes,
- decorating VGN with other metal oxides, hydroxides or by polymer materials,
- field-emission and sensing properties of pristine and metal decorated VGN.